HSI Contaminants Project: Missouri Universities Contact Summary

Conatct	Notes
John Yang, Associate Prof. Lincoln University yangj@lincolnu.edu 573-681-5383	.emailed 2-9-05 .replied 2-17-05 .environment/soil chemist, and recent research is on remediation and risk assessment of lead contaminated soils in the Jasper County Superfund Site, Southwest Missouri. A few months ago, was involved in a proposal for ecological assessment of the Jasper County lead mine area using the hyperspectral imagery, but the proposed project was not funded. heard that NASA had conducted a similar project, but the project was terminated due to poor correlation with ground truth. Referred me to colleauge Dr. Tesfaye.
Dr. Tesfaye tesfayes@lincolnu.edu	emailed 2/25/05 replied 2/25/05 .Referred by Dr. Yang as having worked on the aforementioned NASA proposal .may provide insight as to why project was terminated .was involved in EPA proposal to use Multispectral NOT HSI at the Oronogo-Duenweg Mining Belt Superfund site in Jasper County .indicated that a HSI project to identify contamination in abandoned lead mines (Tri-state) NASA (JPL?) hyperspectral survey using AVIRIS but was cancelled due to poor results shown by ground-truthing .MoDNR and EPA Region 7 (Mark Doolan) may be able to provide further info. .is interested in our project results
Dr. Curt Elmore UM-Rolla elmoreac@umr.edu 573-341-6784	emailed 2-9-05 replied 2-9-05 .doesn't have experience with imagery, only soil and water contamination via traditional ground sampling methods .referred a colleague at UMR Dr. David Rogers
Dr. Monika Moskal Southwest Missouri State University lmm878@smsu.edu	emailed 2-9-05 replied 2-11-05 .has worked with hyperspectral data - AVIRIS and *casi* and has a paper regarding work with AVIRIS in Yellowstone .for *casi* work collected spectral libraries with ground spectroradiometer
Dr. Kenneth Sudduth UM Agronomy SudduthK@missouri.edu	emailed 2-14-05 follow-up email 2-25-05 replied 2/28/05 .has experience with hyperspectral data - probably in agricultural context .used HSI to detect within crop field variability .indicated laborious task of processing HSI and little improvement over multispectral method .included 3 .pdf's of work

HSI Contaminants Literature

Analysis of Hyperspectral Imagery, University of Texas. 2005.

Archer (2005). "Archer: System Info."

Aspinall, R. J., W. Andrew Marcus, and Joseph W. Boardman (2002). "Considerations in Collecting, Processing, and Analysing High Spatial Resolution Hyperspectral Data for Environmental Investigations." Journal of Geographical Systems 4: 15-29.

Chevrel, S., Reinhard Belocky, and Klemens Grösel (2002). "Monitoring and Assessing the Environmental Impact of Mining in Europe using Advanced Earth Observation Techniques - MINEO: First Results of the Alpine Test Site."

Dobrovolny, P., Lubomil Pospisil, and Otakar Pazdirek. (1998). Detecting Environmental Impacts of Uranium Mining with the use of Remotely Sensed and Geophysical Data. Geographic Information Systems: Information Infrastructures and Interoperability for the 21st Century Information Society, Brno, Czech Republic.

Hong, S. Y., K.A. Sudduth, N.R. Kitchen, H.L Palm, and W.J. Wiebold (2001). Using Hyperspectral Remote Sensing Data To Quantify Within-field Spatial Variability. Third International Conference on Geospatial Information in Agriculture and Forestry, Denver, Colorado.

Hong, Suk Young, Kenneth A. Sudduth, Newell R. Kitchen, Scott T. Drummond, Harlan L. Palm, and William J. Wiebold (2002). Estimating Within-Field Variations in Soil Properties from Airborne Hyperspectral Images. Pecora 15/Land Satellite Information IV/ISPRS Commission I/FIEOS.

Hsu, P.H. and Y.H. Tseng (2000). Multiscale Analysis of Hyperspectral Data Using Wavelets for Spectral Feature Extraction. 21st Asia Conference on Remote Sensing, December 4-8, Taipei, Taiwan.

Hsu, P.H (2004). Feature Extraction of Hyperspectral Images Using Matching Pursuit. XXth ISPRS Congress, July 12-23, Istanbul, Turkey.

Jacquez, G. M., W. Andrew Marcus, Richard J. Aspinall, and Dunrie A. Greiling (2002). "Exposure Assessment Using High Spatial Resolution Hyperspectral (HSRH) Imagery." Journal of Geographical Systems 4: 1-14.

Lèvesque, J., V. Singhroy, K. Staenz, and D. Bolton (1997). Site Characterization of Mine Tailings at the INCO Copper Cliff Tailings Impoundment Area using casi Imagery. International Symposium of Geomatics in the era of RADARSAT, Ottawa, Ontario, Canada.

Lèvesque, J., Tom Szeredi, Karl Staenz, and Vern Singhroy (1998). Spectral Band Selection from casi Data for Monitoring Mine Tailings Site Rehabilitation. 20th Canadian Symposium on Remote Sensing, Calgary.

Lèvesque, J., Karl Staenz, Jiali Shang, Bob Neville, Paul Yearwood, and Vern Singhroy (1999). Temporal Monitoring of Mine Tailings Revegetation Using Hyperspectral Data, Sudbury, Ontario. Thirteenth International Conference on Applied Geologic Remote Sensing. Vancouver, British Columbia, Canada. 2: 21-28.

Marsh, S.H., C. Cotton, G. Ager, and D.G. Tragheim (2000). Detecting Mine Pollution Using Hyperspectral Data in Temperate, Vegetated European Environments. Fourteenth International Conference on Applied Geologic Remote Sensing, November 6-8, Las Vegas, Nevada.

Ong, C., T.J. Cudadhy, and G. Swayze (2003). Predicting Acid Drainage Related Physicochemical Measurements Using Hyperspectral Data. 3rd EARSeL Workshop on Imaging Spectroscopy, Oberpfaffenhofen, Herrsching, Germany.

Shang, J., Josèe Lèvesque, Philip Howarth, Bill Morris, Karl Staenz, and Paul Yearwood (1999). Preliminary Investigation of Acid Mine Drainage Detection Using casi Data, Copper Cliff, Ontario, Canada. Fourth International Airborne Remote Sensing Conference Exhibition / 21st Canadian Symposium on Remote Sensing, Ottawa, Ontario, Canada.

Sich, H. (2005). Thom and Mom. Boulder, CO, West Press.

J Geograph Syst (2002) 4:15–29

Journal of Geographical Systems
© Springer-Verlag 2002

Considerations in collecting, processing, and analysing high spatial resolution hyperspectral data for environmental investigations

Richard J. Aspinall[1], W. Andrew Marcus[2], Joseph W. Boardman[3]

[1] Geographic Information and Analysis Center, Department of Earth Sciences, Montana State University, Bozeman, MT 59717-3495, USA (e-mail: aspinall@montana.edu)
[2] Department of Geography, University of Oregon, Eugene, OR 97403-1251, USA (e-mail: marcus@oregon.uoregon.edu)
[3] Analytical Imaging and Geophysics LLC, 4450 Arapahoe Avenue #100, Boulder, CO 80303, USA (e-mail: boardman@aigllc.com)

Received: 22 July 2001 / Accepted: 30 October 2001

Abstract. This paper briefly describes the methods available for collection, atmospheric and geometric correction, and processing of hyperspectral imagery. Discussion of data capture concentrates on logistics of integrating image acquisition with field data collection. Atmospheric correction is required to use the imagery with reference spectra from field and laboratory sensors; a variety of methods for atmospheric correction are described. Geometric correction is required for integration of the image data and derived products with other geographic information. A description of methods for single and multiple feature identification is provided. These all focus on the analysis of the spectral description of surface materials provided by hyperspectral imagery; methods for multiple feature identification take advantage of high spectral dimensionality of the imagery to identify sub-pixel components. A role for spatial analysis combined with spectral analysis in interpretation of environmental features is identified.

Key words: High spatial resolution, hyperspectral imagery, analysis, atmospheric and geometric correction

JEL classification: C63, C69, C89

The collaboration among the three authors is the result of research in the High Tech Landscapes initiative of Yellowstone Ecosystem Studies and major funding from the NASA EOCAP program, Stennis Space Flight Center. The impetus for writing the manuscript came from papers and discussion at the workshop on "Exposure Assessment Using Hyperspatial Imagery" which was hosted by BioMedware, Inc. and was funded by the National Institute of Environmental and Health Sciences. The constructive comments of three referees are gratefully acknowledged.

1 Introduction

The development of widely accessible high spatial resolution hyperspectral (HSRH) data is relatively recent, and thus is a relatively novel data source for analysis of large spatial scale environmental and earth science questions. Although the principles of spectroscopy are well known and methods for analysis are well developed, particularly for spectra collected in laboratory environments (e.g.,Clark et al. 1992; Clark and Swayze 1995), the heterogeneity of landscapes and earth surface features in large scale environmental studies presents new challenges and opportunities for analysis of hyperspectral imagery. Likewise, although principles of ground truthing and accuracy assessment are well established in remote sensing literature (e.g., Congalton and Green, 1999), the high spatial resolution of modern data presents challenges to field data collection and data analysis.

This paper describes some of the major technical issues in capturing and processing high spatial resolution hyperspectral imagery. We also guide the reader to major literature on these topics, much of which is contained in the "grey literature" of conference proceedings and web sites. Methods and analyses applied to high spatial resolution hyperspectral imagery are described in the same sequence that a typical user encounters. Explanation of data collection and image pre-processing is followed by description of a series of methods for data analysis. We conclude with suggestions for ways to enhance future analysis of hsrh data.

2 The nature of high spatial resolution hyperspectral imagery

The principles of spectroscopy employed in hyperspectral image data collection and processing are well known and have been used for many years (Goetz et al. 1985). Spectroscopy measures the electromagnetic radiation from objects as a spectrum, with different materials having different characteristic spectra based on their chemical composition. For example, minerals (Goetz et al. 1985; Kruse et al. 1993; Clark and Swayze 1995), vegetation (Ustin et al. 1999), plant properties (Gamon et al. 1993, 1995; Roberts et al., 1993; Ustin et al. 1996) snow and ice (Clark and Swayze 1995), and soils (Palacios-Oreuta and Ustin 1996) have all been successfully and directly identified and measured using spectroscopy. Hyperspectral remote sensing measures the spectral properties of the environment using imaging spectrometers placed on airborne and spaceborne platforms. A list of hyperspectral imaging systems can be found at http://rst.gsfc.nasa.gov/sect13/is_list.html.

The word "hyper," literally translated, means "excessive in extent or quality" or "over, above, beyond" (Gove 1976, p. 1112). In contrast to multispectral scanners, the amount of spectral information recorded by hyperspectral spectrometers thus exceeds the amount required to identify many features. This "excess" information results from the high spectral resolution (i.e., narrow band widths) relative to multispectral scanners and the wide range of spectra that are recorded, which together enable users to extract subtle differences in spectral signatures. There is no absolute definition of how many bands are needed or how narrow the bandwidths need to be to make imagery "hyper," although most sensors that are called

hyperspectral have 48 or more bands with spectral resolutions of 20 nm or smaller. A number of the key characteristics that influence the data collected by hyperspectral sensors are described in Table 1.

Just as there is not a specific number of bands required for imagery to be hyperspectral, there is no clear threshold of pixel size at which coarse spatial resolution imagery transitions to high spatial resolution imagery. For the purposes of our work, we define high spatial resolution as imagery with pixels that are 5 m or less in size. This size range represents (for hyperspectral imagery), a spatial resolution that has only recently become available as sensors have been mounted on low flying aircraft. In addition, pixels that are 5 m or smaller in size present georectification, coregistration and ground truthing problems that are not present with coarser spatial resolution hyperspectral analysis.

3 Data collection and pre-processing of the imagery

3.1 Flight planning for high spatial resolution hyperspectral data collection

At the present time, acquisition of airborne hsrh imagery is limited by instrument availability and cost. A number of instruments, such as Probe1 and HyMap, are commercially available, while other instruments such as AVIRIS are available to NASA-supported researchers. In addition to financial costs, data collection using commercial instruments has a number of logistical constraints. Weather conditions influence flights and the quality

Table 1. Properties of imaging spectrometers

Property	Description
Spectral range	describes the measured range of the electromagnetic spectrum. Different materials absorb in different wavebands thus the spectrum recorded by an instrument should include these characteristic wavebands to help identify different materials. Airborne and spaceborne instruments typically record in the visible and near infrared spectrum (0.4 μm to 2.5–3.0 μm).
Spectral bandwidth	the width of an individual band in the spectrometer. Bands are adjacent in a spectrometer to provide continuous measurement of the entire spectrum. The narrower the bandwidth, the narrower the absorption features that can be measured and the greater the resolution of the spectrum.
Bandpass profile	describes the shape of the response of the detector in the spectrometer across the spectral bandwidth. The shape is usually gaussian. The width of the bandpass profile is described as the wavelength at the 50% response level of the function, the Full Width at Half Maximum.
Spectral sampling	the distance in wavelength between bandpass profiles for each channel as a function of wavelength.
Signal to noise ratio	describes the precision with which the spectrometer measures the spectrum relative to the detail needed to resolve particular features. A lower signal to noise ratio is needed for strong spectral features while a higher signal to noise ratio is needed for weak features.

of data collected, flight scheduling must be coordinated with field data collection, since ground-based data may be required on the day of the flight or in the several days immediately surrounding it. We suggest that individuals planning HSRH-flights have a project management strategy that particularly focuses on the logistics of data collection.

3.2 Initial considerations for image processing and field data collection

As with any remote sensing analysis, the nature of field data collection and image pre-processing required to use hsrh imagery will depend on how the data will be analysed. Of particular importance is whether a "top-down" or "bottom-up" analysis is envisioned.

Top-down approaches use field mapping to train the imagery to detect certain features. Field surveys and accurate georeferencing and co-registration of images and field maps are required for top-down approaches. In some instances however, atmospheric corrections may not be required with top down approaches. The small geographic extent of hsrh images reduces the potential for significant variations in atmospheric effects across the scene, while mapping field features directly to the image means that the classifying algorithm can incorporate atmospheric effects into the feature spectra as it searches the image to find similar features. A particular feature type will therefore probably appear similar across the entire image and the atmospheric effects should not overly confuse the mapping process. As one extends the analysis over larger areas or between images, however, ignoring atmospheric effects becomes increasingly untenable.

In contrast, bottom-up approaches typically use ground-based or laboratory-based spectral libraries to identify key features. In this situation, atmospheric corrections are absolutely essential, because the effects of the atmosphere must be removed in order for image spectra to match library spectra. Because the identification of features relies on the matching of spectra rather than overlaying ground maps on the imagery, georeferencing and image co-registration can be relatively unimportant in the bottom-up approach. In bottom-up approaches using library spectra accurate atmospheric corrections are particularly important, where specific bands are very strongly affected by atmospheric composition (Table 2). The great advantage of bottom-up approaches is that the same spectral library can be extended over wide areas and across multiple images to identify specific feature types, as long as the images are atmospherically corrected.

Table 2. Absorption wavelengths of common atmospheric constituents

Constituent	Absorption wavelength (μm)
Ozone	0.35
	9.6
CO_2	1.6
	2.005
	2.055
Water	0.69
	0.72
	0.76

HSRH-imagery can sometimes provide the unique opportunity to take advantage of the strong points of both top-down and bottom-up approaches, while avoiding some of their pitfalls. Because the pixel resolution is small, the image may contain pixels that contain only the feature of interest (e.g., a wetland, a plant species type, or a particular soil type). Spectra can be collected from these pixels to create an airborne spectral library. The great advantage of this type of library is that it incorporates the atmospheric effects in the feature spectra and therefore does not require applying the many assumptions and uncertainties inherent in atmospheric corrections and the matching of image spectra with library spectra. Likewise, the ability to visually identify and map these pure pixels directly to the image (much like an air photo) means that precision field mapping and image georectification may not be necessary to accurately map features on the image.

3.3 Atmospheric corrections

Analytical approaches: As noted above, the data collected by airborne or spaceborne hyperspectral sensors are not immediately comparable to laboratory or ground-based spectra, because the atmosphere alters the spectral signal reaching the sensor. Data collected using imaging spectrometers therefore must be converted from raw radiance values to atmospherically corrected reflectance values to allow spectra to be compared with reference spectra in spectral libraries (Kruse 1994). Ideally, absolute reflectance is calculated, although there are several methods that produce relative reflectance.

Image processing to remove atmospheric effects requires both calibration and atmospheric correction. Calibration adjusts the image by converting raw radiance values to absolute or relative reflection values. Atmospheric corrections then adjust these reflectance values for each pixel and wavelength to adjust for some combination of differing path lengths and effects of atmospheric composition (Table 2).

Calibration uses several methods to convert measured values to relative reflectance or absolute reflectance. Flat field calibration, logarithmic residuals (Green and Craig 1985) and internal average relative reflectance (IARR) (Kruse 1988) produce relative reflectance spectra. Flat field calibration is used to normalize images to an area of known reflectance on the ground. The method divides the ground reference spectra into the image spectra for each band, then uses the resultant ratios to calculate the relative reflectance at each pixel. IARR calibration is used to normalize images to a scene's average spectrum. This is effective for reducing imaging spectrometer data to relative reflectance in an area where no ground measurements exist and little is known about the scene. An average spectrum is calculated from the entire scene; this is then used as the reference spectrum and divided into the measured spectrum at each pixel of the image to estimate relative reflectance. If this method must be used, it operates best in arid areas with no vegetation.

Empirical line calibration and calibration to an atmospheric model are methods for estimating apparent (absolute) reflectance. Empirical line calibration is used to force image data to match selected field reflectance spectra and requires *a priori* knowledge of a site (Conel et al. 1987).

Reference field or laboratory spectra are collected for known locations that cover the full range of spectral variation in the image. Specific pixels from the image are associated with these reference spectra and linear regression is used to calculate the gain and offset needed to convert the digital number for each image band to reflectance. This is equivalent to removing the solar irradiance and the atmospheric path radiance. The instrument digital numbers are then converted to reflectance using the gain and offset values. Of the empirical methods, this produces spectra that are most comparable with field or laboratory spectra.

Calibration to apparent (absolute) reflectance can be made using an appropriate atmospheric model (Gao et al. 1993). The Atmospheric Removal Program (ATREM) (Gao and Goetz 1990) is a radiative transfer model-based method for calibration to absolute reflectance that requires no ground-based measurement. The method was developed for 224 band AVIRIS data. A three channel ratioing method uses the water vapor absorption bands to calculate the amount of water vapour for each pixel. This produces an image of water vapour concentrations. This image is used with transmittance spectra of atmospheric gases to produce scaled surface reflectance. Similarly, MODTRAN, a radiative transfer model (Berk et al. 1998, 1999) can be used to estimate reflectance (Adler-Golden et al. 1998; Gastil and Melack 1998).

A variety of combination methods have also been used. Clark et al. (1995) used a combination of ATREM and the empirical line method to correct model errors in ATREM by calculating normalization factors for one pixel and then applying them to the rest of the ATREM-corrected image. Goetz et al. (1998) combined ground measurements of spectral irradiance with MODTRAN to derive a model equivalent to an empirical line method correction that did not require uniform ground targets of different reflectance. Goetz et al. (1997) and Boardman (1998) also describe an analytical process, the Empirical Flat Field Optimal Reflectance Transformation (EFFORT) that bootstraps a linear adjustment to apparent reflectance spectra to improve the accuracy of spectra from AVIRIS following calibration with ATREM. This improves the comparison with library-based spectra, the basis of many of the image interpretation methods.

The effect of different methods for calibration and atmospheric correction on the characteristic spectral profile for materials is pronounced. Figure 1 shows the raw digital numbers and atmospherically corrected spectral profile for a pixel measured using the Probe1 hyperspectral instrument. Data analysis to identify materials is sensitive to the calibration method used, particularly when generating spectral libraries from imagery, or comparing images to field or laboratory derived reference spectra. Correction using an atmospheric model is recommended since the resulting data can be used with spectral libraries and are comparable for different images.

Data collection considerations: The amount of field effort needed to collect ground-based data for atmospheric corrections varies from nothing to extensive, depending on the algorithm that is used. The IARR method requires no field data, which eliminates field expenses, but at the cost of accuracy. ATREM is far more accurate than the IARR method and requires no field data, but does require an imaging spectrometer that collects narrow band width data in the water vapor absorption bandwidths. Flat field calibration only requires spectral data from one site. Empirical line

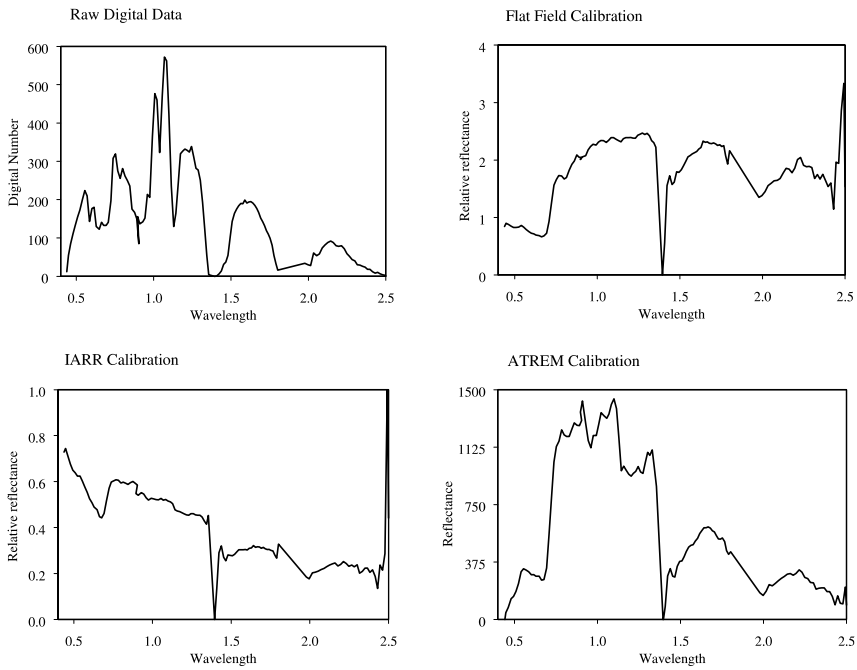

Fig. 1. Probe 1 raw and atmospherically corrected spectral profile

calibration requires a minimum of two ground references sites that represent end members of spectral reflectance, although a number of reference sites along the continuum of reflectance values is preferable. MODTRAN requires extensive ground-based measurements, including RADIOSONDE data to characterise atmospheric thermal structure and water content at different levels.

A number of problems commonly arise with collection of field spectra for atmospheric corrections. Reference targets should be at least 3×3 pixels in size to insure that the center pixel provides a pure signal on the image that is uncontaminated by spectral mixing with adjacent pixels. Finding homogenous features of this size can be difficult, especially in natural settings. Because one is usually trying to collect ground reference data on the day of the flight, one does not have the imagery to guide spectral end member selection for the empirical line approach. Too often one discovers at a later date that the ground sites only represent a portion of the range of spectral reflectances. Finally, the uncertainty in flight timing and difficulties with keeping field teams permanently on alert can mean that there are significant time gaps between ground data collection and image acquisition, which in turn casts doubt on the validity of the ground reference data as a guide to calibrating the image. If ground-based calibrations techniques are going to be used, researchers should therefore spend significant time in the field prior to the flight to locate reference sites that are sufficiently large, that represent light and dark end members, and that are relatively unchanging over time.

Spectral data to develop spectral libraries typically come from laboratory-based spectrometers or portable field spectrometers, all of which are costly to buy or rent and require expert operators. Financial and personnel constraints can thus be a major constraint if equipment and expert operators are not available at reduced cost through research institutes or if existing spectral libraries (Table 3) cannot be used.

4 Geometric Corrections

Analytical approaches: Most hyperspectral imaging systems record spectra using cross track or "whisk broom" sensors, which record the complete spectra for one pixel on the ground before moving ("whisking") to the next pixel. This contrasts with along track (or "push broom") sensors that record multiple spatial instances of a particular spectral band at one time and are more akin to an optical photograph in their geometric characteristics.

Since hyperspectral imaging systems collect data pixel-by-pixel as they scan across track perpendicular to the flight line, the ground location of these pixels can jump dramatically from pixel to pixel due to the pitch, yaw and roll of the aircraft coupled with the cross track scanning of the instrument. Geometric correction of hyperspectral imagery is therefore important in order for the data to be referenced to real world locations and to be used with other spatially referenced data sets. This presents three issues for geometric correction. First, the overall geometry of the imagery is variable since each pixel is collected separately. Standard geometric correction techniques (using n-term polynomial or rubber sheet warping with control points to register images to ground coordinates) is inappropriate and usually unsuccessful (Clark et al. 1998). Second, the pixels may be of variable spatial dimension. Third, there may not be complete coverage of the ground surface. In AVIRIS, which was designed for the relatively stable and predictable motion of the ER-2 platform flying at 20 km elevation, the sensor scanning frequency is tuned to the forward motion of the platform and images are spatially continuous with constant pixel size. Airborne hyperspectral instruments in other platforms are sensitive to the motion of the platform (Boardman 1999).

Clark et al. (1998) and Boardman (1999) have presented methods for geometric correction of hyperspectral imagery from on-board navigation devices. Clark et al. (1998) use a series of equations to correct AVIRIS for the motion of the ER-2 platform, although they do not correct for topographic effects (e.g. changes in elevation). Boardman (1999) uses an onboard Global Positioning System/Inertial Navigation System, C-MIGITS-II to obtain x,y,z (from the GPS) and 3-axis attitude data (from the INS) to

Table 3. Reference libraries for spectra

Features in library	Reference	Library source
Minerals	Clark et al. (1993)	http://speclab.cr.usgs.gov
Minerals	Grove et al. (1992)	http://speclib.jpl/nasa.gov
2000 natural and man-made materials		http://speclib.jpl/nasa.gov
Vegetation	Clark et al. (1993)	http://speclab.cr.usgs.gov

develop and apply a full photogrammetric camera model for low altitude AVIRIS data. The model uses ray-tracing to locate each pixel on the ground surface, a digital elevation model providing ground elevation data. The output is ortho-corrected with full (x,y,z) geo-referencing for each pixel (Boardman 1999). This method has potential for application to any hyperspectral image data, provided GPS/INS data are collected at a frequency that matches the scan frequency of the imaging device and can be digitally tied to the imagery using a common time reference.

The ray-tracing technique is a powerful technique that is both accurate and precise. It is also complex, however, and is not presently built into commercial software. Researchers wanting to use the technique must therefore contract through the commercial vendor that developed it. If the ray-tracing technique is not available because of instrument or logistical constraints, one must then choose between less than optimal solutions. If the plane experienced significant turbulence, the standard polynomial transfer functions are particularly inappropriate because they assume linear or curvilinear variations in pixel location across the entire image, when in fact the image locations vary in a non-linear manner. In this case, a local triangulation technique is preferable, with multiple local control points (e.g. trees) being used to segment the image into triangles, with the images within each triangle being stretched to fit that local surface.

Data collection considerations: HSRH imagery poses particularly severe constraints on the geographic precision required to coregister ground-based maps and pixel locations on images. Locational inaccuracies of only 0.5–1 m can lead to mismatches between image pixels and field maps with high spatial resolution data (Wright et al. 2000; Marcus et al. 2001). When supervised classification techniques are used, this mismatch of image pixels and ground features associates the wrong spectra with ground features, which in turn generates significant inaccuracies in image classification.

Avoiding these mismatches is particularly difficult with HSRH imagery. Even if the image is georeferenced to ± 2 m using the ray-tracing approach, it is difficult to locate features on the ground with this degree of accuracy, especially in natural settings without bench marks, intersections, and features that have well identified point locations. Considerable pre-flight planning should therefore be devoted to considerations of image and map overlay.

The optimal and most accurate approach to precise coregistration of imagery and maps is to map directly to the imagery, using the imagery like an air photo. This is not possible in many cases, however, because researchers often want to map as close to the flight date as possible to insure that mapped features (e.g., stream depths, vegetation cover, soil moisture, etc.) represent conditions shown on the imagery. Some operators of hyperspectral sensors cannot provide imagery rapidly, while others can have same day turn around under the appropriate circumstances. If mapping directly to imagery is a desired method, users should query sensor operators about the turn around time that is required and make this part of the data contract.

Precision location can also be accomplished by placing targets in the field that show up clearly on images. This works well for marking the corners of sample grids or the ends of transects. We have found that 2×2 m plastic ground tarps show up well in natural landscapes with pixel resolutions as large as 5 m. The tarps saturate the pixel spectra, particularly in near

infrared bands where the plastic reflectance is radically different than the natural background materials.

One can also do precision mapping using classic field survey equipment or GPS. Unless ground truth sites exist that cover many pixels, however, we do not recommend this approach. Ground map precisions as tight as $+0.5$ m challenge GPS and survey techniques unless field teams are willing to expend significant time, which in turn limits the amount of ground data that can be collected. Second, even with sub-meter precision and accuracy in the ground map, it is almost impossible (even with ray-tracing) to generate comparable precision in the image, unless meter scale DEMs are available. Coregistration of imagery and field maps may therefore still be inaccurate. To overcome this problem, ground truth sites that cover many pixels should be mapped. This allows boundary pixels where overlap errors occur to be discarded from overlay analysis. Unfortunately, many features (e.g., a particular vegetation type such as willows) may not cover multiple pixels even on HSRH-imagery.

Finally, with hyperspectral data, it may not be necessary to have precise locations for ground sites. As noted previously, if a feature has a clear spectral signature, the feature can be detected using spectral matching techniques discussed below. Given the severe coregistration problems associated with HSRH-imagery, this spectral matching approach should be seriously considered as an alternative to supervised classification whenever hyperspectral data are available.

5 Data analysis

Hyperspectral imagery presents a number of opportunities for interpretation and analysis and can make use of methods beyond the standard statistically-based image classification methods used in multi-spectral remote sensing. Multispectral images are often analysed using multivariate statistical classifiers that treat individual wavebands in the imaging instrument as a series of independent variables. These "standard" methods for image classification can be applied to hyperspectral imagery although statistical classification of high-dimensional data that exhibits correlation between spectral bands fails to take full advantage of the key feature of the imagery, namely that it provides access to a measurement of a near complete spectrum for each pixel using narrow wavebands. The data provided by calibrated hyperspectral imagery are comparable with laboratory spectra measured for materials. These reference spectra provide digital 'lookup' keys to the composition of pixels and provide a direct measurement of the material being sensed.

A number of specialised methods have been developed to take advantage of the characteristic spectra of materials and there are several reference spectral libraries that provide descriptions of the spectra of materials (Table 3). Further libraries tailored to specific applications of hyperspectral imagery are needed to complement the libraries organised around classes of materials. For example, for health related applications, libraries may be developed that contain spectra for characteristics of habitats that are known to have a close association with vectors of diseases. Kitron et al. (1996) use Landsat Thematic Mapper data and GIS to investigate the distribution of tsetse flies in Kenya and the approach could be extended to hyperspectral imagery with appropriate spectral libraries. Analysis of hyperspectral

imagery usually requires an empirical match to be made between the image spectra and a set of reference spectra (end-members) from a spectral library for known materials. Reference spectra can be measured in the laboratory or field; they may also be derived from the hyperspectral imagery itself.

Analysis methods focus either on a) classifying each pixel into a single class by identifying the main material in the pixel, or b) estimating the composition of a pixel using an un-mixing method that identifies multiple materials and their relative abundance within a pixel.

5.1 Single feature identification

There are four main methods for identifying single feature types within hyperspectral imagery:

a) binary encoding,
b) continuum removal,
c) spectral angle mapper, and
d) spectral feature fitting.

Binary encoding: Binary encoding (Mazer et al. 1988) is a classification method that encodes the image data and reference spectra into 0 s and 1s based on whether a band falls below or above the spectrum mean. An exclusive OR function is then used to compare each encoded reference spectrum with the encoded image spectra and classify the image. Each pixel is classified to the material with the greatest number of bands that match, above a minimum match threshold.

Continuum removal: Continuum removal normalizes reflectance spectra to allow comparison of individual absorption features from a common baseline (Kruse et al. 1985; Clark et al. 1987; Kruse et al. 1993a). A convex hull that is fitted to the spectrum describes the continuum. Straight-line segments connect local spectra maxima to define the convex hull, the first and last spectral data values being on the hull by definition.

Spectral angle mapper: The Spectral Angle Mapper (Kruse et al. 1993b) matches pixel spectra to reference spectra using a measure of spectral similarity based on the angle between the spectra treated as vectors in an n-dimensional space with dimensionality, n, equal to the number of image bands. Smaller angles represent closer matches. The angle between each pixel and all reference spectra can be mapped and pixels assigned to the material for which the spectral angle is smallest and within a defined limiting angle. When used on calibrated reflectance data, the spectral angle mapper is relatively insensitive to effects of illumination and albedo since the angle between vectors is measured rather than the length of the vector.

Spectral feature fitting: Spectral Feature Fitting uses least squares methods to compare the fit of image spectra to selected reference spectra (Clark et al. 1990, 1991; Crowley and Clark 1992; Swayze and Clark 1995). Reference spectra are scaled to match the image spectra after continuum removal from both data sets. The method measures absorption feature depth which is related to material abundance.

5.2 Un-mixing methods

Un-mixing methods take advantage of the high-dimensionality of the hyperspectral data to identify sub-components of the spectrum for each pixel. These methods identify the relative contribution of different materials to the spectral composition of a given pixel. They thus provide the capability to map sub-pixel features and abundance of different materials. There are three main methods for un-mixing:

a) matched filtering,
b) spectral un-mixing/spectral mixture analysis, and
c) mixture tuned matched filtering.

Matched filtering: The Matched Filtering method is described by Harsanyi and Chang (1994) and Boardman et al. (1995). Matched filtering performs a partial un-mixing of spectra to estimate the abundance of user-defined end-members from a set of reference spectra. Matched filtering does not require knowledge of all the end-members within an image scene and can also be used to identify single feature types.

Spectral un-mixing/spectral mixture analysis: Spectral un-mixing (Boardman, 1989, 1993) determines the relative abundance of materials based on the spectral characteristics of materials. Reflectance in each image pixel is treated as a linear combination of the reflectance of each end-member present within the pixel. The number of end-members must be less than the number of spectral bands and all of the end-members represented in the image must be used. Boardman (1989) applies singular value matrix decomposition to un-mix hyperspectral data. Spectral libraries provide the initial data matrix to this method.

Mixture tuned matched filtering: Boardman (1998) describes mixture tuned matched filtering (MTMF), a method that builds on the strengths of matched filtering and spectral un-mixing. MTMF combines the ability to map a single known target without knowledge of all end-member signatures with the leverage of mixed pixel models including constraints on feasibility. MTMF also reduces the incidence of false positives.

6 Opportunities for spatial analysis of high spatial resolution hyperspectral imagery

The methods described for analysis of hyperspectral imagery identify materials based solely on the analysis of spectra. The spatial component of hyperspectral imagery offers an additional feature of the data with potential for application in interpretation and mapping of landscape objects. Spatial analysis may help in at least two ways. First, the spatial structure of spectral information in imagery can be used to augment spectral based analysis. Pinzon et al. (1998) and other papers in this issue address the use of spatial analysis as a complement to spectral analysis. Second, spatial analysis may be used to interpret the distribution of materials identified from the imagery by spectral analysis to map and model environmental objects of interest.

References

Adler-Golden SM, Berk A, Bernstein LS, Richtsmeierl S, Acharyal PK, Matthew MW, Anderson GP, Allred CL, Jeong LS, Chetwynd JH (1998) FLAASH, A MODTRAN4 atmospheric correction package for hyperspectral data retrievals and simulations. *AVIRIS 1998 Proceedings*, JPL, California. 6pp. (http://makalu.jpl.nasa.gov/docs/workshops/98_docs/2.pdf)

Berk A, Bernstein LS, Anderson GP, Acharya PK, Robertson DC, Chetwynd JH, Adler-Golden SM (1998) MODTRAN cloud and multiple scattering upgrades with application to AVIRIS. *Remote Sensing of Environment* 65:367–375

Berk A, Anderson GP, Bernstein LS, Acharya PK, Dothe H, Matthew MW, Adler-Golden SM, Chetwynd JH Jr, Richtsmeier SC, Pukall B, Allred CL, Jeong LS, Hoke ML (1999) MODTRAN4: Radiative transfer modeling for atmospheric correction. *AVIRIS 1999 Proceedings*, JPL, California. 7 pp (http://makalu.jpl.nasa.gov/docs/workshops/99_docs/6.pdf)

Boardman JW (1989) Inversion of imaging spectrometry data using singular value decomposition. *Proceedings, IGARSS'89, 12th Canadian Symposium on Remote Sensing*, 4:2069–2072

Boardman JW (1993) Automated spectral unmixing of AVIRIS data using convex geometry concepts. *Summaries, 4th JPL Airborne Geoscience Workshop*, JPL Publication 93-26, 1:11–14

Boardman JW (1998a) Post-ATREM polishing of AVIRIS apparent reflectance data using EFFORT: a lesson in accuracy versus precision. *AVIRIS 1998 Proceedings*, JPL, California. 1pp. (http://makalu.jpl.nasa.gov/docs/workshops/98_docs/7.pdf)

Boardman JW (1998b) Leveraging the high dimensionality of AVIRIS data for improved subpixel target unmixing and rejection of false positives: Mixture tuned matched filtering. *AVIRIS 1998 Proceedings*, JPL, California. 6 pp (http://makalu.jpl.nasa.gov/docs/workshops/98_docs/8.pdf)

Boardman JW (1999) Precision geocoding of low altitude AVIRIS data: lessons learned in 1998. *AVIRIS 1999 Proceedings*, JPL, California. 6pp. (http://makalu.jpl.nasa.gov/docs/workshops/99_docs/7.pdf)

Boardman JW, Kruse FA (1994) Automated spectral analysis: A geologic example using AVIRIS data, north Grapevine Mountains, Nevada *Proceedings, 10th Thematic Conference on Geologic Remote Sensing*, Environmental Research Institute of Michigan, Ann Arbor, MI, p. I-407–I-418

Boardman JW, Kruse FA,Green RO (1995) Mapping target signatures via partial unmixing of AVIRIS data. *Summaries, 5th JPL Airborne Earth Science Workshop*, JPL Publication 95-1, 1:23–26

Clark RN, Swayze GA (1995) Mapping minerals, amorphous materials, environmental materials, vegetation, water, ice, and snow, and other materials: The USGS Tricorder Algorithm. *Summaries of the 5th Annual JPL Airborne Earth Science Workshop*, JPL Publication 95-1, pp 39–40

Clark RN, King TVV, Gorelick NS (1987) Automatic continuum analysis of reflectance spectra *Proceedings, 3rd AIS workshop, 2-4 June, 1987*, JPL Publication 87-30, Jet Propulsion Laboratory, Pasadena, California, p 138–142

Clark RN, Gallagher AJ, Swayze GA (1990) Material absorption band depth mapping of imaging spectrometer data using the complete band shape least-squares algorithm simultaneously fit to multiple spectral features from multiple materials. *Proceedings of the 3rd Airborne Visible/Infrared Imaging Spectrometer (AVIRIS) Workshop*, JPL Publication 90-54, pp 176–186

Clark RN, Swayze GA, Gallagher A, Gorelick N, Kruse FA (1991) Mapping with imaging spectrometer data using the complete band shape least-squares algorithm simultaneously fit to multiple spectral features from multiple materials. *Proceedings, 3rd Airborne Visible/Infrared Imaging Spectrometer (AVIRIS) Workshop*, JPL Publication 91-28, pp 2–3

Clark RN, Swayze GA, Gallagher A (1992) Mapping the mineralogy and lithology of Canyonlands, Utah with imaging spectrometer data and the multiple spectral feature mapping algorithm. *Summaries of the 3rd Annual JPL Airborne Geoscience Workshop*, JPL Publication 92-14, v. 1, pp 11–13

Clark RN, Swayze GA, Gallagher A, King TVV, Calvin WM (1993) The US Geological Survey Digital Spectral Library: Version 1:0.2–3.0 mm. *U.S. Geological Survey, Open File Report 93-592*, 1340 p

Clark RN, Livo KE, Kokaly RF (1998) Geometric correction of AVIRIS imagery using on-board navigation and engineering data. *AVIRIS 1998 Proceedings*, JPL, California. 9 pp (http://makalu.jpl.nasa.gov/docs/workshops/98_docs/9.pdf)

Clark RN Swayze GA, Heidebrecht KB, Green RO, Goetz AFH (1995) Calibration to surface reflectance of terrestrial imaging spectrometry data: Comparison of methods. *Summaries of the 5th annual JPL Airborne Earth Science Workshop* 1:41–42

Conel JE, Green RO, Vane G, Bruegge CJ, Alley RE, Curtiss B (1987) Airborne Imaging Spectrometer-2: Radiometric spectral characteristics and comparison of ways to compensate for the atmosphere. *Proceedings SPIE,* 834, pp 140–157

Congalton RG, Green K (1999) *Assessing the Accuracy of Remotely Sense Data: Principles and Practices*. New York, Lewis Publishers, p 137

Crowley JK, Clark RN (1992) AVIRIS study of Death Valley evaporite deposits using least-squares band-fitting methods. *Summaries of the 3rd Annual JPL Airborne Geoscience Workshop*, JPL Publication 92-14, v 1, p 29–31

Gamon JA, Field CB, Roberts DA, Ustin SL, Valentini R (1993) Functional patterns in an annual grassland during an AVIRIS overflight. *Remote Sensing of Environment* 44:239–253

Gamon JA, Field CB, Goulden ML, Griffen KL, Hartley AE, Joel G, Penuelas J, Valentini R (1995) Relationships between NDVI, canopy structure, and photosynthesis in three California vegetation types. *Ecological Applications*, 5:28–41

Gao BC, Goetz AFH (1990) Column atmospheric water vapor and vegetation liquid water retrievals from airborne imaging spectrometer data. *J Geophys Res* 95:3549–3564

Gao BC, Heilbrecht KB, Goetz AGH (1993) Derivation of scaled surface reflectance from AVIRIS data. *Remote Sensing of Environment* 44(2–3):165–178

Gastil M, Melack JM (1998) Improved atmospheric correction for AVIRIS spectra from inland waters. *AVIRIS 1998 Proceedings*, JPL, California. 9 pp (http://makalu.jpl.nasa.gov/docs/workshops/98_docs/19.pdf)

Goetz AFH, Vane G, Solomon JE, Rock BN (1985) Imaging spectrometry for earth remote sensing science. *Science* 228:1147–1153

Goetz AFH, Boardman JW, Kindeland B, Heidebrecht KB (1997) Atmospheric corrections: On deriving surface reflectance from hyperspectral imagers. *Proceedings SPIE*, 3118, pp 14–22

Goetz AFH, Heidebrecht KB, Kindell B, Boardman JW (1998) Using ground spectral irradiance for model correction of AVIRIS data. *AVIRIS 1998 Proceedings*, JPL, California. 10 pp (http://makalu.jpl.nasa.gov/docs/workshops/98_docs/22.pdf)

Gove PB (1976) *Webster's 3rd New International Dictionary of the English Language Unabridged*: G.&C. Merriam Company, Springfield, MA, p 2662

Green AA, Craig MD (1985) Analysis of aircraft spectrometer data with logarithmic residuals. *Proceedings, AIS workshop, 8–10 April, 1985,* JPL Publication 85-41, Jet Propulsion Laboratory, Pasadena, California, pp 111–119

Grove, CI, Hook SJ, Paylor II ED (1992) Laboratory reflectance spectra of 160 minerals, 0.4 – 2.5 μm. *Jet Propulsion Laboratory Pub*. 92-2

Harsanyi JC, Chang CI (1994) Hyperspectral image classification and dimensionality reduction: An orthogonal subspace projection approach. *IEEE Transactions on Geoscience and Remote Sensing* 32:779–785

Kitron U, Otieno LH, Hungerford LL, Odulaja WU, Brigham OO, Okello M, Joselyn MM, Ahmed M, Cook E (1996) Spatial analysis of the distribution of tsetse flies in the Lambwe Valley, Kenya, using TM satellite imagery and GIS. *Journal of Animal Ecology* 65:371–380

Kruse FA (1988) Use of Airborne Imaging Spectrometer data to map minerals associated with hydrothermally altered rocks in the northern Grapevine Mountains, Nevada and California. *Remote Sensing of Environment* 24(1):31–51

Kruse FA (1994) Imaging spectrometer data analysis: A tutorial. *International Symposium on Spectral SensingResearch '94,* San Diego, CA, 9 July 1994

Kruse FA, Lefkoff AB (1993) Knowledge-based geologic mapping with imaging spectrometers. *Remote Sensing Reviews* 8:3–28

Kruse FA, Raines GL, Watson K (1985) Analytical techniques for extracting geologic information from multichannel airborne spectroradiometer and airborne imaging spectrometer data. *Proceedings, International Symposium on Remote Sensing of Environment, Thematic Conference on Remote Sensing for Exploration Geology, 4th*, Environmental Research Institute of Michigan, Ann Arbor, pp. 309–324

Kruse FA, Lefkoff AB, Dietz JB (1993a) Expert System-based mineral mapping in northern Death Valley, California/Nevada using the Airborne Visible/Infrared Imaging Spectrometer (AVIRIS). *Remote Sensing of the Environment*, 44:309–336

Kruse FA, Lefkoff AB, Boardman JB, Heidebrecht KB, Shapiro AT, Barloon PJ, Goetz AFH (1993b) The spectral image processing system (SIPS)–Interactive visualization and analysis of imaging spectrometer data. *Remote Sensing of Environment* 44:145–163

Marcus WA, Marston RA, Colvard CR Jr, Gray RD (2002) Mapping the spatial and temporal distributions of large woody debris in rivers of the Greater Yellowstone Ecosystem, U.S.A. *Geomorphology (in press)*

Mazer AS, Martin M, Lee M, Solomon JE (1988) Image processing software for imaging spectrometry data analysis. *Remote Sensing of Environment* 24:201–210

Palacios-Oreuta A, Ustin SL (1996) Multivariate statistical analysis of soil spectra. *Remote Sensing of the Environment* 57:108–118

Pinzon JE, Ustin SL, Pierce JF (1998) Robust feature extraction for hyperspectral imagery using both spatial and spectral redundancies. *AVIRIS 1998 Proceedings*, JPL, California. 27 pp (http://makalu.jpl.nasa.gov/docs/workshops/98_docs/43.pdf)

Roberts DA, Smith MO, Adams JB (1993) Green vegetation, non-photosynthetic vegetation, and soils in AVIRIS data. *Remote Sensing of Environment* 44:255–269

Swayze GA, Clark RN (1995) Spectral identification of minerals using imaging spectrometry data: evaluating the effects of signal to noise and spectral resolution using the tricorder algorithm. *Summaries of the 5th Annual JPL Airborne Earth Science Workshop*, JPL Publication 95-1, pp 157–158

Ustin SL, Hart QJ, Duan L, Scheer G (1996) Vegetation mapping on hardwood rangelands in California. *Int J Remote Sensing* 17:3015–3036

Ustin SL, Smith MO, Jacquemoud S, Verstraete MM, Govaerts Y (1999) Geobotany: vegetation mapping in Earth Sciences. In: Rencz A (ed) *Manual of Remote Sensing: for the Earth Sciences*. American Society of Photogrammetry and Remote Sensing, Bethesda, Maryland 3:189–248

Wright A, Marcus WA, Aspinall R (2000) Applications and limitations of using multispectral digital imagery to map geomorphic stream units in a lower order stream. *Geomorphology* 33:107–120

Site Characterization of Mine Tailings at the INCO Copper Cliff Tailings Impoundment Area using *casi* Imagery*

J. Lévesque[1] V. Singhroy[2], K. Staenz[2], and D. Bolton[3]

[1]MIR Télédétection Inc.
2182 de la Province, Bureau 208, Longueuil, Québec, Canada, J4G 1R7
Phone: (613) 947-1284, Fax: (613) 947-1385, E-mail: josee.levesque@ccrs.nrcan.gc.ca

[2]Canada Centre for Remote Sensing
588 Booth Street, Ottawa, Ontario, Canada, K1A 0Y7

[3]INCO Limited
Copper Cliff, Ontario, Canada, P0M 1N0

ABSTRACT

Hyperspectral imagery from the Compact Airborne Spectrographic Imager (*casi*) in the visible and near infrared was used to characterize mine tailings at the INCO Copper Cliff tailings impoundment area. The objective of the study described in this paper is to evaluate the usefulness of high spatial and spectral resolution data and analysis techniques for characterizing and monitoring such sites. Flight data were acquired in late August 1996 in 72 contiguous 9 nm wide spectral bands from 400 nm to 950 nm along with a detailed ground survey. The ground survey involved a visual characterization of the site and collection of ground truth spectra using a GER 3700 spectrometer operating between 400 nm and 2500 nm. Images were classified using a spectral matching technique. The site is well characterized by this technique and independent ground data support these results.

1. INTRODUCTION

The reduction of acidic drainage from mine tailings sites and their environmental restoration is a growing concern for many mine operators. When exposed to air and water, tailings oxidize and produce sulfuric acid which liberates the heavy metals already in great amount in the tailings (University of Missouri, 1997). Because of their high level of contamination in heavy metals and other toxic substances related to mining exploitation, it is difficult to revegetate such sites. One of the techniques used to revegetate mine tailings is to spread lime to reduce the level of acidity and thus allow certain tolerant species to initiate the process of revegetation. The success of mine tailings revegetation greatly depends on the quality of monitoring the tailings in order to ensure an efficient process on a long term basis.

The objective of the study was to evaluate the usefulness of high spatial and spectral resolution data and their analysis techniques for characterizing and monitoring mine tailings sites. Hyperspectral remote sensing offers data from sophisticated sensors that provide the

*Presented at the International Symposium: Geomatics in the era of RADARSAT. Ottawa, May 25-30, 1997.

level of spectral and spatial detail necessary to discriminate different types of surfaces such as vegetated areas, limed areas, exposed tailings, and any mixture of these surfaces.

Hyperspectral imagery from the Compact Airborne Spectrographic Imager (*casi*) in the visible and near infrared was used to characterize the mine tailings site at the INCO Copper Cliff tailings impoundment area in Sudbury. This site was chosen because of its well initiated revegetation program by INCO company (INCO Ltd, 1997) and earlier work conducted by Singhroy (1995a, 1995b, 1997). It contains a large variety of mine tailings, different levels of vegetation regrowth, as well as limed and non-limed areas. The image was classified using spectral matching.

2. METHODOLOGY

Ground survey

The ground survey included a visual characterization of the site and the collection of field spectra using a GER 3700 spectrometer operating between 400 nm and 2500 nm. Spectra of oxidized and non-oxidized (fresh) mine tailings of different composition (pyrite, pyrrhotite), green and dry vegetation, lime, straw, and rock were collected in August 1996. These spectra as well as the visual assessment were used to validate the results of the image classification.

casi imagery

High spatial and spectral resolution *casi* data were acquired in the visible and near infrared and calibrated to radiance. Flight data were acquired on August 24, 1996 in 72 contiguous 9 nm wide spectral bands covering a wavelength range from 400 nm to 950 nm. The radiance data were multiplied by a factor of 1000 to achieve digital counts. Prior to the data analysis, a roll correction was applied using the navigation data to remove first-order geometric effects due to aircraft motion.

Preclassification processing of image data

In order to reduce the number of bands and thus the redundancy in the data, a Minimum Noise Fraction Transformation (MNFT) was performed on the data cube. This transformation gives similar results as Principal Components but, besides reducing the amount of data, it also reduces their noise content (Research Systems Inc., 1997). For the Copper Cliff mine tailings site, the first four components as well as the 6th and 7th MNFT features were kept for classification purposes. The 5th MNFT feature displays strong noise and, therefore, was not used in the classification.

Classification using the Spectral Angle Mapper (SAM)

SAM is a spectral matching technique that classifies spectra on a pixel basis according to its resemblance to a reference or end-member spectrum. An end-member spectrum represents a pure pixel, which is composed of a single material (e.g. lime) rather than a mixture of two or more materials (e.g. lime, soil, and grass) (Boardman, 1995). Its spectrum represents a pure material and can be used as a reference spectrum for that specific material. Most pixels in an image are a mixture of many end-members. The SAM method uses an algorithm that calculates the spectral angle between the reference spectrum and the spectrum to be classified. It projects the spectra as vectors in space with a dimension that is equal to the number of bands (Research Systems Inc., 1997). Figure 1 shows a simplified two dimensional representation of the SAM method where two materials are compared using two spectral bands. SAM considers the direction of the vectors and not their length. Since the length of the vectors is related to the degree of illumination, SAM is not sensitive to illumination since only the direction of the vectors (colour) is taken into account when calculating the spectral angle. The resulting product of SAM classification is a series of angle images, one for each end-member, where each pixel is assigned an angle value. The smaller the angle, the more similar is the pixel spectrum to the end-member spectrum.

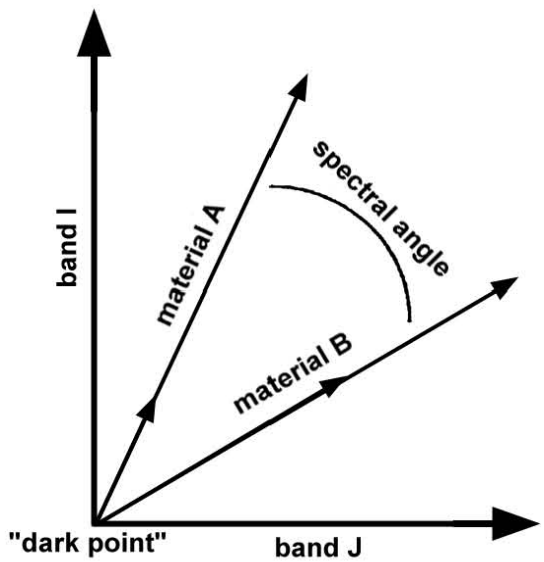

Figure 1. Two-dimensional example of the Spectral Angle Mapper (SAM) (Research Systems Inc., 1997)

End-member collection

End-member spectra were collected from the image data using the purest pixel determined by the Pixel Purity Index (PPI) (Research Systems Inc., 1997). Three end-members were chosen for the classification: mine tailings, limed areas, and vegetation. The grass and trees were incorporated into the same class (vegetation).

3. RESULTS AND DISCUSSION

Colour composites and image spectra

Figure 2 shows a colour composite of the *casi* image acquired over the Copper Cliff mine tailings. The bands displayed are 737 nm in red, 676 nm in green, and 540 nm in blue. The end-members are identified in the image and are illustrated with a ground-level image.

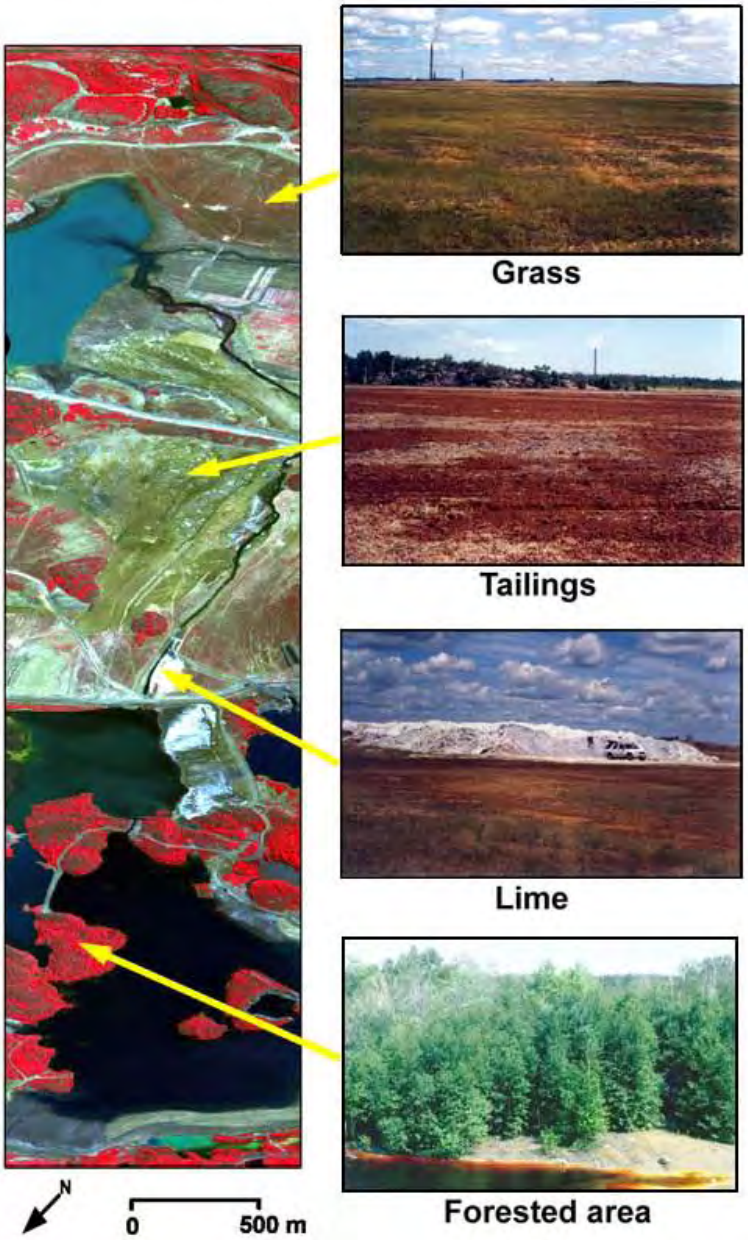

Figure 2. Colour composite (*casi* bands 737nm, 676 nm, 540 nm) showing the three end-members. Note that in the analysis, grass and forested area form one end-member (vegetation).

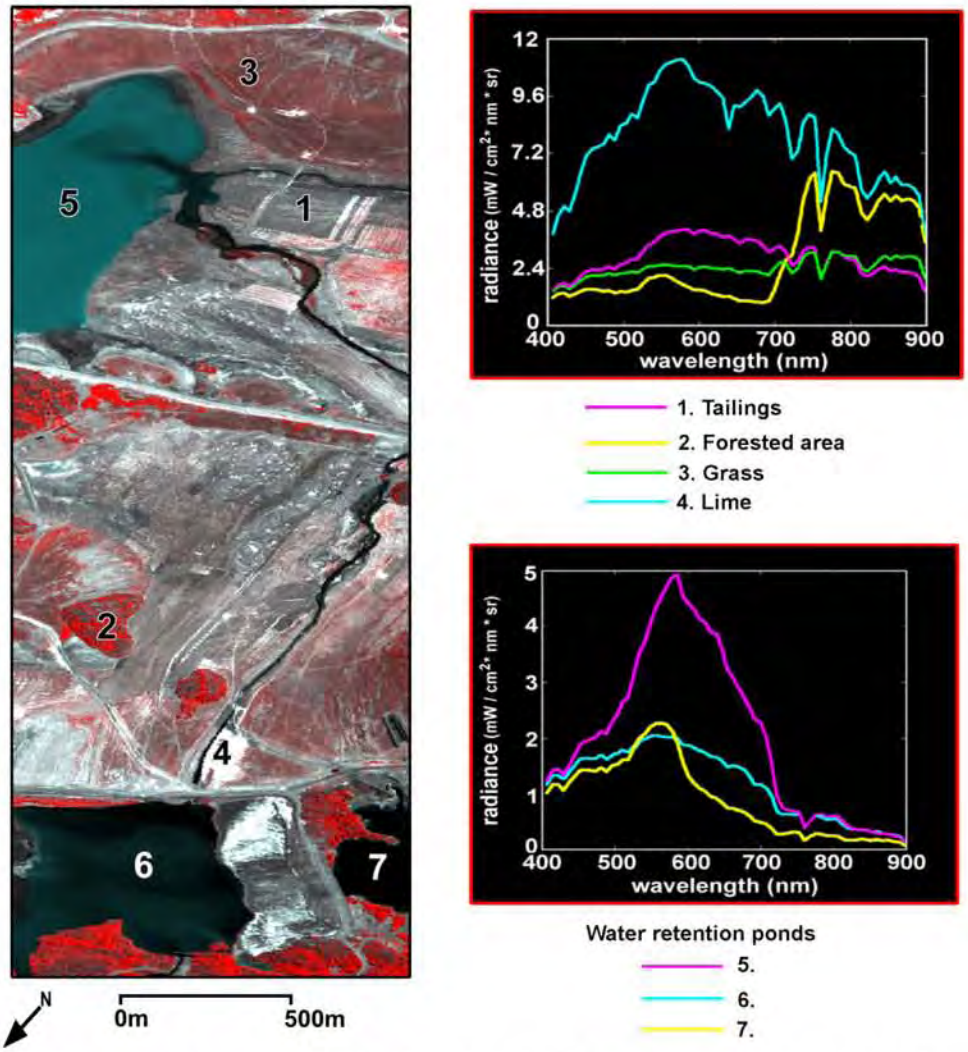

Figure 3. Colour composite (*casi* bands 737 nm,684 nm, 684 nm) and spectra extracted from the *casi* image.

Figure 3 displays bands 737 nm, 684 nm and 684 nm in red, green, and blue, respectively. This colour composite facilitates the visual discrimination between vegetation (red), lime (white) and tailings (gray). Spectra of the three end-members were extracted from the image data (upper graph). The spectra were extracted from the tailings, forested area and grass (same end-member), and lime. Note the similar shape of the tailings and the grass spectra. As shown in the grass picture in Figure 2, the grass areas are composed of dry and green grass with patches of tailings which can explain their resemblance. The lime spectrum appears very bright in all wavelengths. The lower graphic shows the spectra of the three water ponds included in the image. Their different shapes and amplitudes indicate that contiguous spectra, as provided with hyperspectral data, allow a good discrimination between different water composition.

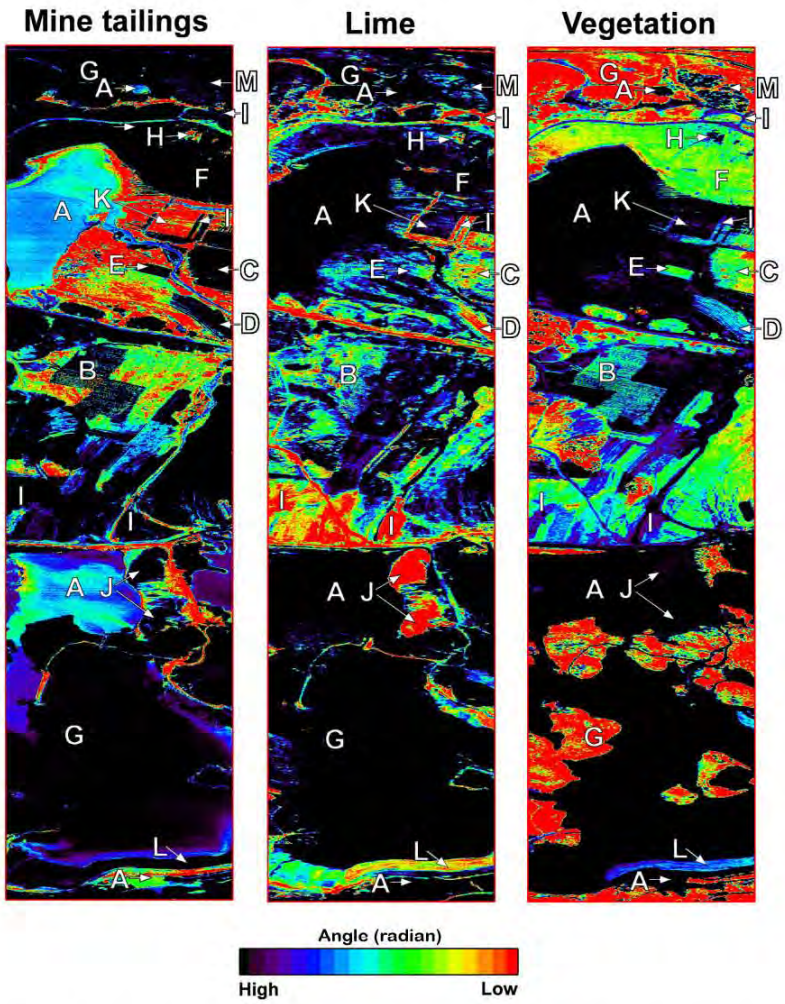

Figure 4. Results of the Spectral Angle Mapper classification.

Note the well defined tailings area surrounded by lime (K). It is also interesting to note that the roads are mainly composed of tailings and lime which shows the possibility that the contamination could be spread through human transportation means.

Vegetation and lime are mixed in area labeled L. This area appears as a band following the shoreline. From the ground observations this area is composed mainly of lime and straw, a material used to produce top soil organic matter and retain soil moisture. Straw is dry organic vegetation matter so it appears blue (low biomass) in the vegetation end-member image. The lime content is fairly high (mainly yellow) and no tailings (black) are seen through it.

The area of rock outcrop labeled as M was not chosen as an end-member. However, some of its surface is slightly covered by lime and vegetation. Since lime was not intentionally spread on this area, it suggests that airborne contamination from area to area can be present. This should be taken into account in future analysis.

SAM classification results

The images in Figure 4 display the similarity of each pixel spectra to the given end-member spectra. They should be compared to the images of Figures 2 and 3. Pixel values represent the spectral angle in radians measured from the end-member spectra. The lowest angle values represent the most similar pixel spectra to the end-member spectra and are displayed in red. The highest angle values represent the least similar pixel spectra to the end-member and are displayed in black. Any angle values in between are allocated a colour displayed in the colour scale as shown in Figure 4.

Figure 4 shows the mine tailings, lime and vegetation end-member images. Because no end-member was collected for water, it is normal that this class is not part of the results. The water bodies appear black in the three displayed end-member images. However, the three water ponds labeled as A appear as light blue in the tailings end-member image and black in the lime and vegetation images indicating that they relate slightly to mine tailings in their composition.

There is a pattern of two rectangular polygons that emerge in the centre part of the images (B) of the tailings and vegetation end-members. This pattern is not present in the lime end-member image but some lime is present in some parts of the area. It represents an area of seedling, partly limed, containing a very small amount of grass (light blue in vegetation image).

The C label shows a limed area where grass grows in different concentration over the lime. Note that this area appears black in the tailings end-member image indicating that the tailings surface is completely covered by lime and vegetation. The places where the vegetation end-member image displays a red colour (high amount of vegetation) appear black in the lime end-member image. The ground survey indicates that the amount of vegetation on these patches is high enough to cover the entire limed surface, thus showing a certain level of success in the revegetation process. The same thing is happening to a lesser extent in the D and E areas.

The area labeled as F shows a grass area. Compared to tree areas (G), grass areas do not cover as much ground as forested areas and are composed of dry and green grass so that the amount of green vegetation present in the pixels of these areas is less than in pixels of the forested areas. Thus, treed areas appear red while grass areas range from light blue to yellow and occasionally red as on the C area.

The area labeled as H shows an incursion of tailings into the grass area. This patch of tailings is mixed with lime as shown on the tailings and lime end-member images.

High lime content (I) is well expressed by the red colour in the lime end-member image except for the two J areas where the high lime content values are related to dry pyrrhotite tailings. This illustrates how hyperspectral imagery can be used to differentiate tailings surface features over large areas once validated through ground observation.

4. CONCLUSIONS

This study has demonstrated the usefulness of hyperspectral *casi* data to characterize mine tailings sites. Mine tailings, limed surfaces and vegetation can be well characterized assuming that ground observation is present to validate the results. The results thus far are promising. However, further investigation should be made to address the following issues: (1) results should be compared for end-members extracted from the image and those collected from the ground to see if the results can be improved; (2) other analysis methods such as spectral unmixing and matched filter should be investigated; (3) knowledge of the chemical composition of the water bodies on the Copper Cliff mine tailings site would help in deciding whether hyperspectral remote sensing can be used to estimate the degree of contamination of the water bodies on mine tailings sites as well as any leakage from the tailings areas; (4) end-member images should be calibrated so that different years of monitoring can be compared.

5. REFERENCES

Boardman, J.W. (1995) "Analysis, understanding and visualization of hyperspectral data as convex sets in n-space". SPIE, vol. 2480, pp. 14-21.

Research Systems Inc. (1997). "ENVI User's Guide: The environment for visualizing images". Version 2.6, January 1997 edition, Limited Liability Company, Lafayette, Colorado.

INCO Ltd (1997). "Tailings and revegetation". Web site: http://www.incoltd.com/invest/10k/10k-034g.htm.

Singhroy, V. (1995a). "Spectral characterization of vegetation at mine tailings." Proceedings: Mining and the Environment, Sudbury'95, Sudbury, Ontario, pp.193-200.

Singhroy, V. (1995b). "Environmental and geological site characterization in vegetated areas: Image enhancement guidelines." Remote Sensing and GIS: Applications and Standards. ASTM Special Technical Publication #1279. V. Singhroy, D. Nebert and A. Johnson, Eds., American Society for Testing and Materials, pp. 5-17.

Singhroy, V. (1997). "Satellite and airborne sensing to characterize mining areas - selected sites in Canada." in Remote Sensing for Site Characterization. Eds Kuhn et al., Springer Verlag, NY, pp. 229-243.

University of Missouri (1997). What is acid mine drainage? Web site: http://www.umr.edu/~mcox/oure/Intro.html.

Spectral Band Selection from *casi* Data for Monitoring Mine Tailings Site Rehabilitation

Josée Lévesque
MIR Télédétection Inc., 2182 de la Province, Longueuil, QC, J4G 1R7, Canada
Email : levesque@ccrs.nrcan.gc.ca

Tom Szeredi
MacDonald Dettwiler and Assoc., 13800 Commerce Parkway, Richmond, BC, V6V 2J3, Canada

Karl Staenz, Vern Singhroy
Canada Centre for Remote Sensing, 588 Booth St., Ottawa, ON, K1A 0Y7, Canada

Abstract – **This paper investigates the effect of varying bandwidth and number of bands on spectral unmixing results of *casi* data acquired over a mine tailings site. Forthcoming high spatial resolution sensors with less bands and larger bandwidths such as Quickbird, Ikonos1 and Orbview3 were simulated in order to determine whether the similar unmixing results can be achieved as with the 68-band *casi* data.**

1. INTRODUCTION

Canadian liability for acid mine drainage is in the order of $2 billion to $5 billion depending on the technique used to dispose of and treat the acidic waste (MEND). In the Sudbury area alone, Inco Ltd. spends an annual $5 million to reclaim property (Inco Ltd.). Given these enormous costs, monitoring techniques are needed to evaluate the efficiency of the techniques used to revegetate mine tailings sites. In a previous study, Lévesque et al. (1997) demonstrated the monitoring capability of the Compact Airborne Spectrographic Imager (*casi*) over the Sudbury mine tailings area. If long term monitoring is required airborne surveys can become quite expensive. The question is whether one can achieve similar results using forthcoming high spatial resolution satellites such as Quickbird, Ikonos1, and Orbview3 (Table 1). The spatial resolution of these sensors is similar to that of the *casi* data acquired over the Sudbury mine tailings site (2.3 m by 4.3 m). However, these sensors have fewer spectral bands and their bands are wider than those of the *casi* dataset used in this study. This paper investigates the effect of varying bandwidth and number of bands on spectral unmixing results. Finally, four Quickbird bands and related bandwidths were simulated in order to evaluate their possible monitoring capability. Since Orbview3 and Ikonos1 have basically the same spectral configuration as Quickbird the results obtained for Quickbird are assumed to be applicable to these sensors also.

Table 1. Spectral band configuration and spatial resolution for the Quickbird, Orbview3 and Ikonos sensors.

Sensor	Quickbird	Orbview3	Ikonos1
Company	Earthwatch	Orbital Sciences	Space Imaging
Spectral bands (nm)	450 - 520 530 - 590 630 - 690 770 - 900	450 - 520 520 - 600 625 - 695 760 - 900	450 - 520 520 - 600 630 - 690 760 - 900
Spatial resolution	3.2 m	4 m	4 m

2. METHODOLOGY

2.1 Image data

Hyperspectral *casi* radiance data were acquired on August 24, 1996 in 72 contiguous, 8.7 nm wide, spectral bands covering a wavelength range from 407 nm to 944 nm. Pixel size is 2.3 m in the across track direction and 4.3 m in the along track direction. Table 2 summarizes the *casi* sensor configuration parameters. Only wavelengths between 407 nm and 900 nm (68 bands) were used due to the poor spectral quality of the last four bands.

Table 2. *casi* sensor configuration.

Spectral coverage	407-944 nm
Number of bands	72
Spectral sampling interval	7.6 nm
Bandwidth at FWHM*	8.7 nm
Sensor altitude above ground	1905 m
Ground resolution: across track	2.3 m
along track	4.3 m
Swath	406 pixels

* FWHM: Full Width at Half Maximum

2.2 Image data preprocessing

The *casi* image data were roll corrected using the navigation data to remove most significant aircraft motion effects from the imagery. Surface reflectance was retrieved from the radiance data using a look-up table based approach implemented in the Imaging Spectrometer Data Analysis System (ISDAS) (Staenz et al., 1997 and 1998).

2.3 Band simulation

Band reduction. The number of bands were reduced by skipping every other band of the 68-band *casi* dataset resulting in a 34-band dataset. This procedure was repeated to produce datasets containing 17, 8, and 4 bands, respectively.

Varying bandwidth. In order to test the effect of varying the bandwidth on the unmixing results, 6 bands were chosen based on the geobotany dataset from Staenz (1996) (480 nm, 548 nm, 608 nm, 676 nm, 745 nm, 829 nm). A gaussian spectral response profile centered at each of the 6 selected bands was used to simulate the bandwidths ranging from 8.5 nm to 76.5 nm with an increment of 8.5 nm.

Sensor simulation. Quickbird spectral bands as shown in Table 1 were simulated using gaussian spectral response profiles.

2.4 Spectral unmixing

Constrained spectral unmixing was performed on all the simulated *casi* data cubes using an algorithm implemented in ISDAS (Szeredi et al., 1998 ; Boardman, 1989 and 1990). The method decomposes the image spectra $\vec{S}$ in terms of endmember spectra $\vec{S}_i$:

$$\vec{S} \approx \sum_{i=1}^{N} f_i \vec{S}_i \qquad \textbf{(1)}$$

where $0 \le f_i \le 1$, $\sum_{i=1}^{N} f_i = 1$ and f_i is the fraction of endmember *i* contributing to the image spectrum $\vec{S}$, and N is the total number of endmembers. The result of the unmixing is a set of N fraction images which show the fractional abundance of the endmembers. Endmember spectra were selected from the original image using the three first principal components (PCs) which account for 77%, 21% and 1% of the variability in the dataset, respectively. Endmembers are the purest pixel spectra in the dataset and are often located at the extremities of the scatterplot when two PCs are plotted against each other. Five endmember spectra were identified as shown in Figure 1: lime, green vegetation, oxidized tailings, water 1, and water 2 (distinct from water 1 because of it's high content of sewage, tailings, and lime). According to the PC scatterplots, the endmember spectra were the same for the band reduced, varying bandwidth, and sensor simulation data cubes. The unmixing results of the simulated datasets were then compared to the unmixing results of the full 68-band dataset. Comparison between the 68-band dataset unmixing results and the unmixing results from the simulated cubes was achieved by computing the absolute and relative difference.

3. RESULTS

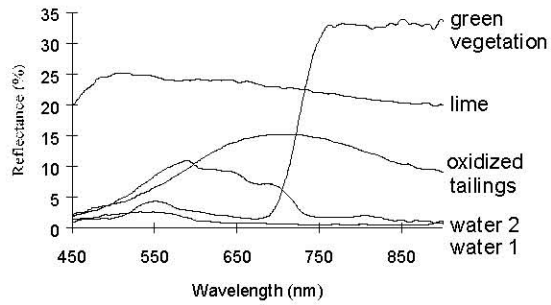

Figure 1. Endmember spectra.

The relative difference between the Quickbird simulation and the 68-band unmixing results is shown in Figure 2 for the green vegetation endmember. The plot shows that low fractions display a larger relative difference than higher fractions. For a constant absolute difference this result is to be expected.

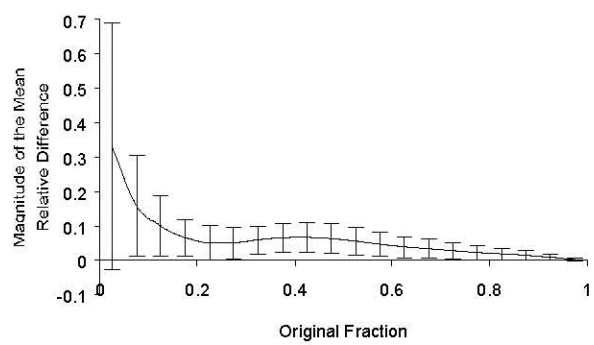

Figure 2. Relative difference (solid curve) and standard deviation (vertical bars) for the green vegetation endmember between unmixing results achieved with Quickbird simulated data and the 68-band *casi* data.

3.1 Band reduction

Figure 3 shows the effect of varying the number of *casi* bands on the spectral unmixing results. The absolute mean difference (AMD) remains under 0.02 for all the endmembers using 34, 17, and 8 bands. When using 4 bands the overall AMD increases but remains below 0.03 for green vegetation and lime. The two water endmembers consistently display a higher AMD than the other endmembers. This can be understood from eq. (1). The water endmember spectra $\vec{S}_{w1}$, $\vec{S}_{w2}$, are relatively dark, hence the spectral magnitudes $|\vec{S}_{w1}|$ and $|\vec{S}_{w2}|$ are small compared to the other endmembers. Due to this fact the fractions f_{w1} and f_{w2} can vary by a relatively large amount without changing the sum spectrum in eq.(1) too much. The constrained unmixing takes advantage of this fact and hence the fractions f_{w1} and f_{w2} vary more than the fractions of the other endmembers.

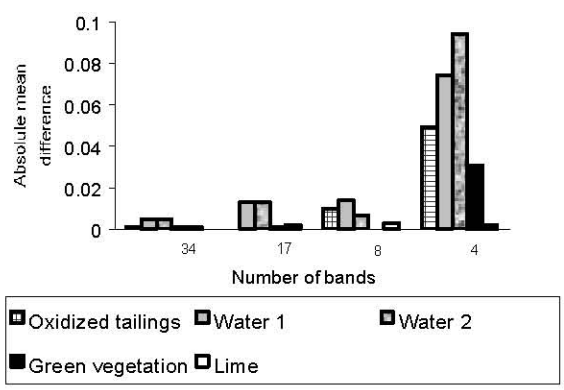

Figure 3. Absolute mean difference (AMD) between the 68-band unmixing results and unmixing results of a varying number of bands for each endmembers.

3.2 Varying bandwidth

Figure 4 shows the AMD and its standard deviation between the 68-band unmixing results and the varying bandwidth of the 6 selected band data cube. AMD slightly increases with increasing bandwidth but the AMD remains below 0.005. The standard deviation of the AMD decreases as the bandwidth increases since the local variations (in wavelength) in the spectrum are smoothed over. This results in less fractional variations and a smaller standard deviation.

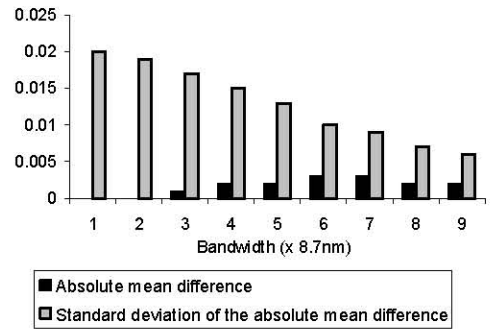

Figure 4. Absolute mean difference (AMD) and standard deviation between the 68-band umixing results and the unmixing results of varying bandwidth of the 6-band datacube.

3.3 Sensor simulation

In Figure 5 the AMD is shown for each endmember for the Quickbird simulation unmixing results against the 68-band unmixing results. Unlike for the case of four bands used in Figure 3, the four Quickbird bands were selected to enhance differences between the spectra and hence display lower AMD. As pointed out before, the two water endmembers, followed by the oxidized tailings, the green vegetation and the lime endmembers, show an inverse relationship between their spectral reflectance magnitude and their AMD. AMD values for all endmembers do not exceed 0.015. Similarly, the standard deviation of the AMD is related to the magnitude of the endmember spectra which indicates that more variation is expected when using low reflectance endmembers.

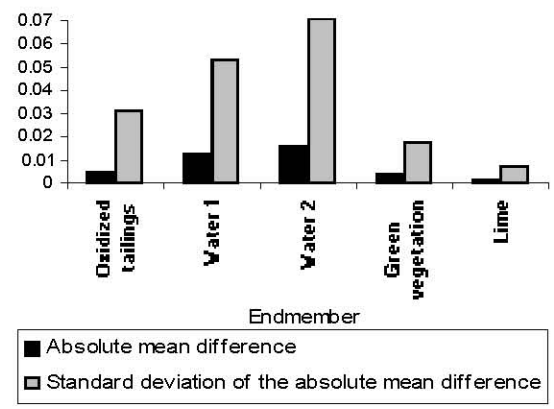

Figure 5. Absolute mean difference (AMD) between the 68-band unmixing results and the Quickbird simulation unmixing results for each endmember.

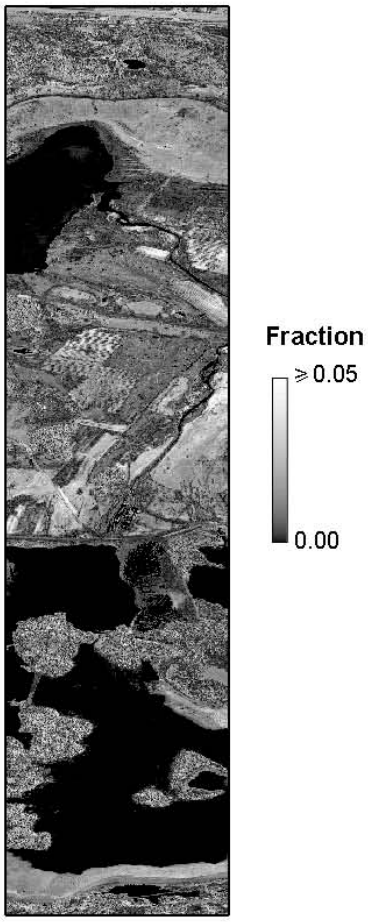

Figure 6. Map of the absolute difference (AD) between Quickbird simulation unmixing results and the 68-band unmixing results over the Copper Cliff mine tailings area in Sudbury.

The map shown in Figure 6 gives a spatial representation of the absolute difference (AD) between the Quickbird simulation unmixing results and the 68-band unmixing results over the Copper Cliff mine tailings area in Sudbury. The brighter parts of the map show higher differences and the darker parts show lower differences. Most of the data are in the AD range of 0.00 to 0.05.

4. CONCLUSION AND DISCUSSION

The unmixing results obtained by varying the number of bands produce absolute mean differences that do not exceed 0.02 for 34-band, 17-band and 8-band sets. The 4-band dataset yields larger differences, up to 0.094. However, Quickbird simulation indicates a difference of 0.016 is achievable if the bands are selected according to physical spectral properties. The bandwidth simulation results indicate that as bandwidth increases, the absolute mean difference increases and the standard deviation of the absolute mean difference decreases. The study shows that similar unmixing results are obtained using *casi* hyperspectral data and simulated broad-band high resolution multispectral sensors.

However, several points must be borne in mind: the limited spectral resolution of broad-band sensors make it difficult to spectrally identify endmembers and to spectrally separate subtle differences in endmembers. The endmembers in this study are very spectrally different and hence the second point was not a problem. To unmix a scene with N endmembers requires N-1 bands. Therefore, complicated scenes with many endmembers might require more bands to perform spectral unmixing than provided by forthcoming high spatial resolution sensors.

5. REFERENCES

Boardman, J.W., "Inversion of Imaging Spectrometry Data Using Singular Value Decomposition", *Proceedings of the 1989 International Geoscience and Remote Sensing Symposium (IGARSS '89) and the 12th Canadian Symposium on Remote Sensing*, Vancouver, BC, Vol. 4, pp. 2069-2072, 1989.

Boardman, J.W., "Inversion of High Spectral Resolution Data", *Proceedings of SPIE Conference on Imaging Spectrometry of the Terrestrial Environment*, Orlando, Florida, Vol. 1298, pp. 222-233, 1990.

Lévesque, J., Szeredi, T., Staenz, K., Singhroy, V., and Bolton, D., "Spectral Unmixing for Monitoring Mine Tailings Site Rehabilitation, Copper Cliff Mine, Sudbury, Ontario", *Proceedings of the Twelfth International Conference and Workshops on Applied Geological Remote Sensing*, Denver, Colorado, Vol. 1, pp.340-347, 17-19 November 1997.

Mend - Mine Environmental Neutral Drainage program: http://www.nrcan.gc.ca/mets/mend, 1998.

Inco Ltd : http://www.incoltd.com/invest/annrpt/96-env1g.htm, 1998.

Staenz, K., "Classification of a Hyperspectral Agricultural Data Set using Band Moments for Reduction of the Spectral Dimensionality", *Canadian Journal of Remote Sensing*, Vol. 22, No. 3, pp. 248-257, 1996.

Staenz, K., and Williams D., "Retrieval of Surface Reflectance From Hyperspectral Data Using a Look-Up Table Approach", *Canadian Journal of Remote Sensing*, Vol. 23, No. 4 , pp. 354-368, 1997.

Staenz, K., Neville, R.A., Lévesque, J., Szeredi, T., Singhroy, V., Borstad, G.A., and Hauff, P., "Evaluation of *casi* and SFSI Hyperspectral Data for Geological Applications - Two Case Studies", *in Geological Remote Sensing/ Case Studies* (editor V. Singhroy), Geological Association of Canada (GAC) Special Paper (in press), 1998.

Szeredi, T., Staenz, K., and Neville, R.A., "Spectral Unmixing in ISDAS", to be submitted to: *Canadian Journal of Remote Sensing*, 1998.

Preprint/Prétirage

PRELIMINARY RESULTS ON THE INVESTIGATION OF HYPERSPECTRAL REMOTE SENSING FOR THE IDENTIFICATION OF URANIUM MINE TAILINGS

Josée Lévesque*, Robert A. Neville, Karl Staenz

Canada Centre for Remote Sensing, Natural Resources Canada, 588 Booth St., Ottawa, Ontario, Canada, K1A 0Y7, Email: josee.levesque@ccrs.nrcan.gc.ca

and Q.S. (Bob) Truong
Canadian Nuclear Safety Commission, 280 Slater, Ottawa, Ontario, Canada, K1P 5S9

ABSTRACT

This paper investigates the potential of hyperspectral remote sensing for the identification of uranium mine tailings. The objective is to distinguish uranium mining operations from other types of mining to help in the development of nuclear safeguards. Probe-1 airborne hyperspectral data were acquired over the Pronto mine tailings near Elliot Lake, Ontario, Canada. Analysis of the data includes radiometric and atmospheric corrections, endmember extraction and identification, constrained linear spectral unmixing, and the production of an abundance map of each endmember. Reflectance spectra of laboratory standards of uranium compounds were measured to help in the identification of the endmember spectra. This paper presents the abundance maps of some of the endmembers and the spectra of the laboratory standards.

1. INTRODUCTION

This paper presents preliminary results on the investigation of the potential of hyperspectral remote sensing for the identification of uranium mine tailings. This study is part of the collaboration between the Canada Centre for Remote Sensing (CCRS) and the Canadian Safeguards Support Program (CSSP) of the Canadian Nuclear Safety Commission (CNSC). CNSC supports the International Atomic Energy Agency (IAEA) in developing operational remote sensing methodologies that will help to enforce international regulations for nuclear safeguards.

Mine wastes are difficult to hide, especially when mining low-grade ore as is often the case with uranium mining where the amount of waste is large compared to the amount of economic mineral extracted. As an example, the former mines at Elliot Lake were once considered economically viable with an average uranium concentration of 0.1%.

The radiological activity emanating from uranium mine tailings can be best assessed using airborne gamma ray spectrometry. However, it is not feasible to use these sensors on board a satellite platform due to the strong atmospheric absorption of the gamma radiation. This study attempts to identify spectrally, in the 400 nm - 2500 nm range, mineral compounds in the mine tailings that are associated with uranium

mining. The surface mineralogy of exposed uranium tailings can be determined using hyperspectral remote sensing which provides many contiguous narrow spectral bands that allows spectral discrimination and identification of various minerals. The objective is to investigate the potential of hyperspectral remote sensing for the identification of uranium mine tailings and distinguish them from other types of mine tailings. More specifically to determine if uranium mine tailings include spectrally distinct mineral compounds that could help distinguish them from mine tailings from other sources.

2. STUDY SITE DESCRIPTION

The Pronto uranium and copper mine tailings are located in the Elliot Lake area on the north shore of Lake Huron, Ontario, Canada (Figure 1). The tailings are the waste produced from mining uranium from a Precambrian quartz-conglomerate type deposit of detrital placer origin (Fogwill, 1981). Over 2 million tons of uranium ore were processed at the Pronto mill between 1955 and 1960 producing an equivalent amount of uranium tailings. The mill was then converted to process copper ore from a nearby mine and generated an additional 2 million tons of copper tailings until the closure of the mine in 1970. During the 1955 - 1970 period, tailings from uranium and copper ore extraction were deposited on a 47 ha area confined within a natural rock basin closed by waste rock dams (Rio Algom Limited, 1999).

FIGURE 1. Location of the Pronto mine.

Figure 2a shows the map of the Pronto waste management area. The arrows show the surface drainage that flows into the holding pond. A water treatment plant treats the incoming water with a mixture of lime and barium chloride to reduce the acidity and remove the radium. The treated water is then sent to a settling pond prior to being released into a stream that feeds Lake Huron. There is an area of exposed uranium tailings and an area of copper tailings. The copper tailings overlay the uranium tailings and helps to mitigate the radiation levels released by the tailings (Rio Algom Limited, 1999). The Pronto site contains one of the rare instances in the Elliot Lake area in which uranium tailings are exposed at the surface. Surprisingly, many of the uranium tailings are naturally revegetated, the remaining ones being submerged under water for remediation purposes. Figure 2b shows a Probe-1 RGB composite of the Pronto tailings management area. Some of the aforementioned features are identified in the image.

* Under contract to CCRS from MIR Télédétection inc., 110 rue de la Barre, Bur. 226, Longueuil, QC, J4K 1A3, Canada.

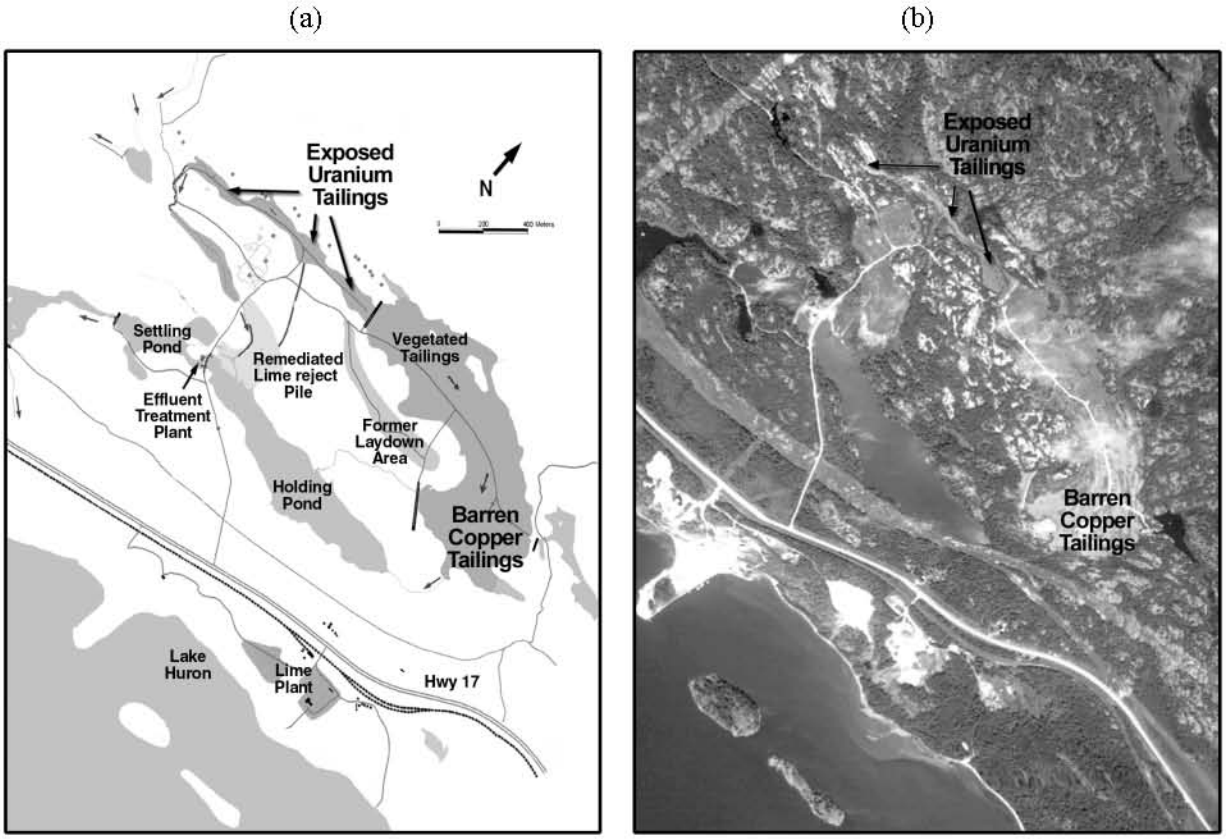

FIGURE 2. (a) Map of the Pronto waste management area and (b) black and white image of a Probe-1 colour composite (red: 662 nm, green:523 nm, blue:450 nm).

3. METHODOLOGY

All image processing and analyses were carried out using the Imaging Spectrometer Data Analysis System (ISDAS) developed at the Canada Centre for Remote Sensing (Staenz *et al.,* 1998).

3.1 AIRBORNE DATA ACQUISITION AND PROCESSING

Airborne hyperspectral Probe-1 data were acquired on July 8, 1999 over the Pronto mine. Table 1 shows the sensor configuration for the airborne survey. A total of 128 spectral bands were recorded between 440 nm and 2500 nm with a nominal bandwidth ranging from 11 nm to 22 nm. Probe-1 has a field-of-view of 60° and produces a 512-pixel wide image. It was flown at an altitude of 2139 m above ground level which produced a pixel size of 5 m by 5 m at nadir. No aircraft motion correction was required since the sensor was mounted on a three-axis gyro-stabilised platform which compensated for aircraft motion.

* Under contract to CCRS from MIR Télédétection inc., 110 rue de la Barre, Bur. 226, Longueuil, QC, J4K 1A3, Canada.

TABLE 1. Probe-1 sensor configuration.

Spectral coverage	440 nm - 2500 nm
Number of bands	128
Bandwidth at FWHM*	11 nm - 22 nm
Sensor altitude above ground	2650 m
Ground resolution:	
across track	5 m
along track	5 m
Field of view (FOV)	60°
Swath of image	512 pixels

** FWHM = Full Width at Half Maximum*

Calibration

Dark current was first subtracted from the Probe-1 data. Spectroradiometric laboratory measurements were used to transform the raw data from digital numbers (DN) to radiance using a vicarious calibration method (Secker *et al.*, 2001).

Atmospheric correction

An atmospheric correction was performed on the image data using a look-up table (LUT) approach to transform the radiance data into reflectance (Staenz and Williams, 1997). Table 2 shows the model input parameters used for the transformation. MODTRAN 3 radiative transfer code was used to calculate the atmospheric transmission over the full spectral range of the sensor.

TABLE 2. MODTRAN3 model input parameters for the atmospheric correction of the Probe-1 data.

Date	1999:07:08
GMT	14:07:30
Aircraft heading	134°
Sensor altitude *(above sea level)*	2.439 km
Terrain elevation *(above sea level)*	0.3 km
Solar zenith angle	47.6°
Solar azimuth angle	101.9°
Atmospheric model	midlatitude summer
Aerosol model	continental (rural)
Water vapour content	1.3 g/cm^2
Ozone column *(as per model)*	0.319 cm-atm
CO_2 mixing ratio *(as per model)*	357.5 ppm
Horizontal visibility	50 km

* Under contract to CCRS from MIR Télédétection inc., 110 rue de la Barre, Bur. 226, Longueuil, QC, J4K 1A3, Canada.

Spectral unmixing

Thirty endmembers were automatically extracted based on the iterative error analysis technique implemented in ISDAS (Szeredi *et al.*, 2001). The endmembers were used to unmix the Probe-1 data using a constrained linear technique (Shimabukuru and Smith, 1991; Boardman, 1995) which decomposes the image spectra in terms of linear combinations of the endmembers. In the constrained method, the image fractions are confined between 0 and 1 and sum to 1. The result of the unmixing procedure is a set of fraction images that show the fractional abundance of the endmembers.

3.2 LABORATORY REFLECTANCE MEASUREMENTS OF URANIUM STANDARDS

Spectral measurements were made of a number of compounds, minerals, and ore samples related to uranium mining and processing. A GER3700™ portable spectrometer was used to carry out the measurements in the laboratory. This spectrometer records wavelengths from 300 nm to 2500 nm with a 3 to 16 nm spectral resolution. A halogene lamp was used as the source of light. Reflectance was calculated using the ratio of the target (sample) radiance to the radiance of a reference (Spectralon™) target (x 100). Reflectance spectra were measured from laboratory standards samples of uranium ore, uranium-thorium ore, uranium tailings ore, yellowcake (U_3O_8).

4. PRELIMINARY RESULTS

4.1 ENDMEMBER FRACTION IMAGES

Figures 3a and 3b show the endmember fraction images of the uranium and copper tailings. High fractions are shown in white and zero fractions in black. Their associated endmember spectra are shown in Figure 3c and 3d. Both endmember spectra exhibit the shape of an iron oxide mineral with the strong iron absorption band in the 850 nm to 1000 nm range. This is no surprise since the uranium mined in the Elliot Lake area was extracted from a highly pyritic geological environment. Figure 4 shows the spectrum of such an iron oxide mineral (goethite) retrieved from the USGS (United States Geological Survey) spectral library together with the two tailings endmember spectra.

Figure 5 shows the endmember fraction map of water loaded with suspended sediments. The holding pond (untreated water), contains the highest fractions at the affluent of the two streams that drain the waste management area. High sediment load is shown in white and no sediment load in black. Prior to being released to the environment, the water is treated with lime to reduce acidity and barium chloride to remove radium, then sent to the settling pond where the chemical reactions occur which help to settle the sediments to the bottom of the pond. The water exiting the settling pond is free of suspended sediments (dark = low fractions) which indicates the success of the water treatment.

* Under contract to CCRS from MIR Télédétection inc., 110 rue de la Barre, Bur. 226, Longueuil, QC, J4K 1A3, Canada.

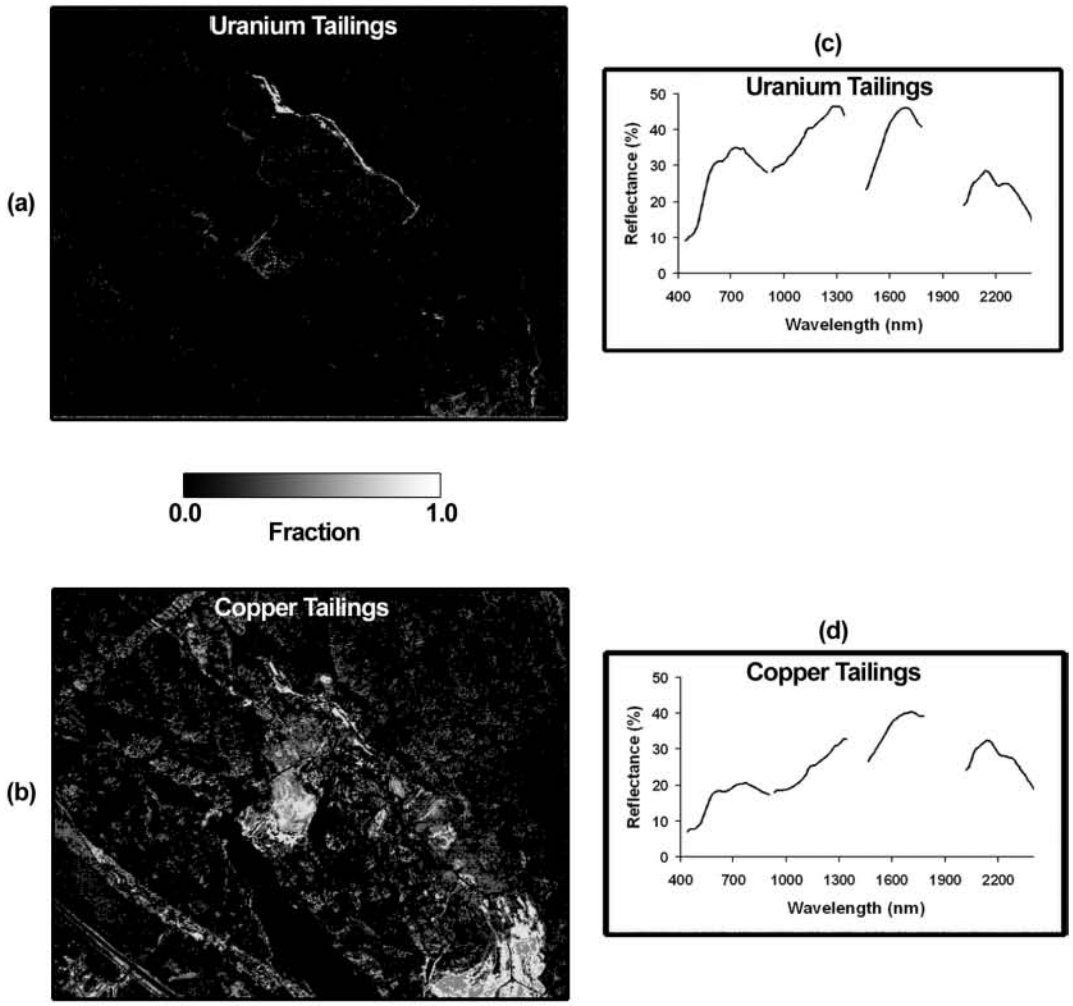

FIGURE 3. Endmember fraction maps corresponding to the (a) uranium tailings and (b) the copper tailings and their associated endmember spectra (c) and (d).

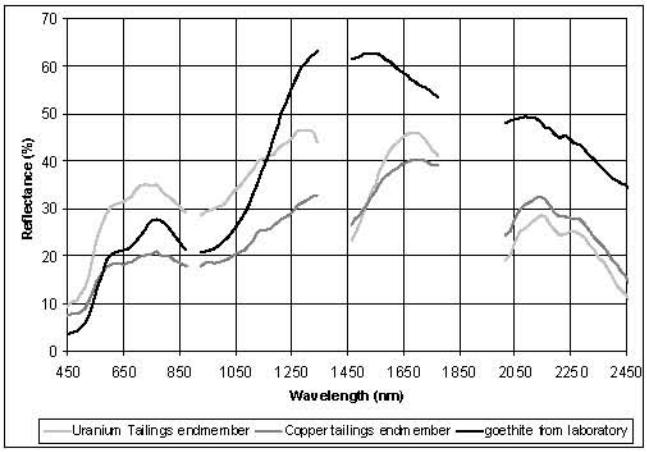

FIGURE 4. Uranium and copper tailings endmember spectra superimposed on a laboratory spectrum of goethite from the USGS spectral library.

* Under contract to CCRS from MIR Télédétection inc., 110 rue de la Barre, Bur. 226, Longueuil, QC, J4K 1A3, Canada.

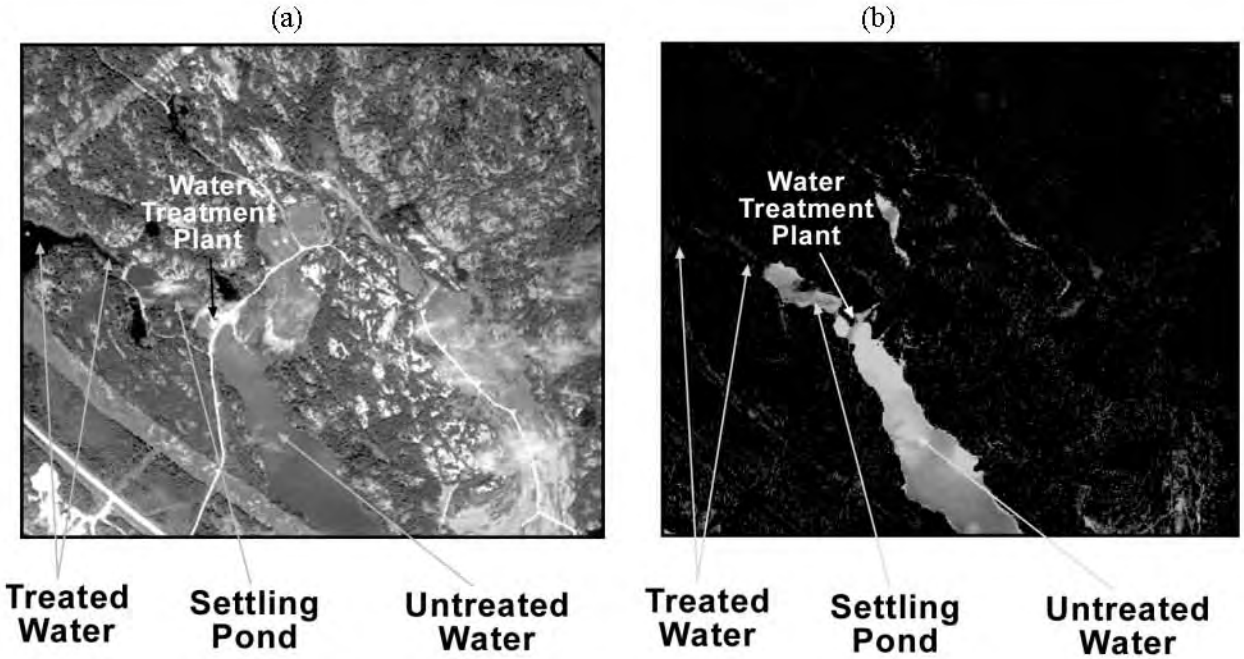

FIGURE 5. (a) Black and white RGB colour composite and (b) the endmember fraction image corresponding to sediment loaded water.

4.2 LABORATORY MEASUREMENTS

Laboratory reflectance spectra of the uranium compounds are shown in Figure 6. Indicated in this Figure are the locations of the absorption features of a single crystal of uranium dioxide (UO_2) (Bates, 1965). Possible important absorption features in the laboratory spectra are located at 837 nm, 865 nm, 1115 nm, 1620 nm, 1730 nm and 2260 nm. A wide UO_2 absorption band ranging from 1350 nm to 1540 nm is also present in the laboratory spectra. The 1730 nm feature was found to be related to the absorption from the plastic dish used to hold the samples while measuring their reflectance. The sources of the other absorption features have not yet been determined. Yellowcake has a distinctly high reflectance in the yellow and red wavelengths. However, not all U_3O_8 concentrates are yellow in colour so that a more distinctive spectral feature must be determine to spectrally identify this uranium compound. None of the single crystal UO_2 absorption features could be identified in the uranium and copper mine tailings spectra from the image endmember. This is not surprising because the concentration of uranium in these tailings is extremely low (average 0.1%).

* Under contract to CCRS from MIR Télédétection inc., 110 rue de la Barre, Bur. 226, Longueuil, QC, J4K 1A3, Canada.

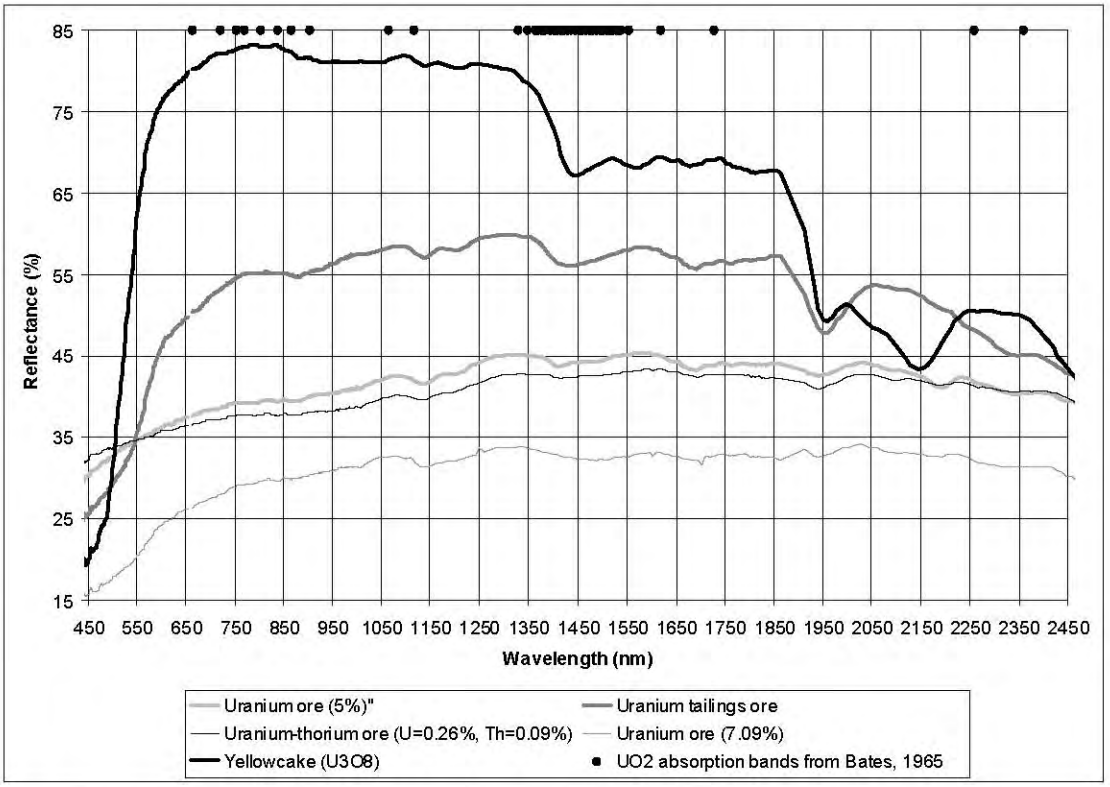

FIGURE 6. Laboratory spectra of uranium compounds and the absorption bands of a UO_2 crystal from Bates (1965).

5. DISCUSSION AND CONCLUSION

These results should be interpreted with care since no spectral absorption feature has yet been associated with uranium mine tailings. The two endmembers (uranium tailings and copper tailings) are more likely to be related to different iron oxide content than to the presence of uranium compounds. The UO_2 reflectance spectrum used to determine the spectral absorption features of uranium may not represent the absorption features of other uranium compounds and by-products. In addition, the task of identifying a measurable spectral feature is made more difficult by the lack of high quality reflectance data in the open literature for uranium bearing minerals. Moreover, the low grade of mined uranium (0.1%) in the Elliot Lake area suggests that the tailings content of related minerals is well below this value (e.g. thorium = 0.03%). For this reason, this study was extended to the Key Lake mine site in Saskatchewan (Canada) where high-grade uranium ore from McArthur River mine is processed (21% average ore grade). The tailings at the Key Lake mine have an average uranium content of 0.3% which is higher than the ore that was mined in the Elliot Lake area. This concentration may still be too low to detect uranium by-products using laboratory spectral measurements and airborne optical hyperspectral remote sensing. However, because they are still in operation, the hyperspectral data acquired over the Key Lake mining facilities will allow the spectral investigation of other types of ground features related to uranium mining such as the ore storage and mixing facilities, the milling facilities, and the yellowcake storage area. This is being investigated using SFSI-2 hyperspectral imagery which operates in the wavelength range of 1220 to 2420 nm (Neville *et al.*, 2001).

* Under contract to CCRS from MIR Télédétection inc., 110 rue de la Barre, Bur. 226, Longueuil, QC, J4K 1A3, Canada.

6. REFERENCES

Bates, J.L. (1965). Visible and infrared absorption spectra of uranium dioxide. *Nuclear Science and Engineering*, 21:26-29.

Boardman, J.W. (1995). Analysis, understanding and visualization of hyperspectral data as convex sets in n-space. *Proceedings of the International SPIE Symposium on Imaging Spectrometry*, SPIE Vol. 2480, Orlando, Florida, U.S.A., pp. 23-36.

Fogwill, W.D. (1981). Canadian and Saskatchewan uranium deposits: compilation, metallogeny, models, exploration. *Geology of uranium deposits. Proc. of the CIM-SEG Uranium Symposium, September 1981.* The Canadian Institute of Mining and Metallurgy, Special Volume 32, pp. 3-19.

Neville, R.A., Staenz, K., Lévesque, J., Nadeau, C., Truong, Q.S., Borstad, G.A. (2001) Hyperspectral analysis of imagery of a uranium mine site. Proc. of the ISSSR Symposium, Québec City, June 11-14.

Rio Algom Limited (1999), Elliot Lake Mine Tailings Management. Internal Report.

Secker, J., Staenz, K., Gauthier, R.P., and Budkewitsch, P. (2001). Vicarious calibration of hyperspectral sensors in operational environments. *Remote Sensing of Environment*, 76:81-92.

Shimabukuru, Y.E., and Smith, J.A. (1991). The least squares mixing models to generate fraction images derived from remote sensing on multispectral Data. *IEEE Transactions on Geoscience and Remote Sensing*, 29:16-20.

Staenz, K., and Williams, D.J. (1997). Retrieval of surface reflectance from hyperspectral data using a look-up table approach. *Canadian Journal of Remote Sensing*, 23(4):354-368.

Staenz, K., Szeredi, T., and Schwarz, J. (1998). ISDAS - A system for processing/analyzing hyperspectral data. *Canadian Journal of Remote Sensing*, 24(2):99-113.

Szeredi, T., Staenz, K., Neville, R. A. (2001), Automatic endmember selection: part 1 theory. *Remote Sensing of Environment* (submitted).

* Under contract to CCRS from MIR Télédétection inc., 110 rue de la Barre, Bur. 226, Longueuil, QC, J4K 1A3, Canada.

PREPRINT/PRÉTIRAGE

The Impact of Spectral Band Characteristics on Unmixing of Hyperspectral Data for Monitoring Mine Tailings Site Rehabilitation

J. Lévesque[1)], K. Staenz[2)], and T. Szeredi[3)]

[1)]MIR Télédétection Inc., 2182 de la Province, Longueuil, QC, J4G 1R7, Canada
Email : josee.levesque@ccrs.nrcan.gc.ca

[2)]Canada Centre for Remote Sensing, 588 Booth St., Ottawa, ON, K1A 0Y7, Canada

[3)] MacDonald Dettwiler and Assoc., 13800 Commerce Parkway, Richmond, BC, V6V 2J3, Canada

SUMMARY

This paper demonstrates the impact of band characteristics on spectral unmixing of Compact Airborne Spectrographic Imager (*casi)* reflectance data acquired in the visible near-infrared spectral range over the Copper Cliff mine tailings site near Sudbury (Ontario, Canada). Spectral unmixing is used to monitor the rehabilitation status. For this purpose, the bands were reduced systematically from 65 to 33, 17, 8 and 4 bands using the original *casi* bandwidth of 8.7 nm full width at half maximum (FWHM). An interpolated data set using a cubic spline was derived from the 65-band *casi* spectra to study the effect of the bandwidth. The bandwidth at FWHM was varied between 8.5 nm and 76.5 nm in increments of 8.5 nm for six selected band positions across the *casi* wavelength range. High spatial resolution Ikonos 2 multispectral sensor image data with less bands and larger bandwidths than *casi* were simulated in order to investigate the combined effect of number of bands and bandwidth. These data cubes were unmixed with a constrained linear approach involving the endmembers green vegetation, lime, oxidized tailings, and two different water types. A comparison of the unmixing results indicates a mean absolute difference of up to 0.02 (standard deviation: $\pm$ 0.05) between the endmember fractions of the simulated data versus the 65-band benchmark data if the bands are selected according to physical spectral properties. The errors are much larger if the bands are not positioned properly. In general, the unmixing of the simulated data, including the four broad-band Ikonos simulation case, produced similar results as with

the full 65-band *casi* as long as the bands are positioned with respect to physical spectral properties. Such a result, especially for the broad-band simulations, was achieved mainly because the endmembers are spectrally very distinct and do not show subtle differences.

RÉSUMÉ

Cette étude démontre l'importance de la position, du nombre, et de la largeur des bandes spectrales sur les résultats de déconvolution spectrale des données de réflectance du Compact Airborne Spectrographic Imager (*casi*). Les données ont été acquises dans le visible et le proche infrarouge pour le site de rejets miniers de la mine Copper Cliff près de Sudbury (Ontario, Canada). Afin d'étudier l'effet du nombre de bandes spectrales, les données *casi* ont été réduites de façon systématique de 65 à 33, 17, 8 et 4 bandes en maintenant la largeur de bande initiale de 8,7 nm à mi-hauteur. Pour étudier l'effet de la largeur des bandes, une série de données interpolées par une fonction cubique a été créée à partir des spectres des données originales *casi* de 65 bandes. Une image de six bandes spectrales pré-sélectionnées a été produite pour chaque largeur de bande à mi-hauteur variant entre 8,5 nm et 76,5 nm avec un intervalle de 8,5 nm. Les données multispectrales à haute résolution spatiale Ikonos 2 (comportant des fenêtres spectrales plus larges et moins nombreuses que *casi*) ont été simulées afin d'étudier l'effet combiné du nombre et de la largeur de bande. Une déconvolution spectrale linéaire a été appliquée sur les données à partir de la signature spectrale de 5 composantes élémentaires : végétation, chaux, rejets miniers oxydés, et deux types de surfaces d'eau. Les résultats montrent une différence absolue moyenne allant jusqu'à 0,02 (écart-type: ± 0,05) entre les fractions des composantes élémentaires des données simulées et celles provenant de la série de données originales *casi* de 65 bandes lorsque que les bandes spectrales sont sélectionnées selon des propriétés physiques et spectrales. La différence absolue moyenne est beaucoup plus élevée lorsque les bandes sont positionnées de façon aléatoire. En général, la déconvolution spectrale des données simulées produit des résultats semblables à ceux obtenus avec la série de données originale *casi* de 65 bandes dans la mesure où la position des bandes spectrales est déterminée d'après des propriétés physiques et spectrales. De tels résultats, entre autre ceux de la simulation de bandes larges, sont

réalisables en grande partie parce que les composantes élémentaires ont des signatures spectrales très distinctes.

1. INTRODUCTION

Canadian liability for acid mine drainage is in the order of $2 billion to $5 billion depending on the technique used to dispose of and treat the acidic waste (Feasby and Jones, 1994). In the Sudbury area alone, Inco Ltd. spends an annual $5 million to reclaim property (Inco, 1998). Given these enormous costs, monitoring techniques are needed to evaluate their efficiency for reclamation of mine tailings sites, e.g., revegetation (Hossner, 1988). Recent work indicated that remote sensing, especially imaging spectrometry, has the potential to play a significant role in this area (Ferrier, 1999; Shang et al., 1999 ; Mueller et al., 1997; Farrand and Harsanyi, 1997 ; Swayze et al., 1996; Singhroy, 1996). In previous studies, Lévesque et al. (1997 and 1999) demonstrated the vegetation monitoring capability of the Compact Airborne Spectrographic Imager (*casi*) over the Copper Cliff mine tailings area near Sudbury, Ontario, Canada. If long term monitoring is required airborne surveys can become quite expensive. The question is whether one can achieve similar results using Ikonos 2 and other forthcoming high spatial resolution satellites such as Orbview3 and Quickbird (ASPRS, 1996 ; Space Imaging, 1999). Table 1 summarizes the basic instument charactersitics of these sensors. The spatial resolution of these sensors is similar to that of the *casi* data acquired over the Copper Cliff mine tailings site (2.5 m by 4.3 m). However, these sensors have fewer spectral bands and their bands are wider than those of the *casi* visible-near infra-red (VNIR) hyperspectral data sets used for this study.

This paper investigates the effect of varying bandwidth and number of bands on the ability to monitor mine tailings revegetation over a site near Sudbury using a spectral unmixing approach. In addition, the four Ikonos 2 bands and related bandwidths were simulated in order to evaluate their potential monitoring capability. Since Orbview3 and Quickbird have basically the same spectral configuration as Ikonos 2 the results obtained for Ikonos 2 are assumed to be applicable to these sensors also. The *casi* data set used for

the study presented in this paper was collected in 72 bands in 1996. The data analysis was carried out on the Imaging Spectrometer Data Analysis System (ISDAS) of the Canada Centre for Remote Sensing (Staenz et al., 1998).

2. IMAGE DATA USED

The image data was collected with a *casi* instrument in spectral mode on August 24, 1996 over the Copper Cliff mine tailings site near Sudbury, Ontario, Canada. The data set includes 72 contiguous, 8.7 nm wide, spectral bands covering a wavelength range in the VNIR from 407 nm to 944 nm (Anger et al., 1996). The instrument was flown at an altitude of 1905 m resulting in a pixel size of 2.5 m in the across track direction and 4.3 m in the along track direction. Table 2 summarizes the *casi* sensor configuration parameters. Only wavelengths between 429 nm and 913 nm (65 bands) were used from the *casi* data set because of the poor data quality of the first three bands as well as the last four bands. This is mainly due to the drop-off of the responsivity of the silicon detector at both ends of the *casi* wavelength range.

3. ANALYSIS APPROACH

Analysis of the *casi* data included removal of the most significant aircraft motion effect, surface reflectance retrieval, band simulation analysis, constrained linear spectral unmixing, and comparison of the resulting fraction images achieved with the various simulated data sets versus the one retrieved from the full *casi* data set. The data processing scheme is outlined in Figure 1.

3. 1 Pre-Processing

In order to correct for the most significant aircraft motion effect, the aircraft roll was calculated using the navigation data to calculate lateral pixel shifts for each line. These shifts were then applied to the entire image cubes on a line-by-line basis.

In the next pre-processing stage, surface reflectances were computed from calibrated (at-sensor radiance) data. The procedure applied to the data uses a five dimensional look-up table (LUT) approach with tunable breakpoints to provide additive and multiplicative coefficients for removal of scattering and absorption effects (Staenz and Williams, 1997). The LUT variables are: wavelength, pixel position, atmospheric water vapour, aerosol optical depth, and terrain elevation. This procedure has the advantage of reducing significantly the number of radiative transfer (RT) code runs thereby saving the time that would be required to run such a code on a pixel-by-pixel basis.

For the LUT generation for the different data sets, the MODTRAN3 radiative transfer code was run for the input parameters as listed in Table 3 for a low-level (5 %) and high-level flat reflectance spectrum (60%). This produces a LUT for each reflectance level. These LUTs were produced for five pixel locations equally spaced across the swath, including nadir and swath edges, and for single values of aerosol optical depth (horizontal visibility), terrain elevation, and water vapour contents. The final step involved in the LUT generation is the convolution of the model output radiances with the relative spectral response profiles of the sensor. *casi*'s response profiles were approximated by a trapezoidal-shaped line spread function.

For the retrieval of the surface reflectance, the LUTs were adjusted only for the pixel position using a bi-linear interpolation routine (Press et al., 1992) since single values for the other LUT parameters were used for the entire cube. The water vapour content was determined by applying the atmospheric correction process iteratively to sample scene spectra, while adjusting this atmospheric parameter, and selecting the value which best removed the water vapour absorption features on average. The surface reflectance of each pixel could then be computed as described in Staenz and Williams (1997). Sample reflectance spectra are displayed in Figure 2.

An assessment of the retrieved spectra revealed only minor irregularities in the reflectance data that may have originated in the sensor, or that may have resulted from

the approximations made in the atmospheric modelling and the selection of parameters. These minor band-to-band errors were not corrected.

3.2 Band Simulations

The number of bands was reduced by skipping every other band of the 65-band data cube resulting in a 33-band data set. This procedure was repeated to produce data sets containing 17, 8, and 4 bands, respectively. This systematic way to pick the bands, especially concerning the data sets with 8 and 4 bands (Table 4), is not ideal from a physical point-of-view. The bands are not properly positioned for the application focused on in this study. In order to overcome these difficulties, six *casi* bands were selected based on the spectral characteristics of vegetation for inclusion in the analysis (Staenz, 1996). This data is referred to in the paper as the geobotany data set. Band positions of this data set are listed in Table 4.

In order to test the effect of varying the bandwidth on the unmixing results, the original *casi* data were fit with a cubic spline and interpolated to a specific wavelength grid (Press et al., 1992). The grid size is determined by dividing the spectral response profile of the bands to be simulated into 20 intervals. This approach is appropriate since subtle spectral changes do not occur for the target type considered in this study. The interpolated data is assumed to be the underlying data set for the subsequent simulations. The interpolated values were then convolved to Gaussian spectral response profiles with full width at half maximum (FWHM) bandwidths, ranging from 8.5 nm to 76.5 nm in increments of 8.5 nm. The profiles were centred at the six band positions of the geobotany data set as listed in Table 4.

In order to consider a more realistic case with a few well selected broad bands, the spectral band characteristics of the four-band instrument onboard Ikonos 2 were simulated with the same technique as described in the previous paragraph from the *casi* 65-band data sets using Gaussian spectral response profiles. The centre wavelengths and

associated bandwidths are summarized in Table 4. The fourth band centred at 830 nm with a bandwidth of 140 nm FWHM could not be simulated properly with *casi* since the 65-band data set with an upper wavelength limit of 913 nm does not entirely cover the right tail of the response profile. Therefore, a narrower bandwidth of 83 nm FWHM was used to approximate the fourth Ikonos band. To ensure that our results are compatible with real Ikonos 2 data, the off nadir viewing direction should be limited to less that 15° (*casi* data set = ± 18°) when acquiring the data.

3.3 Spectral Unmixing

Constrained linear spectral unmixing was performed on all the simulated *casi* data cubes using an algorithm implemented in ISDAS (Szeredi et al., 1999 ; Boardman, 1989 and 1990). The method decomposes the image spectra $\bar{S}$ in terms of endmember spectra $\bar{S}_i$:

$$\bar{S} = \left(\sum_{i=1}^{N} f_i \bar{S}_i \right) + \vec{r}, \qquad (1)$$

where $0 \le f_i \le 1$, $\sum_{i=1}^{N} f_i = 1$ and f_i is the fraction of endmember *i* contributing to the image spectrum $\bar{S}$, N is the total number of endmembers, and $\vec{r}$ is the error term. The result of the unmixing procedure is a set of N fraction images that show the fractional abundance of the endmembers. Endmember spectra were selected from the 65-band image cube using the first three principal components (PCs) which account for 77%, 21% and 1% of the variability, respectively. Endmembers are the purest pixel spectra in the data set and are often located at the extremities of the scatter plot which results when the spectral data are plotted in PC space. Five endmembers were selected from the 65-band data as shown in Figure 3. These endmembers were identified as lime, green vegetation, oxidized tailings, water 1, and water 2 using field reference information in combination with ground-based spectral measurements collected with a GER3700 field spectroradiometer.

Water 2 is distinct from water 1 because of it's high content of sewage, tailings, and lime. The spectra of these endmembers are displayed in Figure 4. According to the PC scatter plots, the same five endmembers were identified for the different simulated data cubes. The endmembers for the different simulations were then generated from the endmembers of the 65-band data the same way as the simulated data sets discussed in the previous section.

3.4 Assessment of Results

The fraction images retrieved with the spectral unmixing procedure from the simulated data sets were then compared to those extracted from the 65-band data. The absolute values of the differences between the fractions found using the 65-band data and that found using the sub sampled multispectral data sets, were computed on a pixel-by-pixel basis for each endmember. Subsequently, the mean and standard deviation of these absolute differences were calculated.

4. RESULTS

As an example of the output of the constrained unmixing, the fraction images of vegetation, lime, and oxidized tailings retrieved from the 65-band data cube are shown in Figure 5 together with a colour composite providing an overview of the study site. The upper part of Figure 5a is the inactive tailings where most of the revegetation work is being done. Some of the typical areas of the tailings are identified in the colour composite and depicted in the adjacent photographs. The three endmembers shown are those most important for tailings rehabilitation purposes. The fractions vary between 0 and 1 with blue representing a low value and red a high value. The lower part of Figure 5a is an active tailings area where fresh tailings are being deposited.

An examination of the error images associated with spectral unmixing (Eq.1) of the 65-band data revealed no significant errors and hence, one can be confident all major endmembers have been found and the endmembers span the data space. In addition, the unmixing results have been validated in the field as reported by Staenz et al. (1999). Therefore, the fraction images derived from this data cube represent an ideal reference for this study.

4.1 Band Reduction

Figure 6 shows the effect of decreasing the number of *casi* bands on the spectral unmixing results. The mean absolute differences remain under 0.02 (standard deviation: ± 0.03) for all the endmembers using 33, 17, and 8 bands. When considering four bands the overall mean absolute difference increases but remains below 0.04 (± 0.05) for green vegetation and lime and below 0.05 (± 0.06) for oxidized tailings, respectively. These errors decrease to the same level as for the 33, 17, and 8 band cases when the bands are selected according to physical spectral properties as is the case for the 6-band geobotany data set. The two water endmembers consistently display a higher mean absolute difference than the other endmembers. This can be understood from Eq. 1. The water endmember spectra, $\bar{S}_{w1}$ and $\bar{S}_{w2}$, are relatively dark, hence the spectral magnitudes $|\bar{S}_{w1}|$ and $|\bar{S}_{w2}|$ are small compared to the other endmembers. Due to this fact the fractions f_{w1} and f_{w2} can vary by a relatively large amount without changing significantly the sum spectrum in Eq. 1. The constrained unmixing takes advantage of this fact and hence the fractions f_{w1} and f_{w2} vary more than the fractions of the other endmembers.

4.2 Varying Bandwidth

The comparison between the fractions retrieved from the 65-band data and the data sets of different bandwidth simulated from the geobotany image cube revealed mean absolute differences below 0.008 ($\pm$ 0.021) for the vegetation, lime, and oxidized tailings endmembers. The maximum mean absolute difference values occured at the 8.5 nm bandwidth. A similar trend was found for the endmembers water 1 and water 2 but with a higher mean absolute difference of up to 0.021 ($\pm$ 0.051). The standard deviation of the absolute difference decreases for all endmembers as the bandwidth increases since the local variations (in wavelength) in the spectrum are smoothed over. This results in less fractional variations and a smaller standard deviation. As an example, Figure 7 shows the mean and standard deviation of the absolute difference for the green vegetation and water 1 endmembers.

4.3 Ikonos Simulation

In Figure 8 the mean absolute difference is shown for each endmember for the Ikonos 2 simulation unmixing results against the 65-band unmixing results. Unlike for the four-band case used in Figure 6, the four Ikonos 2 bands display lower mean absolute differences. This was expected since the four Ikonos bands are better positioned to enhance differences between spectra. The mean absolute difference for all endmembers do not exceed 0.014 ($\pm$ 0.07). As pointed out before, the two water endmembers, followed by the oxidized tailings, the green vegetation and the lime endmembers, show an inverse relationship between their spectral reflectance magnitude and their mean absolute difference. Similarly, the standard deviation of the mean absolute difference is related to the magnitude of the endmember spectra which indicates that more variation is expected when using low reflectance endmembers such as water 1 and water 2.

As an example, the spatial representation of the Ikonos simulation analysis is presented in Figure 9 for the green vegetation endmember. Figures 9a and b depict the fractions retrieved from the 65-band and the simulated Ikonos data , respectively. The absolute difference map of these fraction images is shown in Figure 9c. The bluish portion of the difference map indicates lower differences while the red parts show higher differences. 98.8 % of the data are in the absolute difference range of 0.00 to 0.05.

5. DISCUSSION

Although the results indicate generally a reasonable agreement between the endmember fraction images retrieved from the simulated data sets versus the 65-band data, several points have to be considered.

The separation and identification of endmembers becomes more difficult if one moves from hyperspectral data towards multispectral broad-band data. The limited spectral resolution combined with a limited number of bands makes it difficult to separate spectrally subtle differences in endmember spectra and, subsequently, can be expected to lead generally to poor unmixing results. However, since the endmembers in this study are spectrally very different, the unmixing of the simulated broad-band Ikonos 2 data produced fractions similar to those resulting from unmixing of the *casi* 65-band data. This result is consistent with the results of the bandwidth simulation analysis using well-defined band positions for the application under consideration. However, the unmixing results are strongly affected if the bands are not positioned properly for a given application as shown in Figure 6 with the band reduction analysis.

The endmembers for a specific simulated data set were computed the same way as the image data set itself, e.g., for the Ikonos simulation the endmember spectra of the 65-band data were convolved to the Ikonos four-band characteristics. In order to evaluate the impact of this approach on the fraction images, the endmembers were also extracted from the simulated data sets themselves. The latter procedure is usually the preferred approach since scaling issues between image data and endmembers of ground (library) spectra can be avoided. However, if spectra from a library are used as endmembers, then the band characteristics of the sensor under consideration have to be simulated from those spectra. No significant differences were found between fractions retrieved with endmembers selected from the simulated data sets directly and via the 65-band data.

The unmixing procedure requires N–1 bands to unmix N endmembers. With five endmembers retrieved from the data sets under consideration, the number of bands was limited to four in this study. Complicated scenes containing more endmembers might need more bands to perform unmixing than provided by the forthcoming high spatial resolution sensors such as onboard Ikonos 2. Accordingly, the unmixing procedure cannot be applied in such cases using this type of sensor. Other methods such as traditional classification approaches (e.g. maximum likelihood) could be used, but they are not able to provide the same detailed target information as spectral unmixing.

6. CONCLUSIONS

The influence of spectral band characteristics (number of bands, bandwidth) on spectral unmixing have been investigated for monitoring the rehabilitation status of mine tailings. For this purpose, different band sets, including the four-band multispectral sensor onboard Ikonos 2, have been simulated from hyperspectral VNIR 65-band *casi* surface reflectance data. The resulting endmember fractions for green vegetation, lime, oxidized tailings, water 1, and water 2, retrieved from the simulated data sets, have been compared against those obtained from the 65-band data.

The unmixing results obtained for the different endmembers by decreasing the number of bands produces mean absolute differences that do not exceed 0.02 (standard deviation: ± 0.03) for 33-band, 17-band and 8-band data sets. The 4-band data set yields larger differences, up to 0.14 (± 0.22). However, Ikonos 2 simulation indicates that a mean absolute difference of 0.014 is achievable if the bands are selected according to physical spectral properties. The largest mean absolute differences between the fraction images occur for water 1 and water 2. This is also true for the bandwidth simulation study. It revealed mean absolute differences of a magnitude similar to those resulting from the band reduction study with the exception of the 4-band simulation. In this case, the mean absolute difference is significantly lower for the bandwidth cases, about 7 to 10 times depending on the endmember. Furthermore, the bandwidth simulation results indicate that as bandwidth increases, the standard deviation of the mean absolute difference decreases.

The study shows that especially for the non-water endmembers, which are most important for revegetation monitoring, similar unmixing results were obtained using the simulated data as retrieved with *casi* hyperspectral data as long as the bands are positioned according to physical spectral properties. This is even true for the four broad-band Ikonos 2 simulation. However, for sensors with similar band characteristics as Ikonos 2, the results cannot be readily transferred to more complicated scenes and hence, containing more endmembers than the scene used in this study. This is due to the required minimum number of bands, N-1, for unmixing N endmembers. It is also more difficult to identify endmembers, especially when subtle differences occur, if only a few spectral bands are available. Nevertheless, the study demonstrated that high spatial broad-band sensors such as Ikonos 2 and Quickbird have the potential for monitoring mine tailings rehabilitation using spectral unmixing.

7. ACKNOWLEDGEMENTS

The authors thank The Centre for Research in Earth and Space Technology (CRESTech) for the acquisition of the *casi* data and related technical support. The support of the 1996 field campaign by R. McGregor (Atomic Energy of Canada Ltd.) and A. Dumouchel (Canada Centre for Remote Sensing) and the technical assistance of J. Lefebvre (MacDonald Dettwiler and Associated) is gratefully acknowledged. Our thanks to P. Yearwood of Inco Limited for providing access to the mine tailings site and for logistical support.

8. REFERENCES

Anger, C.D., S. Achal, T. Ivanco, S. Mah, R. Price, and J. Busler, 1996, "Extended Operational Capabilities of *casi*", Proceedings of the 2nd International Airborne Remote Sensing Conference, San Francisco, California, pp.124-133.

ASPRS, 1996, "Land Satellite Information in the Next Decade – The World Under a Microscope", Executive Summary, American Society for Photogrammetry and Remote Sensing, Bethesda, Maryland, U.S.A., 72 pages.

Boardman, J.W., 1989, "Inversion of Imaging Spectrometry Data Using Singular Value Decomposition", Proceedings of the 1989 International Geoscience and Remote Sensing Symposium (IGARSS '89) and the 12th Canadian Symposium on Remote Sensing, Vancouver, British Columbia, Canada, Vol. 4, pp. 2069-2072.

Boardman, J.W., 1990, "Inversion of High Spectral Resolution Data", Proceedings of SPIE Conference on Imaging Spectrometry of the Terrestrial Environment, Orlando, Florida, U.S.A., Vol. 1298, pp. 222-233.

Boardman, J.W., and J.F. Huntington, 1996, "Mineral Mapping with 1995 AVIRIS Data", Summaries of the Sixth Annual JPL Airborne Earth Science Workshop, JPL Publication 96-4, Vol. 1, Pasadena, California, U.S.A., pp. 9-11.

Farrand, W.H., and C. Harsanyi, 1997, "Mapping of Mine Tailings in the Coeur d'Alene River Valley, Idaho, Through the Use of Constrained Energy Minimization Technique", Remote Sensing of Environment, Vol. 59, pp. 64-76.

Feasby, G., and R.K. Jones, 1994, "Report of Results of a Workshop on Mine Reclamation", Canada Centre for Mineral and Energy Technology, 18 pages.

Ferrier, G., 1999, "Application of Imaging Spectrometer Data in Identifying Environmental Pollution Caused by Mining at Rodaquilar, Spain", Remote Sensing of Environment, 68:125-137.

Hossner, L.R., 1988, "Reclamation of Surface-Mined Lands", CRC Press Inc., Boca Raton, Florida, U.S.A., Vol. 1, 189 pages.

Lévesque, J., Szeredi, T., Staenz, K., Singhroy, V., and Bolton, D., 1997, "Spectral Unmixing for Monitoring Mine Tailings Site Rehabilitation, Copper Cliff Mine, Sudbury, Ontario", Proceedings of the Twelfth International Conference and Workshops on Applied Geological Remote Sensing, Denver, Colorado, U.S.A., Vol. 1, pp.340-347.

Lévesque, J., K. Staenz, J. Shang, R.A. Neville, P. Yearwood, and V. Singhroy, 1999, "Temporal Monitoring of Mine Tailings Revegetation Using Hyperspectral Data,

Sudbury, Ontario", Proceedings of the Thirteenth International Conference on Applied Geologic Remote Sensing, Vancouver, British Columbia, Canada, Vol. 2, pp. 21-28.

Inco, 1998: http://www.incoltd.com/invest/annrpt/96-env1g.htm.

Mueller, A., P. Strobl, F. Lehmann, and G. Reinhaeckel, 1997, "Case Studies of Airborne Remote Sensing for the Assessment of Mining Impacts", Proceedings of the Third International Airborne Remote Sensing Conference and Exhibition, Copenhagen, Denmark, pp. I-257-226.

Press, W.H., S.A. Teukolsky, W.T. Vetterling, and B.P. Flannery, 1992, Numerical Recipes in C, Cambridge University Press, Cambridge, England, 994 pages.

Shang, J., J. Lévesque, P.J. Howarth, B. Morris, K. Staenz, and P. Yearwood, 1999, "Preliminary Investigation of Acid Mine Drainage Detection Using *casi* Data, Copper Cliff, Ontario, Canada", Proceedings of the Fourth International Airborne Remote Sensing Conference and the 21st Canadian Symposium on Remote Sensing, Ottawa, Ontario, Canada, pp. I-771-778.

Singhroy, V.H., 1996, "Environmental and Geological Site Characterization in Vegetated Areas: Image Enhancement Guidelines", Remote Sensing and GIS for Site Characterization: Applications and Standards, eds. V.H. Singhroy, D.P. Nebert, and A.I. Johnson, ASTM STP 1279, West Coushocken, Pennsylvania, U.S.A., pp. 5-16.

Space Imaging, 1999: http://www.spaceimaging.com.

Staenz, K., 1996, "Classification of a Hyperspectral Agricultural Data Set using Band Moments for Reduction of the Spectral Dimensionality", Canadian Journal of Remote Sensing, 22(3): 248-257.

Staenz, K., and D.J. Williams, 1997, "Retrieval of Surface Reflectance from Hyperspectral Data Using a Look-Up Table Approach", Canadian Journal of Remote Sensing, 23(4): 354-368.

Staenz, K., T. Szeredi, and J. Schwarz, 1998, "ISDAS – A System for Processing/Analyzing Hyperspectral Data", Canadian Journal of Remote Sensing, 24(2): 99-113.

Staenz, K., Neville, R.A., Lévesque, J., Szeredi, T., Singhroy, V., Borstad, G.A., and Hauff, P., 1999, "Evaluation of *casi* and SFSI Hyperspectral Data for Geological Applications - Two Case Studies", Canadian Journal of Remote Sensing (in press).

Swayze, G.A., R.N. Clark, R.M. Pearson, and E. Livo, 1996, "Mapping Acid-Generating Minerals at the California Gulch Superfund Site in Leadville, Colorado using Imaging Spectroscopy", Summaries of the Sixth Annual JPL Airborne Earth Science Workshop, JPL Publication 96-4, Pasadena, California, U.S.A., Vol.1, pp. 231-234,

Szeredi, T., Staenz, K., and Neville, R.A., 1999, "Automated Endmember Selection: Part I Theory", Remote Sensing of Environment (submitted).

Table 1 : Spectral band configuration and spatial resolution for the Quickbird, Orbview3 and Ikonos sensors.

Sensor	**Ikonos2**	**Quickbird**	**Orbview3**
Company	Space Imaging	Earthwatch	Orbital Sciences
Spectral bands (nm)	450 - 520 520 - 600 630 - 690 760 - 900	450 - 520 520 - 600 630 - 690 760 - 890	450 - 520 520 - 600 625 - 695 760 - 900
Spatial resolution	4 m	4 m	4 m

*) as of September 1999

Table 2: *casi* sensor configurations.

Spectral coverage	407-944 nm
Number of bands	72
Spectral sampling interval	7.6 nm
Bandwidth at FWHM*	8.7 nm
Sensor altitude above ground	1905 m
Ground resolution: across track along track	2.5 m 4.3 m
Swath	406 pixels

*) FWHM: Full Width at Half Maximum

Table 3: Input parameters for MODTRAN3 code runs.

Atmospheric model	Mid-latitude Summer
Aerosol model	Continental
Date of overflight	August 24, 1996
Solar zenith angle	31.5°
Solar azimuth angle	176°
Sensor zenith angle	variable
Sensor azimuth angle	variable
Terrain elevation	0.3 km
Sensor altitude above sea level	2.21 km
Water vapour content	2.35 g/cm^2
Ozone column	as per model
CO_2 mixing ratio	as per model
Horizontal visibility	50 km

Table 4: Spectral characteristics of the simulated data sets.

Data Set	**Centre Wavelength (nm)**	**Bandwidth (nm) at FWHM**
8-band	458.7, 518.2, 578.2, 638.6, 699.3, 760.28, 821.4, 882.7	8.7
4-band	503.2, 608.3, 714.5, 821.4	8.7
Geobotany (6 bands)	480.9, 548.1, 608.3, 676.5, 745.0, 829.1	8.5 to 76.5 in increments of 8.5
Ikonos 2	485, 560, 660, 830	80, 80, 60, 140

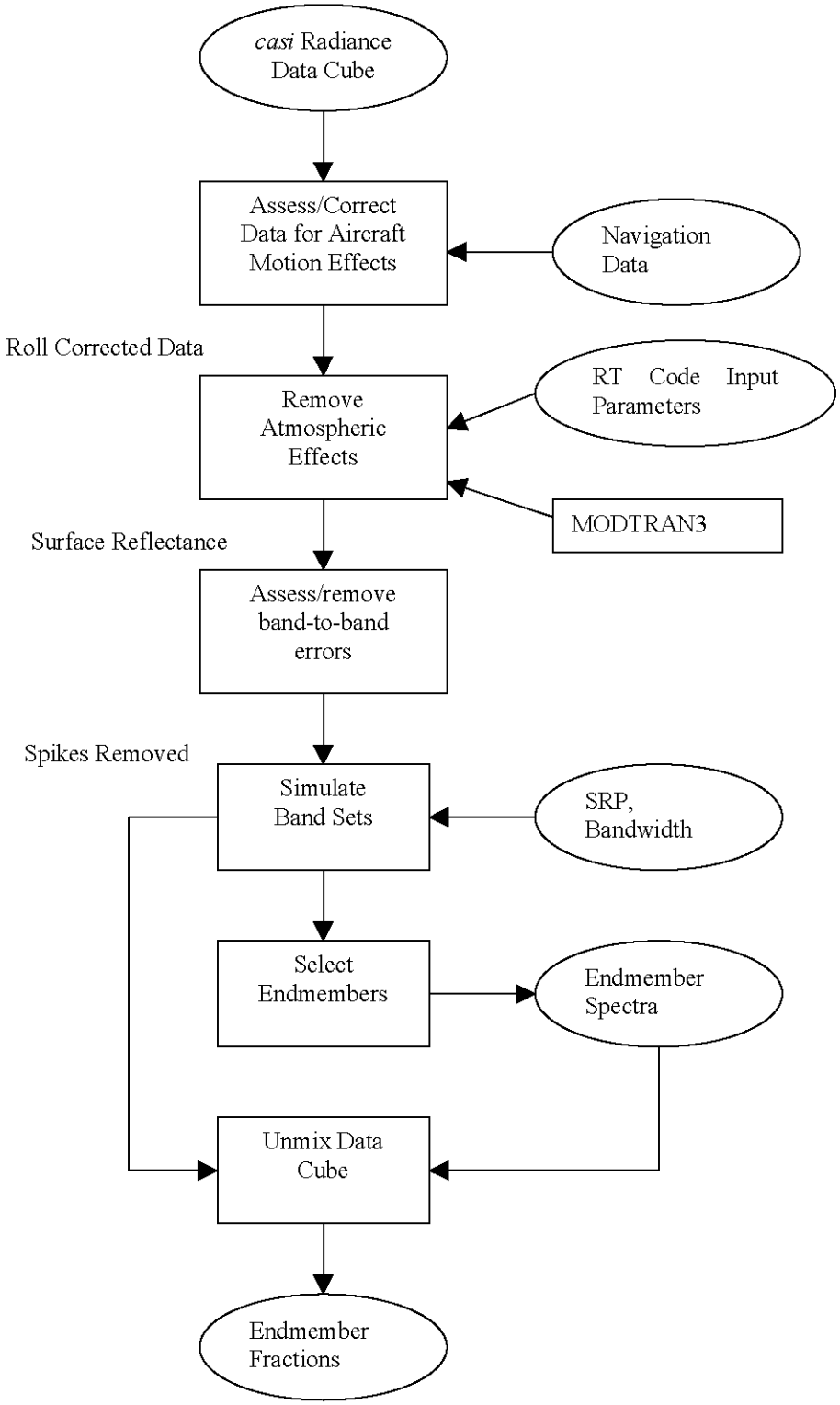

Figure 1: Data processing scheme (SRP = Spectral Response Profile).

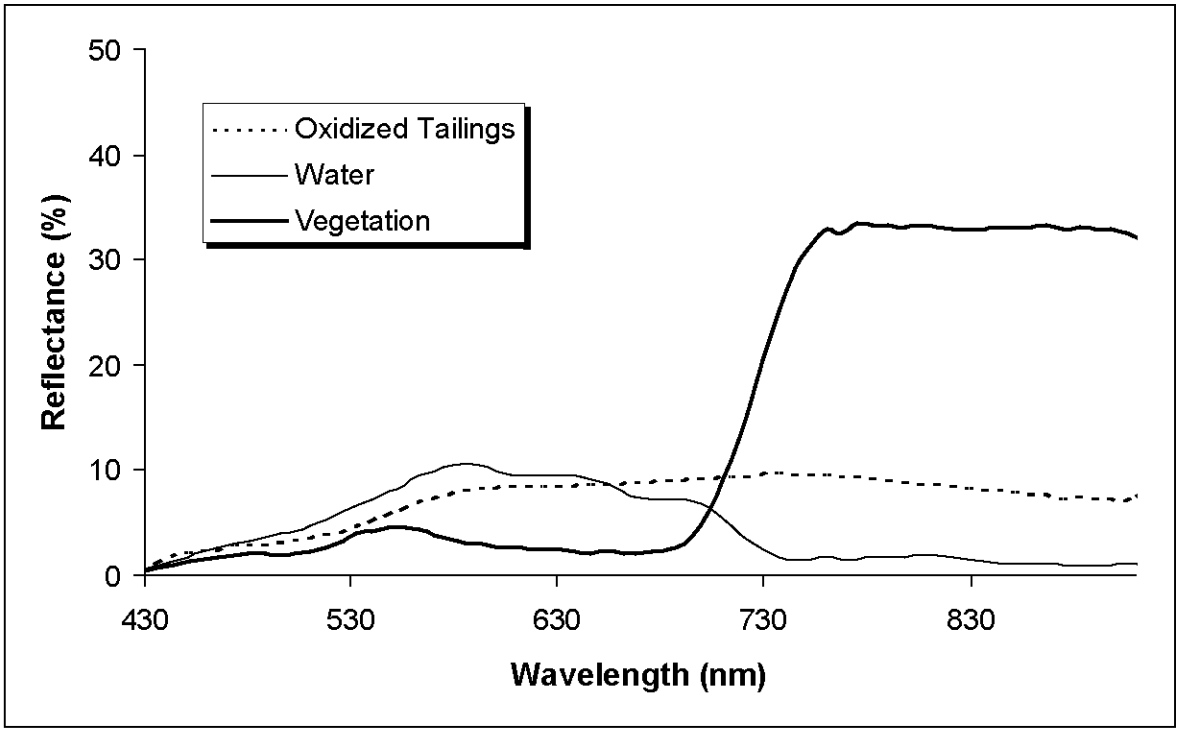

Figure 2: *casi* surface reflectance spectra retrieved from single pixels.

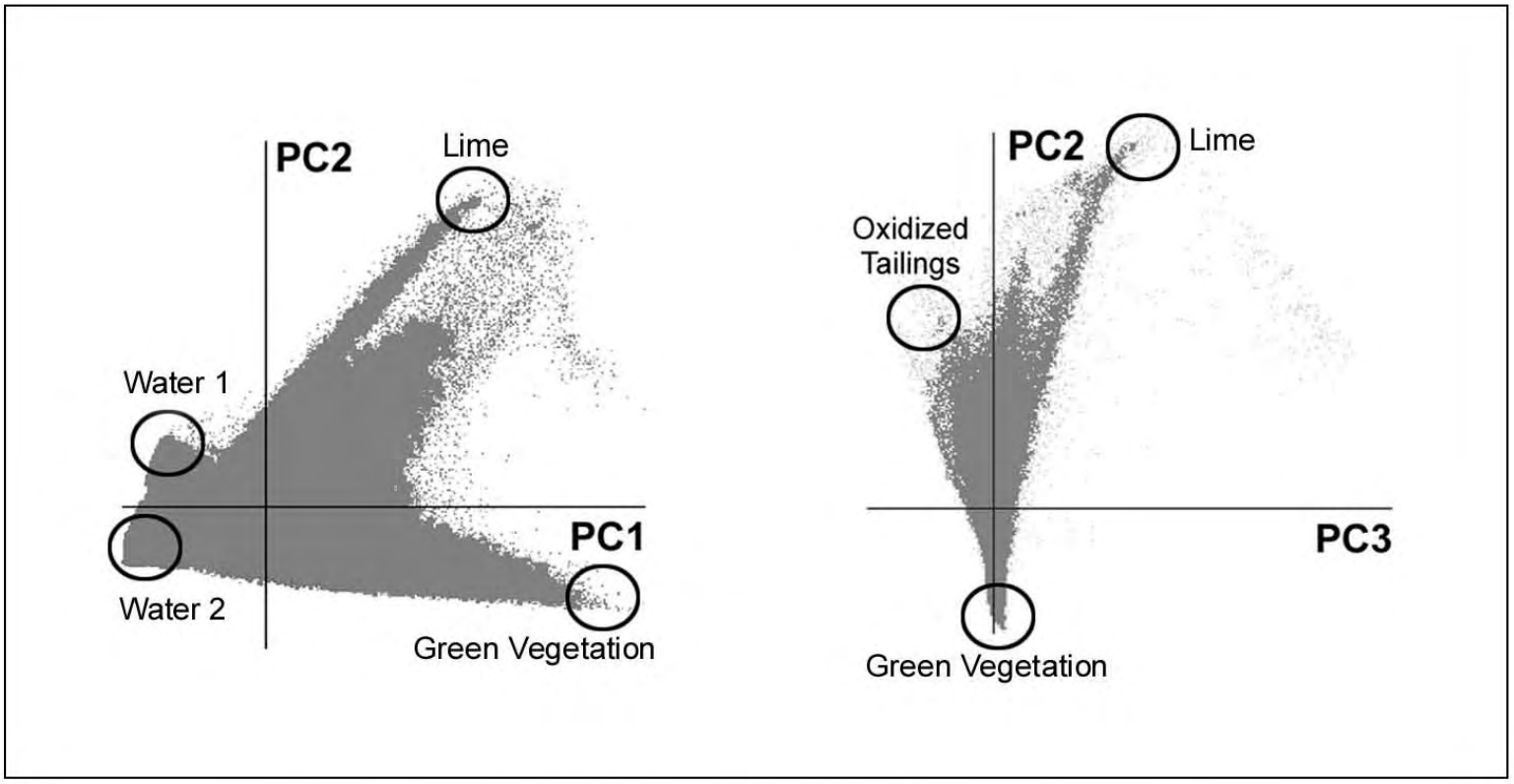

Figure 3: Scatter plots of principal component (PC) 1 versus PC2 and PC3 versus PC2 of the *casi* 65-band data.

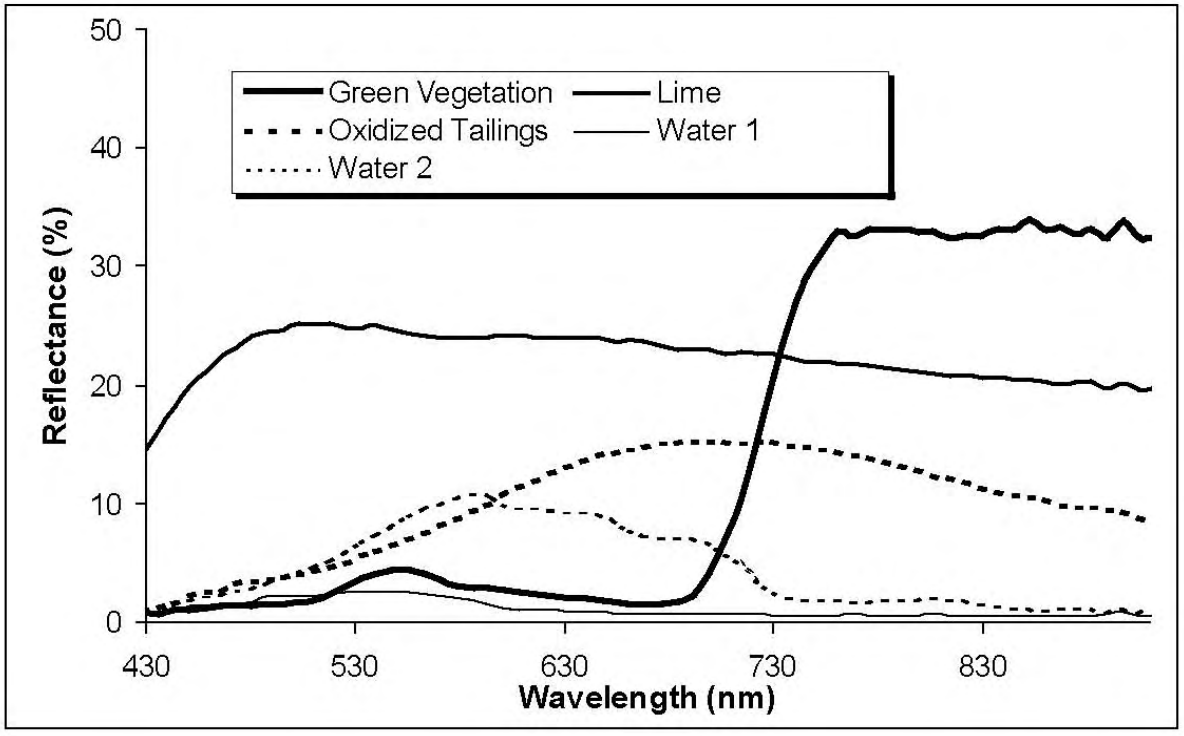

Figure 4: Endmember spectra retrieved from the 65-band *casi* data set.

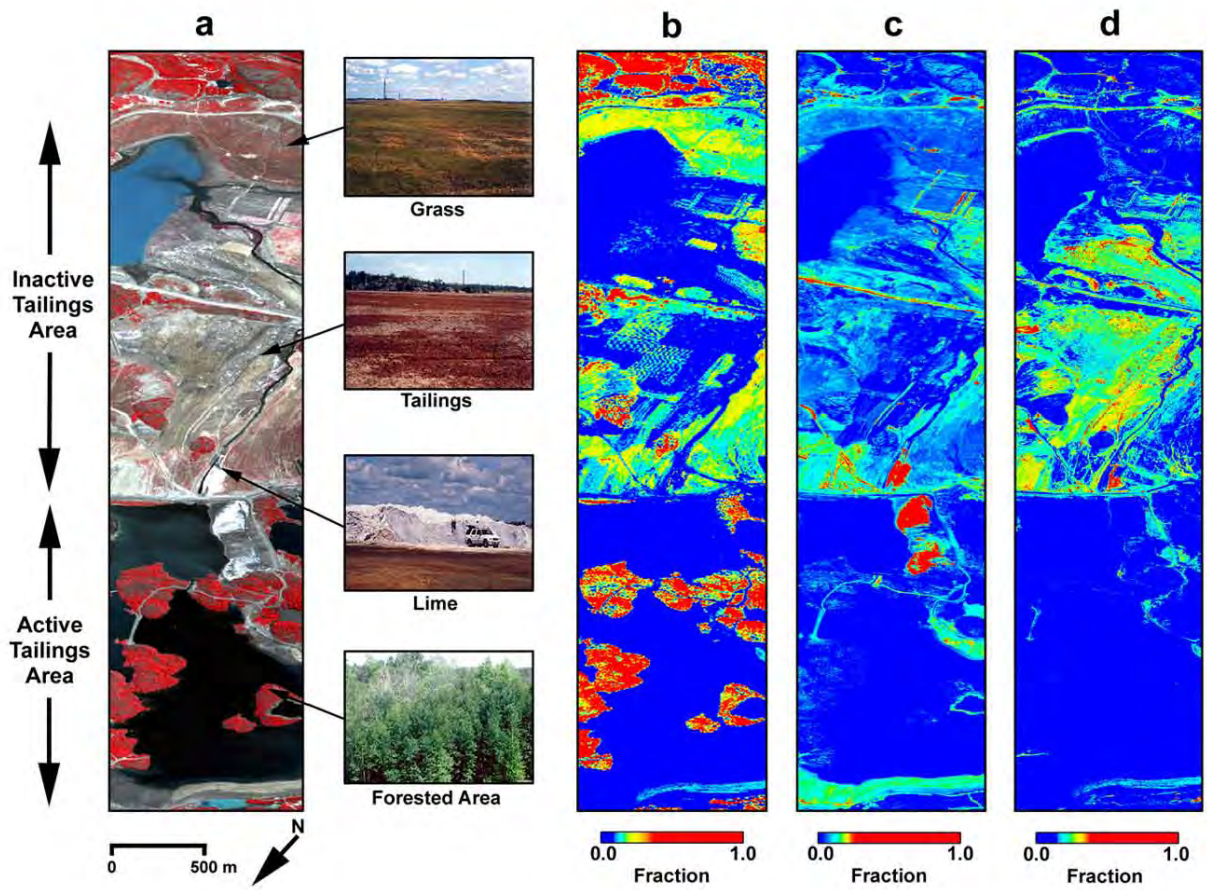

Figure 5: Colour composite and associated pictures showing (a) an overview of the tailings area with fraction images of the three endmembers (b) green vegetation, (c) lime, and (d) oxidized tailings. The colour composite retrieved from the *casi* 65-band data set was generated with bands 19 (540 nm) in the blue, 37 (676 nm) in the green, and 45 (737 nm) in the red, respectively.

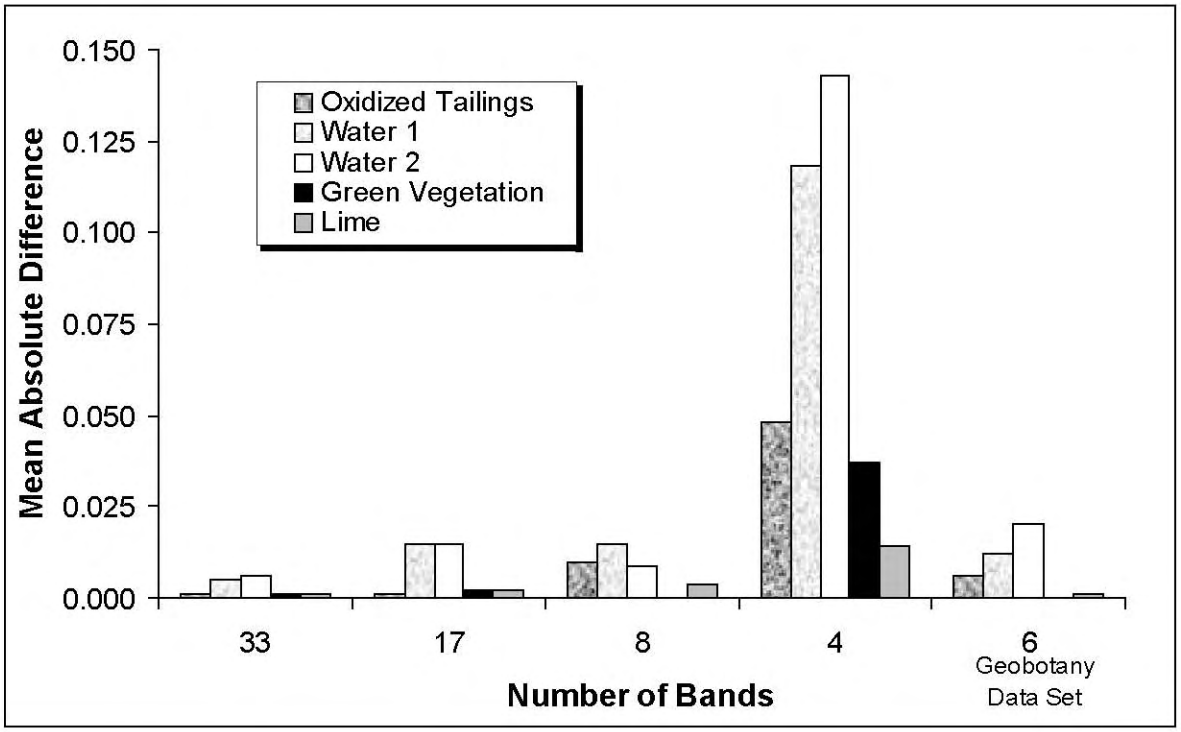

Figure 6: Mean absolute difference between the 65-band unmixing results (endmember fractions) and unmixing results of the band reduction analysis.

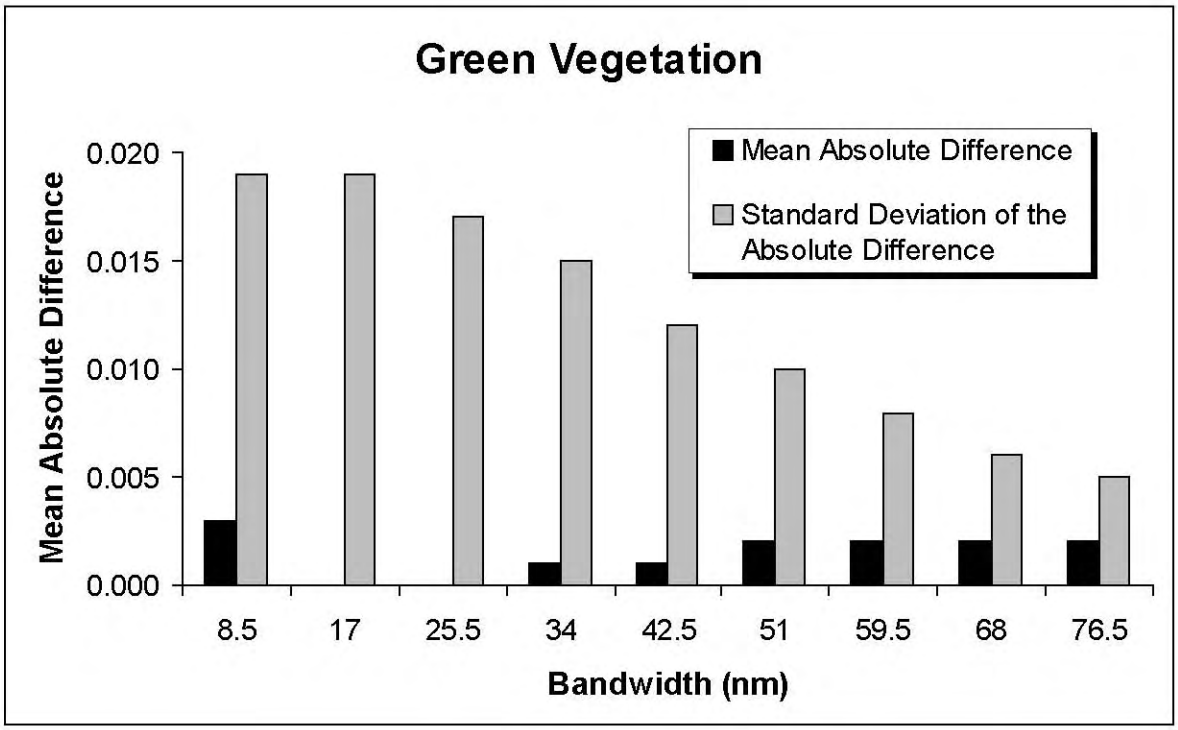

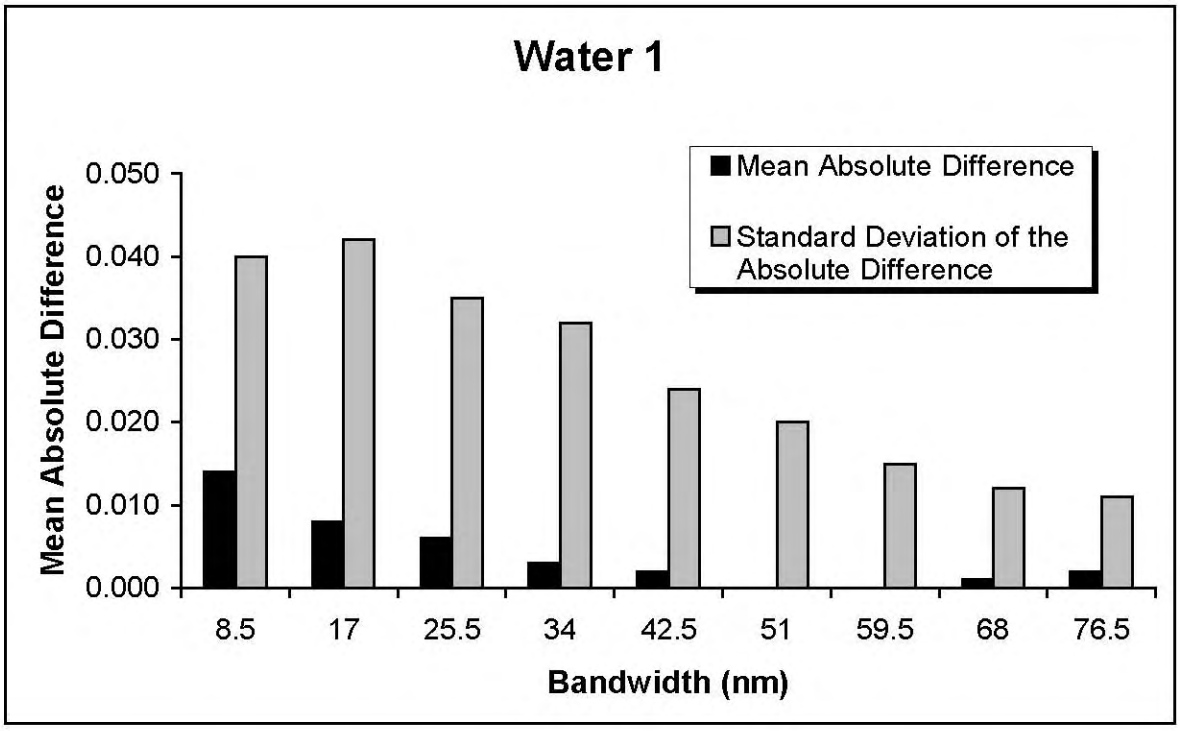

Figure 7: Mean and standard deviation of the absolute difference of the green vegetation and water 1 endmember fractions derived from the 65-band *casi* data and the different bandwidth simulations using the geobotany (6-band) data cube.

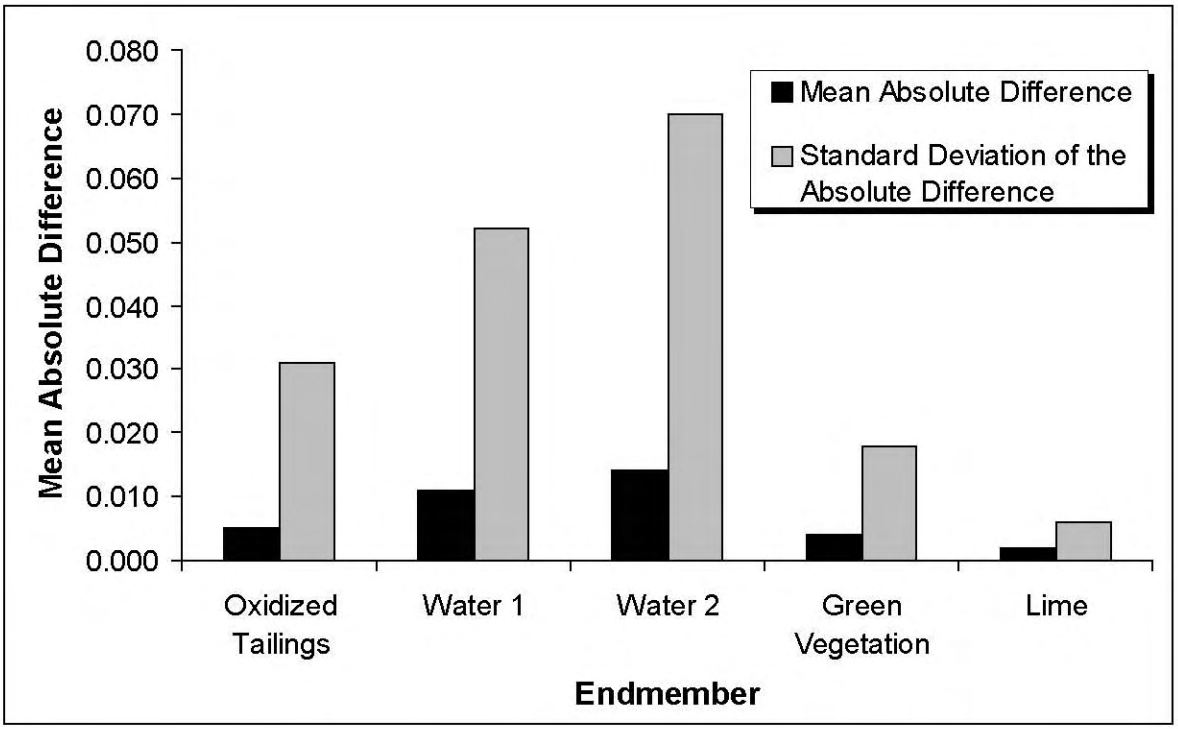

Figure 8: Mean absolute difference between the 65-band unmixing results and the Ikonos 2 simulation unmixing results for each endmember.

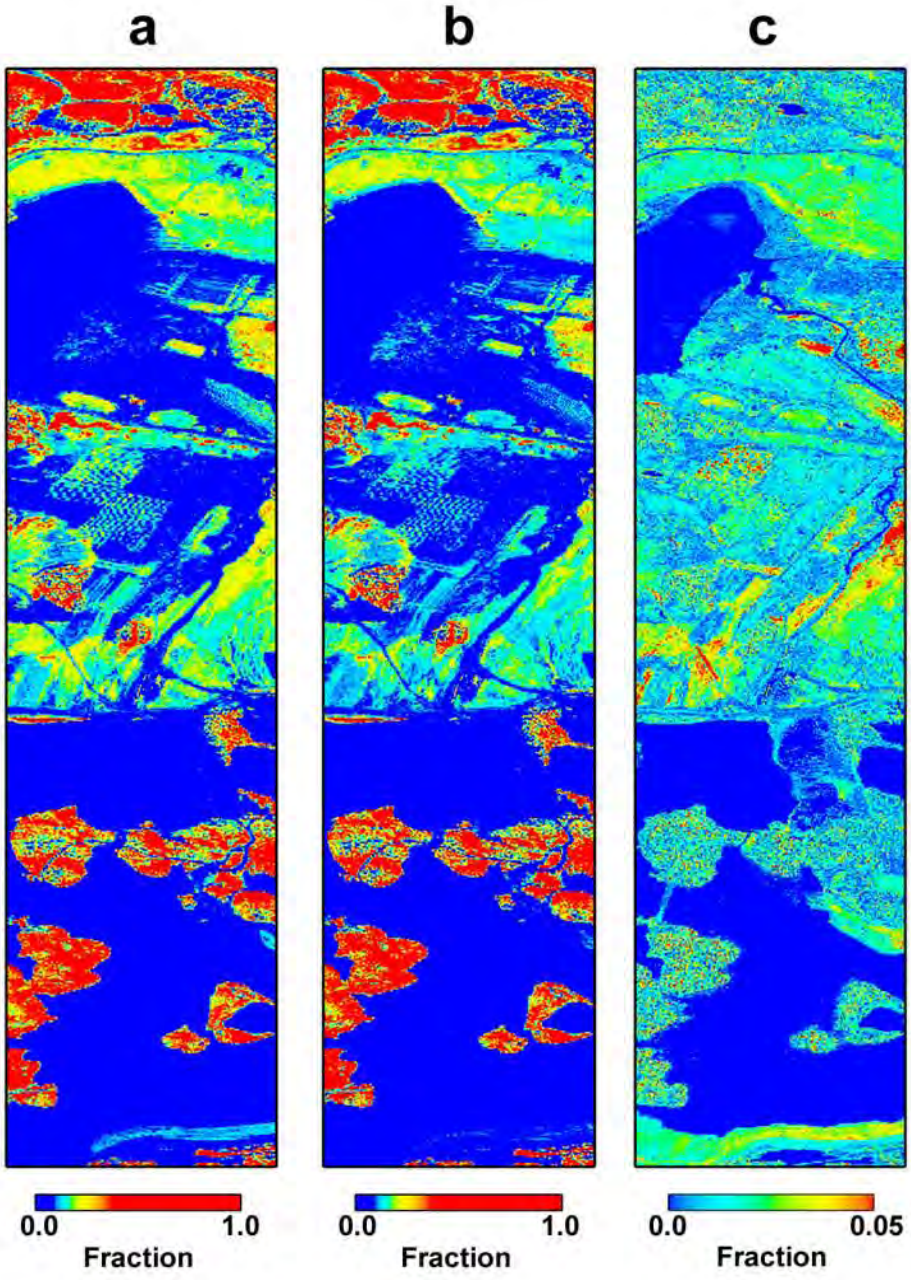

Figure 9: Fraction images retrieved from (a) the 65-band *casi* data and (b) the simulated Ikonos 2 data with (c) associated absolute difference image over the Copper Cliff mine tailings area in Sudbury.

Preprint/Prétirage

TEMPORAL MONITORING OF MINE TAILINGS REVEGETATION USING HYPERSPECTRAL DATA, SUDBURY, ONTARIO*

Josée Lévesque[1], Karl Staenz[2], Jiali Shang[3], Bob Neville[2], Paul Yearwood[4], Vern Singhroy[2]

[1]MIR Télédétection Inc., 2182 de la Province, Longueuil, QC, Canada J4G 1R7
Email : levesque@ccrs.nrcan.gc.ca

[2]Canada Centre for Remote Sensing, 588 Booth St., Ottawa, ON, Canada K1A 0Y7

[3]Laboratory for Earth Observations, University of Waterloo, Waterloo, ON, Canada N2L 3G1

[4]Decommissionning and Reclamation, INCO Limited, Copper Cliff, ON, Canada P0M 1N0

ABSTRACT

Hyperspectral imagery from the Compact Airborne Spectrographic Imager (*casi*) was used to monitor sulphide mine tailings revegetation progress at the Copper Cliff mine in Sudbury, Ontario. A first set of data was acquired on August 24, 1996 in 72 contiguous 9 nm wide spectral bands from 400 nm to 950 nm along with a detailed ground survey. Using the same image acquisition parameters, a second set of data was acquired on August 19, 1998 over the same area along with detailed ground reference measurements. Both sets of image data were classified using constrained linear spectral unmixing. Monitoring was achieved by comparing the 1996 and 1998 image fractions of vegetation. Results indicate that advances in reclamation of the selected sites have been made over the two-year period.

1.0 INTRODUCTION

Rehabilitation of mine tailings sites deals with a complex unnatural soil environment. Acidity is the main factor contributing to tailings infertility. At the Inco Copper Cliff Mine, tailings are the residuals of milling ore from sulphide bearing rocks (Peters, 1988). The resulting sulphide rich tailings oxidize to produce sulphuric acid when in contact with air and water (Kelley and Tuovinien, 1988). This higher acidity contributes to an increase in the availability of heavy metals and other toxic substances which can interfere with plant nutrient uptake and growth. Inco Ltd. is using the lime spreading technique to reduce acidity in the Copper Cliff tailings. Increasing pH using agricultural limestone reduce the mobility of the heavy metals and, therefore, their availability to plants.

In a previous study (Lévesque et al., 1997), the monitoring potential of high spatial and spectral resolution data was demonstrated. Three types of surfaces (vegetation, lime, and oxidized tailings) were quantified using constrained linear spectral unmixing. The resulting image fractions were validated with fractions estimated visually on the ground. This paper presents preliminary results of monitoring the Copper Cliff mine tailings revegetation using multi-temporal data acquired during the summers of 1996 and 1998.

* Presented at the Thirteenth International Conference on Applied Geologic Remote Sensing, Vancouver, British Columbia, Canada, Vol. 2, pp. 21-28, 1-3 March 1999.

2.0 METHODOLOGY

2.1 STUDY SITE

The Inco Copper Cliff tailings impoundment area as outlined in Figure 1 is divided into nine main tailings storage areas (Puro et al. 1995). The tailings represent different stages of activity/reclamation ranging from active areas, where new tailings are being deposited (R1, R2, R3, R4), to inactive areas with well established 30 year old vegetation regrowth (CD). Intermediate between these are inactive areas where revegetation is under way. In Figure 1, areas labelled P and Q were chosen for this study because of their earlier stage of reclamation. Although some trees are present in these areas, they are located on rock outcrops and are not part of the tailings revegetation process. Figure 2 shows a *casi* image (band at 676 nm) containing the sample plots (sub-scenes) that were selected from each tailings area to avoid forested outcrops and to limit the study area to regions where active revegetation work is being done by Inco.

Plot P1 represents an area of older grass growth as compared to plots P2 and Q. It is also located on a hill (from higher to lower part in the image plot). Plot P2 includes an area which was actively revegetated during the last two years (mainly north of the creek) and an area where tailings are predominant (south of the creek). Area Q is dominated by tailings where revegetation work (liming, ploughing, seeding) has been done during the last two years. In all three plots some water, as part of a stream or a pond, was deliberately included to show areas where no changes in vegetation has occurred over the period August 1996 to August 1998 between image acquisitions.

2.2 IMAGE DATA

High spatial and spectral resolution *casi* radiance data were acquired on August 19, 1996 and August 24 1998 in 72 contiguous, 8.7 nm wide spectral bands covering a wavelength range from 407 nm to 944 nm. Pixel size is roughly 2.5 m in the across-track direction and 4 m in the along-track direction. Only wavelengths between 450 nm and 900 nm were used because of the drop-off of the responsivity of the silicon detector at both ends of the *casi* spectrum.

2.3 PROCESSING OF IMAGE DATA

A roll correction was applied to both datasets using the navigation data to remove the most significant aircraft motion from the imagery. Surface reflectance was retrieved using a look-up table (LUT) approach implemented in ISDAS (Staenz and Williams, 1997, Staenz et al., 1998a). After atmospheric correction, an ISDAS algorithm based on spectrally flat targets was used to remove any remaining systematic atmospheric or sensor effects in the data (Staenz et al., 1998b).

2.4 SPECTRAL UNMIXING

Constrained linear spectral unmixing was performed on both 1996 and 1998 *casi* datasets using an algorithm implemented in ISDAS (Szeredi et al., 1998; Boardman, 1989 and 1990). In linear unmixing, the spectrum from each pixel in the data cube is decomposed into a linear combination of "endmembers" spectra which represent in this case the spectra of the purest pixels in the scene.. The first step in the process involves a principal component decomposition; only the first three principal

components (PC) were retained, which respectively account for 77%, 21%, and 1% of the variability in the 1996 dataset and 85%, 12% and 1% of the variability in the 1998 dataset. Figure 3 shows the scatter plots in the three PC dimensions for both 1996 and 1998 data. The endmember spectra are those corresponding to the extremities of these scatter plots; these are selected manually and their locations are indicated in Figure 3. The same endmembers were identified for both years: lime, vegetation, oxidized tailings, and two types of water. The spectra of all endmembers are displayed in Figure 4. Each data cube was unmixed in terms of the five identified endmember spectra. This resulted in a "fraction" image for each endmember. In each fraction image the pixel values correspond to the contribution of this endmember to the total reflectance of the *casi* data.

2.5 COMPARISON OF 1996 AND 1998 RESULTS

The fraction images of the endmember "vegetation" from both years were overlayed to within a RMS error of less than ±2 pixels in both spatial dimensions. This was achieved by performing an image to image registration using a third-order polynomial in combination with ground control points. A procedure which provides more accurate results as performed by Gibson (1994) was not possible because a full set of navigation data was not collected during the *casi* data acquisition. The three plots (P1, P2, Q, Figure 2) were reimaged in Figure 5 as differences (1998-1996).

3.0 RESULTS AND DISCUSSIONS

The first column in Figure 5 shows the maps of the absolute difference between vegetation image fractions derived from the 1996 and 1998 *casi* plots P1, P2, and Q, specifically the vegetation fraction of 1998 minus the vegetation fraction of 1996. The second and third columns show the scatter plots of both years for the same plots and their histograms.

On the difference maps, light tones represent positive differences between fractions of 1998 and fractions of 1996 and indicate areas where vegetation density has increased during the two-year period. Dark tones indicate a decrease in vegetation density. Middle tone (zero difference) shows vegetation areas which have not changed between the two image dates. As expected, the water, which contains no vegetation, appears grey corresponding to zero difference. The creek is hardly distinguishable in the difference map of the plot Q since there has been little change along its boundaries over this time period.

The difference map of plot P1 shows an increase of vegetation density in the lower part of the hill while the upper part shows a decrease. This could indicate a drainage effect. Plot P2 exhibits a general vegetation increase in the upper right quarter where revegetation work has been done over the last two years. The lower part, which is composed of tailings shows a medium tone indicating small changes between 1996 and 1998. Various patterns resulting from revegetation work are apparent in the difference map of plot Q; in particular, fine striations on the left side of the image are caused by ploughing performed in 1996. The brighter areas in the Q map result from more recent seeding. The dark area in the upper left corner was seeded in 1996 and ploughed over in 1998 so that the fraction difference is negative on the rows where grass was growing in 1996.

In all three scatter plots it appears that there are more points above the diagonal (equal fractions line) than below it. This indicates qualitatively an overall increase of vegetation between 1996 and 1998. A more quantitative result can be obtained from the vegetation fraction histograms. For area P1, the 1996

histogram peaks at a fraction of 0.20 and goes to zero at fraction 0.30; in contrast, the 1998 histogram peaks at fraction 0.22 and vanishes at 0.45. For area P2, both have a primary peak at approximately 0.10, the histogram for 1998 has a secondary peak at 0.20 and vanishes at about 0.31, while that for 1996 decreases gradually to zero at 0.35. Those pixels exhibiting the highest vegetation fractions in 1996 appear to have been destroyed by subsequent activities. Area Q has a significant proportion of pixels in 1998 which have fractions above the 0.30 cutoff of the 1996 data, indicating a strong improvement in revegetation.

Because of a RMS misregistration error of ±2 pixels, it was not possible to extract quantitatively accurate results on a pixel-by-pixel basis. This misregistration which represents 5 to 8 m on the ground is sufficient to cause significant errors in the comparison of the 1996 and 1998 data, especially in regions which are not homogenous. However, the analysis confirms that vegetation cover has increased from 1996 to 1998.

4.0 CONCLUSION AND RECOMMENDATIONS

This study has demonstrated the feasibility of the technique used to achieve temporal monitoring of vegetation regrowth over reclaimed mine tailings sites. The results indicate that advances in reclamation of the selected sites have been made over the period between August 1996 and August 1998. If it is desirable to have quantitative vegetation regrowth results on a pixel-to-pixel basis, then accurate aircraft track and attitude data have to be obtained to be able to overlay image data within sub-pixel accuracy.

5.0 REFERENCES

Boardman, J.W., "Inversion of Imaging Spectrometry Data Using Singular Value Decomposition", In *Proceedings of the 1989 International Geoscience and Remote Sensing Symposium (IGARSS'89) and the 12th Canadain Symposium on Remote Sensing*, Vancouver, BC, Vol. 4, pp. 2069-2072, 1989.

Boardman, J.W., "Inversion of High Spectral Resolution Data," In *Proceedings of SPIE Conference on Imaging Spectrometry of the Terrestrial Environment*, Orlando, Florida, Vol. 1298, pp. 222-233, 1990.

Gibson, J., "Photogrammetric Calibration of a Digitsl Electro-Optical Stereo Imaging System", In *Geomatica*, Vol. 48, No. 2, pp. 95-109, 1994.

Kelley, B.C. and Tuovinien, O.H., "Microbiological oxidation of minerals in mine tailings", In *Chemistry and Biology of Solid Waste*, eds. W. Salomons and U. Forstner, Springer-Verlag, New-York, pp.33-53, 1988.

Lévesque, J., Szeredi, T., Staenz, K., Singhroy, V., Bolton, D., "Spectral Unmixing for Monitoring Mine Tailings Site Rehabilitation, Copper Cliff Mine, Sudbury, Ontario", In *Proceedings of the Twelfth International Conference and Workshops on Applied Geological Remote Sensing*, Denver, Colorado, 17-19 November 1997.

Peters, T.H., "Mine Tailings Reclamation. Inco Limited's Experience with the Reclaiming of Sulphide Tailings in the Sudbury Area, Ontario, Canada", In *Environmental Management of Solid Waste*, eds. W. Salomons and U Forstner, Springer-Verlag, New-York, pp. 152-165, 1988.

Puro, M.J., Kipkie, W.B., Knapp, R.A., McDoanld, T.J., and Stuparyk, R.A., "Inco's Copper Cliff Tailings Area", In *Proceedings of the Sudbury'95 Conference on Mining and the Environment*, Sudbury, Ontario, May 28 – June 1, Vol. 1, pp. 181-191, 1995.

Staenz, K. and Williams, D.J., "Retrieval of Surface Reflectance from Hyperspectral Data using a Look-Up Table Approach", *Canadian Journal of Remote Sensing*, Vol. 23, No. 4, pp. 354-368, 1997.

Staenz, K., Szeredi, T., Schwarz, J., "ISDAS – A System for Processing/Analysing Hyperspectral Data, *Canadian Journal of Remote Sensing*, Vol. 24, No. 2, pp. 99-113, 1998a.

Staenz, K., Neville, R.A., Lévesque, J., Szeredi, T., Singhroy, V., Borstad, G.A., and Hauff, P., "Evaluation of *casi* and SFSI Hyperspectral Data for Environmental and Geological Applications – Two Case Studies", *Canadian Journal of Remote Sensing*, Vol. 25, No. 3, pp. 311-322, 1999.

Szeredi, T., Staenz, K., and Neville, R.A., "Automatic Endmember Selection: Theory", *Remote Sensing of Environment* (to be submitted).

6.0 ACKNOWLEDGEMENT

The *casi* datasets used in this study were acquired by the Center for Research in Earth and Space Technology (CRESTech). The authors wish to thank Dr. Phil Howarth from the Waterloo Laboratory for Earth Observations for making the 1998 data available to the Canada Centre for Remote Sensing. The help and contribution of M. Feng Hou to the field work campaign of 1998 was greatly appreciated.

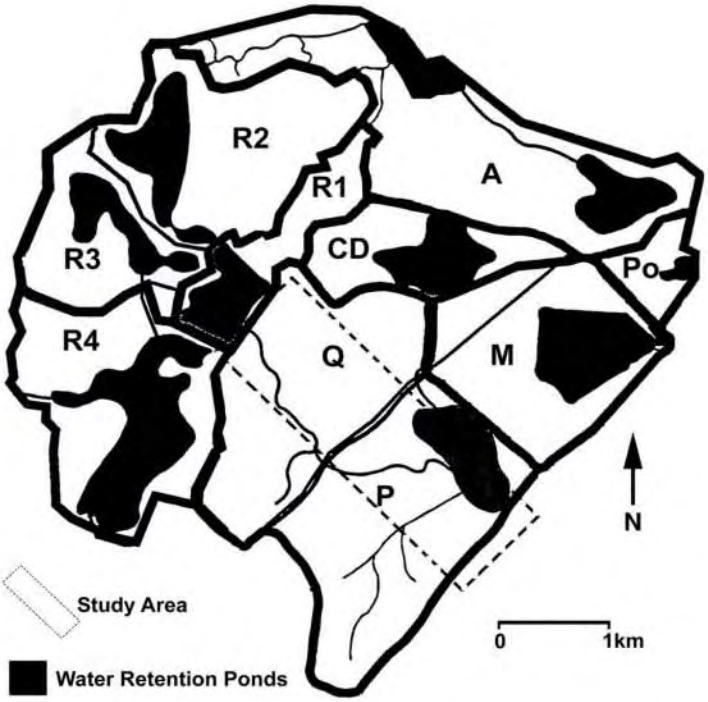

Figure1. Copper Cliff tailings Impoundment area.
(Modified from Puro et al., 1995).

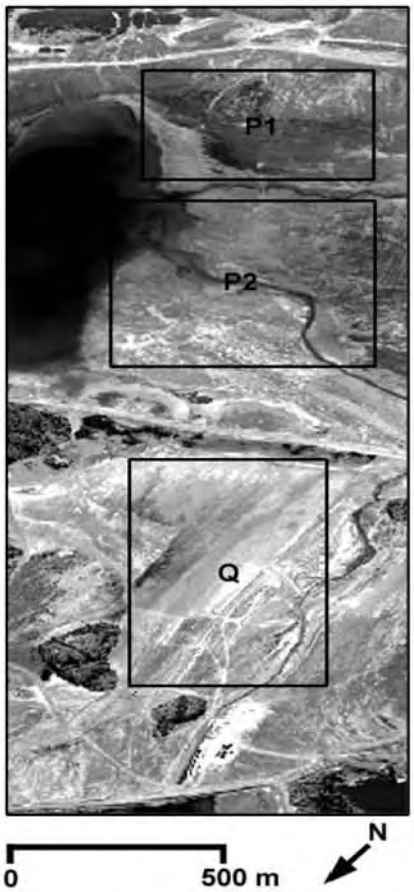

Figure 2. 1998 *casi* band 676 nm showing study plots extracted from P and Q areas.

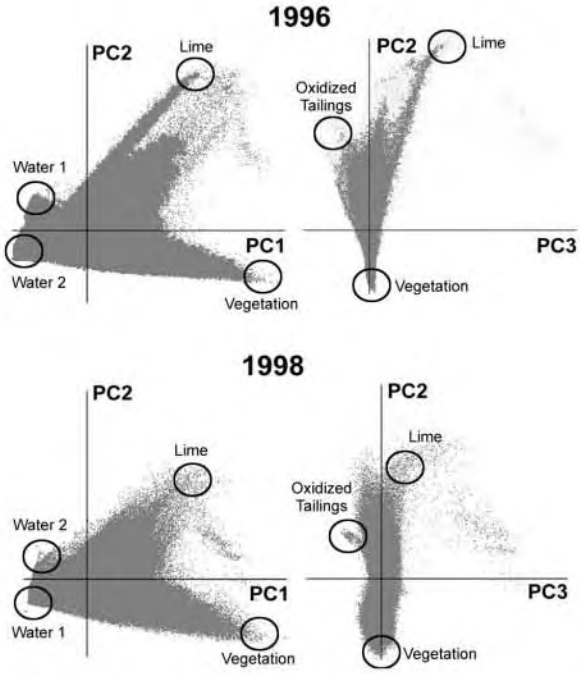

Figure 3. Scatter plots of PC1 versus PC2 and PC3 versus PC2 of 1996 and 1998 data showing the 5 endmembers

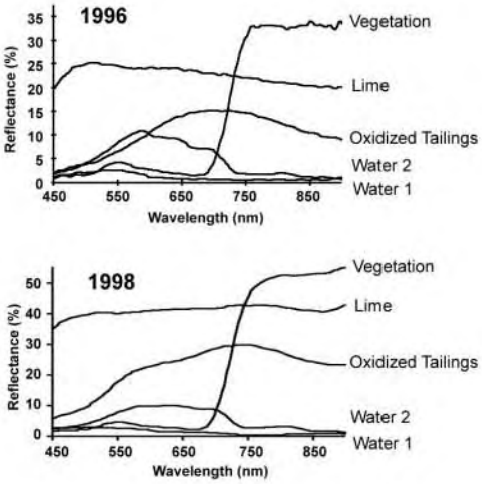

Figure 4. Endmember spectra.

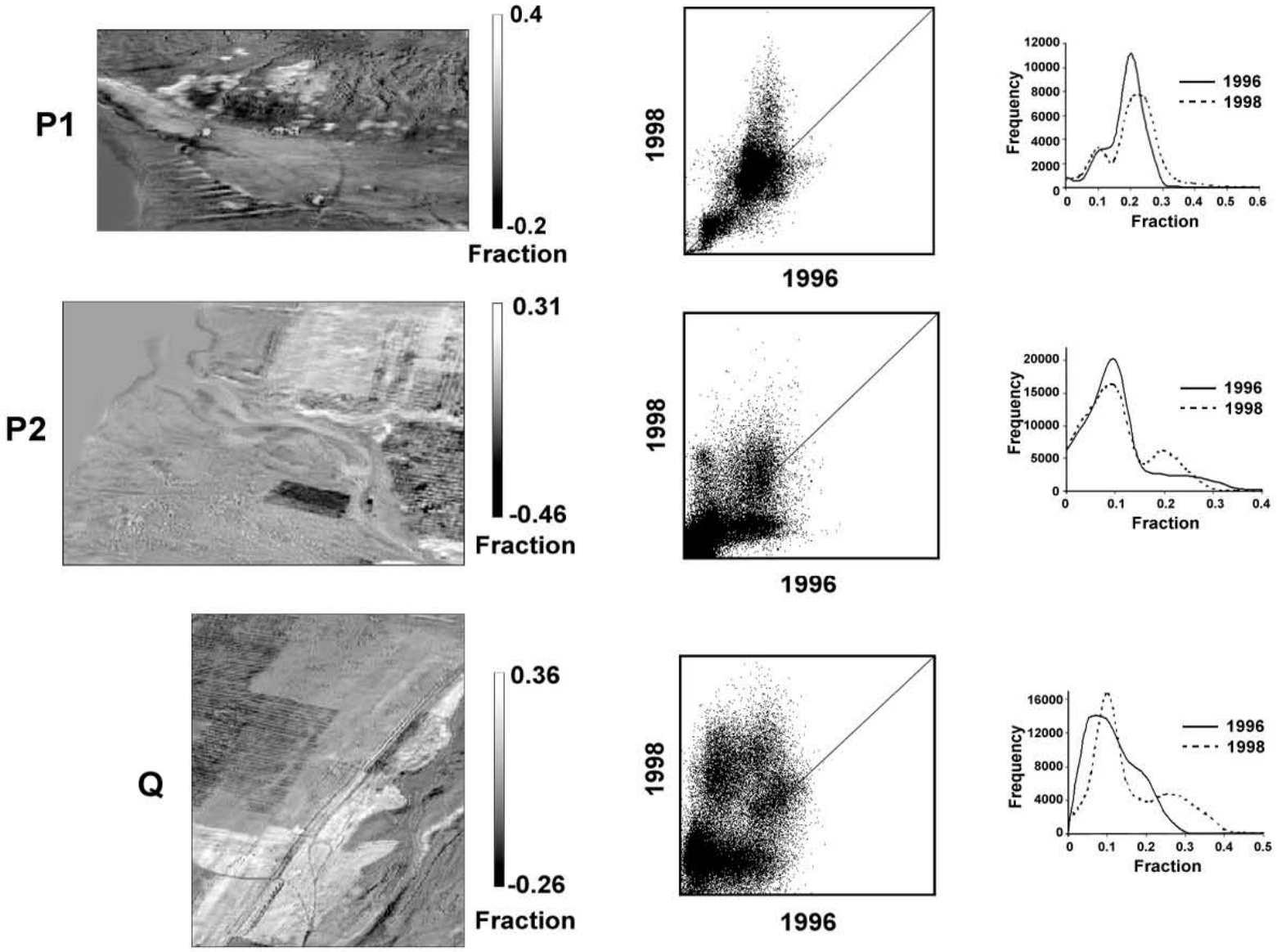

Figure 5. Maps of the absolute difference between 1998 and 1996 vegetation fractions (on the left), scatter plots of 1998 versus 1996 vegetation fractions (middle), and frequency distribution of vegetation fractions for each plot (on the right).

Investigating *casi* Responses to Different Levels of Tailing Oxidation: Inco Copper Cliff Tailings Area, Northern Ontario, Canada

Jiali Shang[1], Josée Lévesque[2], Karl Staenz[3], Philip Howarth[1], Bill Morris[4], Lisa Lanteigne[5]

[1]Waterloo Laboratory for Earth Observations, Department of Geography, University of Waterloo
Waterloo, Ontario, Canada N2L 3G1 e-mail: j2shang@fes.uwaterloo.ca

[2]MIR Télédétection Inc., 2182 de la Province, Longueuil, Québec, Canada J4G 1R7

[3]Canada Centre for Remote Sensing, 588 Booth Street, Ottawa, Ontario, Canada K1A 0Y7

[4]School of Geography and Geology, McMaster University, Hamilton, Ontario, Canada L8S 4M1

[5]Decommissioning and Reclamation, Inco Limited, Copper Cliff, Ontario, Canada P0M 1N0

Abstract

*Sulphide-rich tailings cause acid mine drainage (AMD) when they are in contact with oxygen and water. AMD can contaminate surface and ground water, which in turn can degrade the quality of the environment. Knowledge of the progress of oxidation and also the spatial distribution of tailings materials are of considerable importance when developing programs to provide effective control of tailings sites. In this paper, the potential of Compact Airborne Spectrographic Imager (*casi*) data for providing information on variations in the oxidation of tailings is investigated.*

Spectral-mode casi *data were acquired on August 19, 1998 in 72 bands covering the wavelength range of 400 nm to 950 nm. Twenty-one tailings samples were collected concurrently with the* casi *overflight. Reflectance was measured at all the sample locations using a GER 3700 spectrometer. Sample spectra from the GER were matched with the minerals from the USGS spectral library. Spectral matching revealed that the most likely minerals on this site are pyrite, pyrrhotite, jarosite, and goethite. Image spectra extracted from the casi data over the same sample locations were also matched to the USGS spectral library. Similar results were found in spite of the limited spectral coverage of the* casi. *Spectral unmixing of a test site within the* casi *imagery demonstrated the potential of this instrument to provide information on separating the zones of varying oxidation in the tailings. However, no direct relationships were found between the oxidation phases and the age of the tailings.*

Introduction

Most mine tailings contain a considerable amount of reactive sulphides which, when exposed to oxygen and water, will result in breakdown and oxidiation of the sulfide minerals that eventually lead to acid mine drainage (AMD) (Pearson *et al.*, 1997). AMD typically has pH values in the range of 2-4 and high concentrations of metals and dissolved salts which can cause ground- and surface-water contamination (Ash *et al.*, 1951; Nordstorm and Apers, 1999).

The occurrence of AMD has been identified as the largest environmental problem facing the Canadian mining industry. There is a clear need for developing methodologies for the repetitive, long-term monitoring of mine-tailing sites to ensure that

damage to the environment is kept to a minimum. In recent years, remote sensing techniques have gained increasing popularity over the traditional surface methods for monitoring mine-tailing sites (Farrand and Harsanyi, 1997; Lévesque *et al.*, 1997; Pearson *et al.*, 1997; Boine *et al*, 1999; Shang *et al.*, 1999; Swayze *et al.*, 2000). It is general believed that spectra covering both the visible and the short-wave infrared are needed for mineral mapping. Image data covering only the visible and near-infrared (VNIR) wavelengths are not considered adequate for mineral detection. This is because of the strong absorption features of minerals occurring in the short-wave infrared region of the electromagnetic spectrum. However, a study by Shang *et al.* (1999) revealed that Compact Airborne Spectrographic Imager (*casi*) data can be used to detect the occurrence of acid mine drainage through the association of oxidized tailings with iron oxides. Genesis of iron oxide minerals is a direct consequence of the chemical process leading to AMD generation. Iron oxides are optically typified by various shades of yellow, red, and brown colouration in rocks, soils, and water. They can be identified using the VNIR portion of the spectrum as recorded by the *casi* sensor. The results of this study will assist mining companies in monitoring the migration of AMD. Using remote sensing as a screening tool to identify possible affected sites, a more detailed survey can be conducted targeting these key areas in order to reduce the time and cost. Accordingly, proper control can be applied to mitigate the negative impact of mine tailings on the surrounding environment (Swayze *et al.*, 2000).

This current study investigates the potential of *casi* data for more detailed mine-tailing characterization and AMD detection. The data used are from three sources: high-spatial-resolution hyperspectral *casi* imagery, field spectra acquired with the GER, and mineral spectra from the United States Geological Survey (USGS; USGS, 2000) spectral library.

Study Site

The study site is located at Inco Limited's Copper Cliff tailings complex, Ontario, Canada. It is the largest acid-generating tailings site in Canada, approximately 22.3 km^2, and has resulted from approximately 100 years of mining operations (Puro *et al.*, 1995). Through the years, the tailings areas have been partitioned by tailing dams and have been named alphabetically, A to R, from the oldest to the most recent (Figure 1). Areas A to Q are inactive tailings and have been subjected to intensive reclamation activities, including liming and revegetation. Area R is still receiving tailings. This setting provides an excellent opportunity to study the evolution of tailings over time. Individual partitions within the tailings complex contains a range of mine-tailing compositions with different levels of vegetation regrowth. The major surface-cover types are fresh tailings, oxidized tailings, tailing-retention ponds, rock outcrops and vegetation. The average altitude is 300 m above sea level with an elevation range of 30 m.

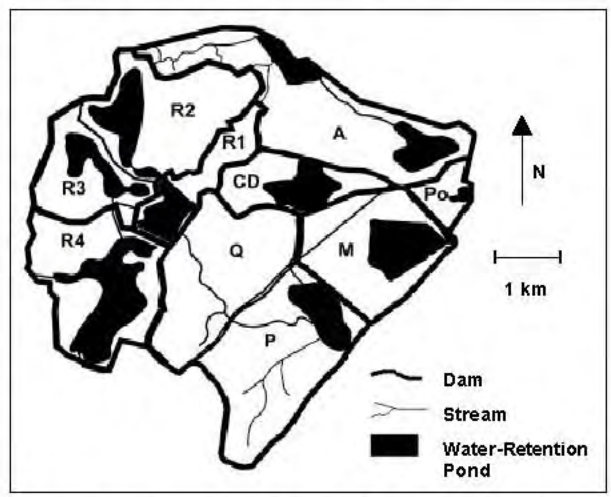

Figure 1. Map of the study site (Modified from Puro et al., 1995)

Data Acquisition and Preprocessing

Hyperspectral *casi* imagery was acquired over the study site on August 19, 1998 from an altitude of 2100 m. The entire tailings were covered with eight flightlines. The data were collected in 72 bands between 400 nm and 950 nm. The bandwidth at full width of half maximum (FWHM) is 10 nm with a spectral sampling interval of 10 nm. The spatial resolution is 4 m by 4 m, resulting in a swath width of 1.6 km (406 pixels).

Tailings samples were collected at 21 locations through the study site concurrently with the *casi* data acquisition. The samples cover different tailings areas within the mining complex to include

tailings of various mineral compositions and oxidation stages. Locations of the sample points are shown in Figure 2. Each sample was gathered from the top of the tailings surface. Reflectances of the tailings samples were measured in the laboratory using a GER 3700 spectroradiometer. The measured reflectance covers 400 nm - 2500 nm of the electromagnetic spectrum.

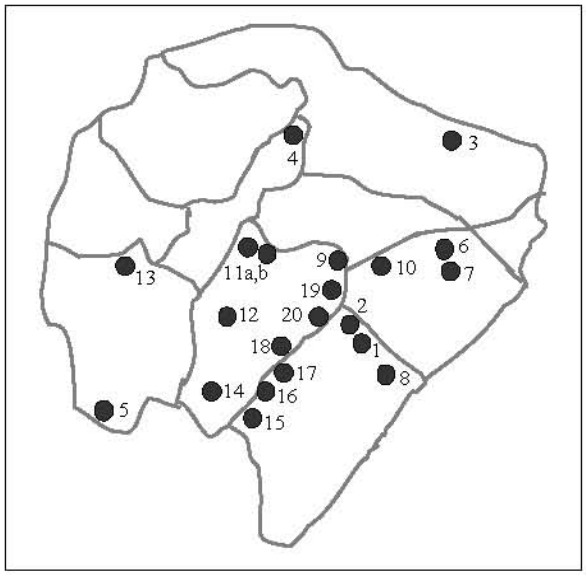

Figure 2. Locations of the tailings samples

Preprocessing of the *casi* data involves three steps: noise removal, atmospheric correction and spectral post-processing. These preprocessing steps will ensure the later extraction of clean endmember spectra which will subsequently lead to better unmixing results.

Noise Removal: This step was carried out in principal component (PC) feature space using the unstriping module implemented in the Imaging Spectrometer Data Analysis System (ISDAS: Staenz *et al.*, 1998). Initially, a PC transformation was performed on the original *casi* radiance data. By doing this, the striping (non-periodic banding noise) and random noise inherent in the original radiance data were enhanced and separated from the signal. The first 6 PC features are of good quality; therefore, they were excluded from this process. The unstripping procedure adjusts the mean of the stripes by applying a gain to that stripe to remove the striping. This is achieved by initially plotting the mean of each line for the remaining PC features against the line number. A triangular smoothing was then applied to the mean curve to remove the spikes in the spatial domain. This enabled the computation of a correction factor (gain) for each line to adjust the original mean values to the smoothed ones. Random sensor noise was eliminated by passing a 3 by 3 average filter through the data. The noise-removed data cube was then inverse-transformed back to its original band form. Figure 3 shows the effect of noise removal from the *casi* data.

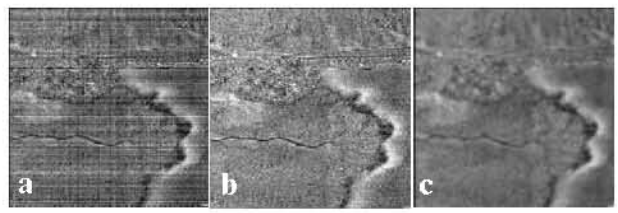

Figure 3. Principal component feautre 9 of casi radiance data of the test site a) original, b) unstriped, and c) spatial averaged

Reflectance Retrieval: The noise-removed *casi* radiance data were converted to reflectance using the surface reflectance retrieval procedure in ISDAS. This procedure, developed by Staenz and Williams (1997), is based on a look-up table (LUT) approach to remove atmospheric effects. It considers the wavelength, pixel position, atmospheric water vapour, aerosol optical depth, and terrain elevation for the generation of the LUTs. The MODTRAN3 radiative transfer code was used to create the LUTs. Figure 4 shows a retrieved *casi* reflectance image of the test site.

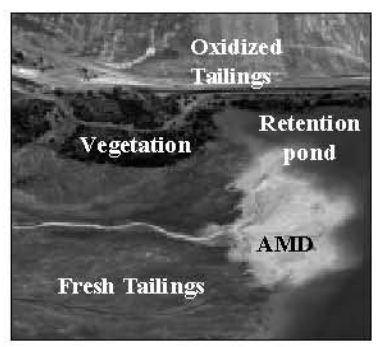

Figure 4. Sub-scene of the casi reflectance image (band 35 centred at 661 nm)

Methods

The study is intended to investigate the potential of *casi* data for mapping variations in tailings

oxidation. This was accomplished through two approaches. First of all, fraction maps of the test site were studied to reveal the spatial relationship of the endmembers. Secondly, GER spectra and *casi* image spectra were compared with minerals from the USGS spectral library.

Spectral Unmixing: Using the *casi* reflectance data, constrained linear spectral unmixing was performed with 10 endmembers on the test scene. These endmembers were selected from the image data with the automated endmember selection tool implemented in ISDAS. This technique applies an iterative error analysis (IEA) scheme to automatically extract endmembers from an image cube (Szeredi *et al.*, 2000). The IEA method performs a series of constrained unmixings, each time choosing as endmembers those pixels with the largest errors.

Spectral Matching: Spectral matching was conducted on all of the GER-measured spectra by comparing them with the 498 mineral spectra from the USGS library. Both spectral angle and correlation measures were used to perform the spectral matching.

Spectral matching was also conducted using spectra extracted from the *casi* data at the same locations where the samples were taken. The *casi* spectra were then compared with the USGS spectral library to investigate whether the spectral matching will reveal similar results to the GER spectra.

Results and Discussion

Spectral Unmixing: The results of the constrained linear unmixing using the 10 endmembers were examined in the form of fraction maps. Endmember fraction maps permit the comparison of the variabilities of fractions of the endmembers in a spatial context. The resulting fraction maps discriminate between surface cover types: vegetation, fresh tailings, various oxidized tailings, and water. Among the 10 endmembers, endmembers 2, 5, 8 and 10 were of most interest since they revealed a unique pattern of a mixture of oxidized tailings (em5, 8, 10) and water (em2). The spectra of these four endmembers are shown in Figure 5.

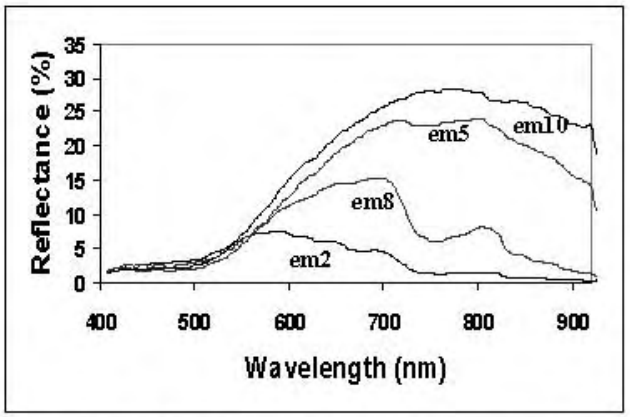

Figure 5. Selected endmember (em) spectra derived from the casi data covering the scene shown in Figure 4

It can be seen from Figure 6 that these four endmembers form a concentrically zoned fan-shaped pattern at the point where a surficial stream discharges into a retention pond. The zonation defined by these endmembers may depict differences in concentration of the sediments (oxidized tailings) in water, or deposition of minerals of different grain sizes. They may also outline the progressive interaction between differing chemistries of the surface run-off (AMD) and the retention pond (water).

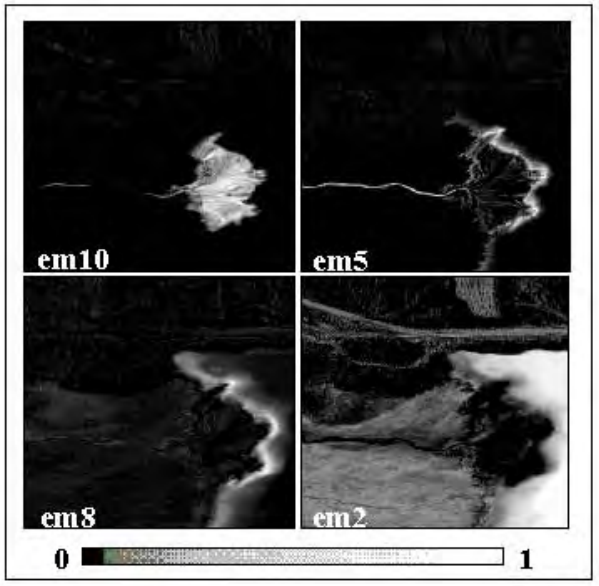

Figure 6. Fraction maps of endmenbers (em) 2, 5, 8, and 10.

Visual examination of the endmember spectra of AMD (em10) and water (em2) in Figure 5 suggests that the intermediate endmember spectra (em5 and 8) are not a simple combination of the outer spectra (em2 and 10). For instance, the em8 spectrum has an apparent broad absorption feature near 730 nm and the reflectance rises again near 800 nm. This supports the hypothesis that these fraction maps reflect the sequential generation of different mineral species.

Spectral Matching: Spectral matching of em10 (oxidized tailings) using both spectral angle and correlation measures revealed that the best matching mineral is goethite, with a spectral angle of 0.075 and a correlation of 0.997. Generally it is considered to be a good match when the spectral angle is smaller than 0.1 or the correlation is greater than 0.9. Goethite is relatively stable and suggests a moderate acid environment. Em5 is also best matched with goethite but with a smaller correlation (0.982) and a larger spectral angle (0.112). The variations between em10 and em5 could occur for three reasons. First, it could imply the emergence of another mineral. Second, it could be caused by different grain sizes in the sediments. When the stream reaches the pond, the velocity of the flow slows down which promotes the deposition of sediments with larger grain size. Third, water attenuation could also play an important role. However, no clear explanation in the existing literature has indicated the effect of water in reflectance of a specific mixture as such. The spectrum of em8 does not match well with any mineral in the spectral library. This could be because em8 is a mixture of two or more minerals with no one mineral occurring in a dominant proportion. Because spectra in the spectral library are derived from pure samples, no match can be found. Overall, this experiment revealed the potential of *casi* to provide information on mine tailing extent and permit separation of tailings with varying composition and oxidation levels.

Ground Measurements: Spectral matching results of the 21 GER spectra of the tailings samples are shown in Table 1. Candidate minerals were accepted if the matching met two criteria: the spectral angle is smaller than 0.1 and the correlation is greater than 0.9. Since the spectra from the USGS spectral library are derived from pure mineral samples, a good match can only be achieved when a single mineral dominates the sample. If two or more minerals with equal or similar proportions exist in one sample, the spectrum of the sample will be the combined effects of all the contributing minerals. The resulting spectrum may not match with any of the minerals in the library. In the worst case, the mixed spectrum may produce a match with a known spectrum for a mineral that is not relevant to the study area.

Table 1. Candidate Minerals for the Tailings Samples Derived from Spectral Matching with the USGS Spectral Library.

Tailing Sample #	Candidate Minerals	Spectral Angle	Correlation
1	phlogopite	0.078	0.989
2	goethite	0.112	0.989
3	andradite andisine	0.067 0.070	0.985 0.967
4	pyrrhotite andradite	0.087 0.089	0.960 0.956
5	pyrite	0.037	0.987
6	jarosite	0.133	0.959
7	jarosite	0.072	0.985
8	no match	0.071	0.949
9	andradite jarosite	0.085 0.010	0.982 0.979
10	andradite corrensite	0.049 0.085	0.993 0.987
11a	jarosite	0.08	0.982
11b	jarosite pyrrhotite	0.057 0.096	0.986 0.985
12	jarosite	0.106	0.968
13	phlogopite	0.081	0.970
14	prochlorite amphibole	0.049 0.049	0.986 0.984
15	andradite jarosite	0.089 0.092	0.978 0.978
16	jarosite	0.051	0.989
17	pyrrhotite	0.063	0.987
18	jarosite pyrrhotite	0.056 0.094	0.987 0.985
19	jarosite andradite	0.072 0.093	0.980 0.972
20	pyrrhotite andradite jarosite	0.054 0.064 0.072	0.991 0.981 0.991

Table 1 reveals that the most frequently occurring oxidized minerals in the study site are jarosite ($NaFe^{+3}{}_3(SO_4)_2(OH)_6$, $KFe^{+3}{}_3(SO_4)_2(OH)_6$) and goethite (alpha-$Fe^{+}O(OH)$). These mineral matches make sense since the aforementioned minerals are the ones most likely to appear in tailings areas, especially metal mine tailings.

Tailings samples 4 and 5 also make perfect sense. Sample 4 was collected from the known pyrrhotite tailings site in the R4 area and is best matched to pyrrhotite. Sample 5 consists of fresh tailings prior to any oxidation. Therefore, it shows the property of the original ore-rock composition, pyrite. As an example, four spectral matching pairs are depicted in Figure 7. Pyrite and pyrrhotite were chosen to show the original unoxidized tailings. Jarosite and goethite were chosen to show oxidized tailings. According to the study by Swayze *et al.* (1998), with progressive oxidation pyrite weathers first to jarosite, and then to goethite. The spatial distribution of jarosite and goethite therefore provide a means whereby it is possible to identify areas associated with low pH and heavy metal. Jarosite is associated with the initial stage of the oxidation during which a strong-acid environment is present. It usually coexists with more leachable heavy metals. Goethite, a more stable mineral, is formed in a less-acid environment and is associated with lower concentrations of leachable heavy metals.

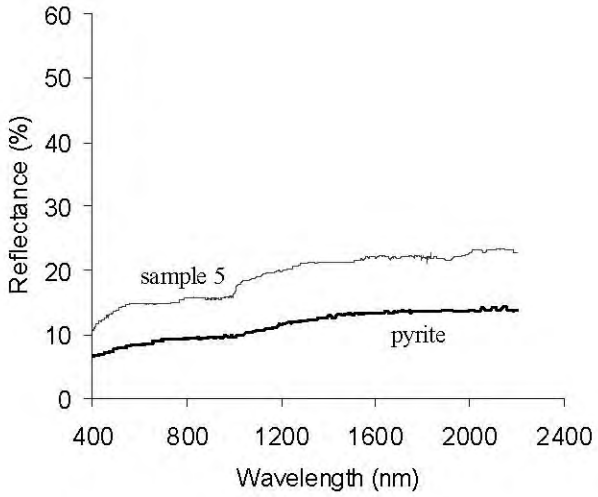

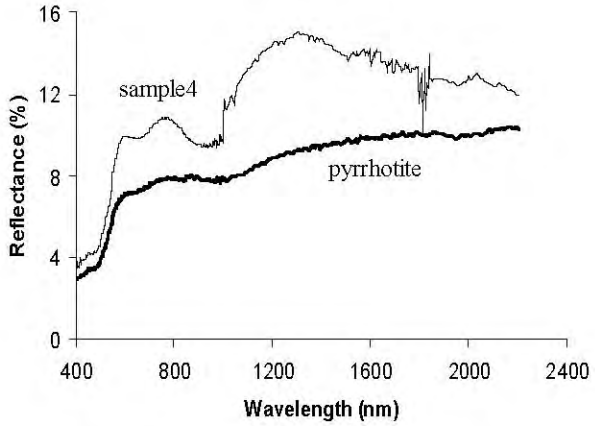

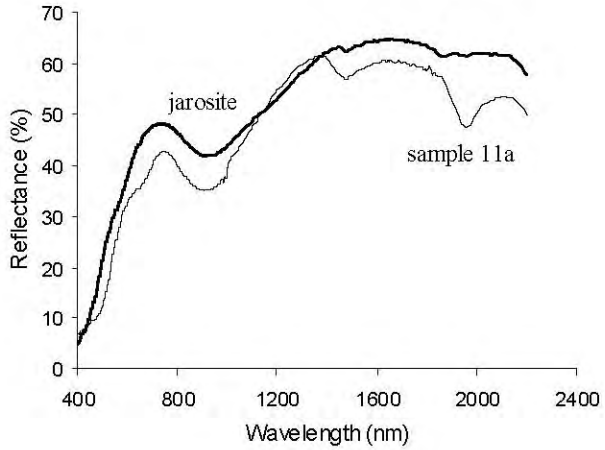

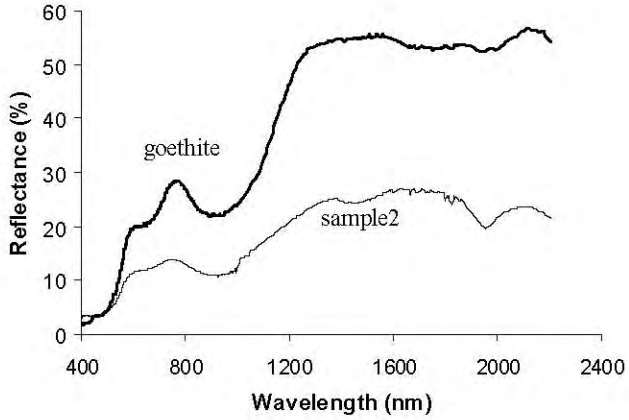

Figure 7. Selected GER spectra and the corresponding matching spectra from the USGS spectral library

It can be seen that differences exist between the sample spectra and the library spectra, even for the best-matched spectral pairs shown in Figure 7. This could be caused by the real difference between the samples and the library minerals. As mentioned earlier, the library spectra were derived from pure mineral samples. In contrast, the tailing samples are more likely mixtures of a variety of minerals. When the proportions of the minor minerals reach a certain level, the spectral shape of the sample will alter and start to resemble the absorption features of the minor minerals.

Spectral matching of the *casi* image spectra revealed mineral results similar to the laboratory-acquired GER spectra. Sample 4 is also best matched with pyrrhotite. Samples 7, 11a, 11b, and 20 also show the same results as the GER. This suggests that *casi* data have the potential for providing information on variations of the oxidation of tailings. As an example, two spectral matching pairs of *casi* spectra are shown in Figure 8.

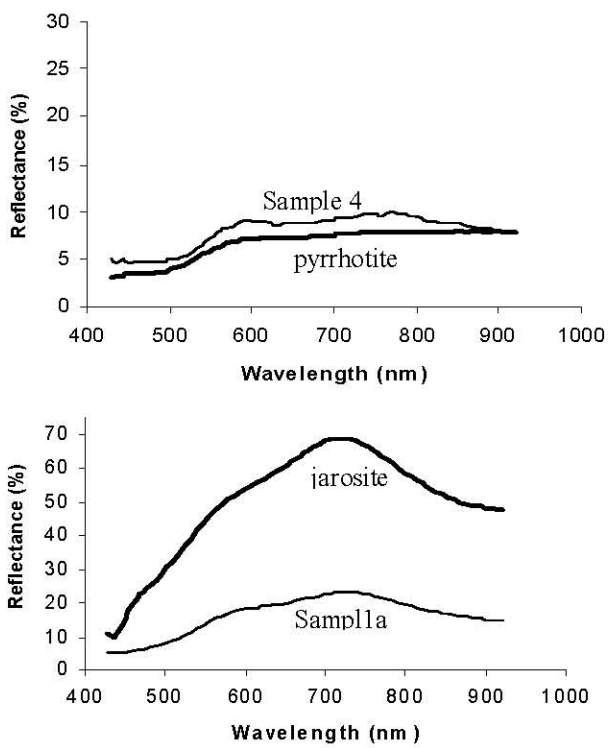

Figure 8. Selected casi spectra and the corresponding matching spectra from the USGS spectral library.

Given the fairly good alignment between the spectral matching results of the same tailing samples from the GER and *casi*, there are some disagreements. This is due to three causes. First, some subtle yet vital absorption features may exist only in the shortwave infrared region of the spectrum which *casi* does not cover. Second, the spectrum of a single pixel represents the averaged information of a broad area, approximately 4 m x 4 m. However, the GER samples very small areas, for this study 20 cm^2. Therefore inherent differences may exist between the tailings being measured. Third, co-location of the sample sites can also contribute to the disagreement. Even though the image spectra were picked visually from the *casi* imagery at the same locations as where the tailing samples, the visual judgement could be off by several pixels.

Conclusions

This study has demonstrated that *casi* data can be used to provide information on separating the oxidation zonations of the tailings. Spectral matching revealed that the most likely existing minerals on this tailings site are pyrite pyrrhotite, jarosite, and goethite. Despite of *casi*'s limited spectral coverage, similar results were found as from the GER spectral matching. Unfortunately, no direct relationships were found between the oxidation phases and the age of the tailings. A more detailed study will be performed in the future on the entire tailings site. Hopefully, it will reveal information on the spatial distribution of oxidized minerals at various phases to provide a better understanding of the evolution of tailings over time.

Acknowledgement

Financial support for this project was provided by the Centre for Research in Earth and Space Technology (CRESTech). The *casi* dataset was acquired by CRESTech. The ISDAS software was provided by the Canada Centre for Remote Sensing (CCRS). Special thanks to Alan King at Inco for his support in this project. Thanks also

goes to the following individuals for their insights and support through the data processing and writing of this paper: David Blowes of the University of Waterloo, Jean-Claude Deguise, Christian Nadeau, Robert Neville and Jeff Secker of CCRS.

References

Ash, S. H., Felegy, E. W., Kennedy, D. O., and Miller, P. S. (1951). *Acid mine drainage problems-Anthracite region of Pennsylvania*, U.S. Bureau of Mines Bulletin 508, 72 pages.

Boine, J., Olbert, C., Glaber, C. and Fischer, J. (1999). "Preliminary spectral investigations of lignite open cast residual lakes in Central Germany." *Proceedings (CD) of 3rd German-Dutch Symposium on Environmental Assessment and Monitoring, 28-29 April,* Germany, 1999.

Farrand, W. H. and Harsanyi, C. (1997. "Mapping of mine tailings in the Coeur d'Alene River valley, Idaho, through the use of constrained energy minimization technique". *Remote Sensing of Environment*, Vol. 59, pp.64-76.

Lévesque, J., Staenz, K., Singhroy, V. and Bolton, D. (1997). "Spectral Unmixing for Monitoring Mine Tailings Site Rehabilitation, Copper Cliff Mine, Sudbury, Ontario." *Proceedings of the 12th International Conference and Workshops on Applied Geological Remote Sensing,* 17-19 November, Denvor, Colorado, U.S.A.

Nordstrom, D. K. and Apers, C. N. (1999). "Geochemistry of acid mine waters", (Chapter 6) in *The Environmental Geochemistry of Mineral Deposits, Part A: Processes, Techniques, and Health Issues* (volume editors: Geoffrey S. Plumlee and Mark J. Logsdon). Littleton, Colorado, Society of Economic Geologists, pp. 133-160.

Pearson, R. M., Swayze, G. A., Wiltshire, R., Serina, D. and Clark, R. N. (1997). "Using AVIRIS imagery mineral mapping for identification of acid rock drainage sources at the California Gulch NPL site and fluvial tailings deposits on the Arkansas River, Leadville, Colorado, USA." *Proceedings of the 3rd International Airborne Remote Sensing Conference and Exhibition*, 7-10 July, Copenhagen, Denmark, Vol. I, pp. 102-109.

Puro, M. J., Kipkie, W. B., Knapp, R. A., McDonald, T. J. and Stuparyk, R. A. (1995), "Inco's Copper Cliff Tailings Area." *Proceedings of the Sudbury'95 Conference on Mining and the Environment*, Sudbury, Ontario, Canada, Vol. 1, pp. 181-191.

Shang, J., Lévesque, J., Howarth, P., Morris, B., Staenz, K. and Yearwood, P. (1999). "Preliminary Investigation of Acid Mine Drainage Detection Using casi Data, Copper Cliff, Ontario, Canada." *Proceedings of the Fourth International Airborne Remote Sensing conference and Exhibition/21st Canadian Symposium on Remote Sensing*, Ottawa, Ontario, Canada. Vol. 1, pp. 771-778.

Staenz, K., Szeredi, T. and Schwarz, J. (1998). "ISDAS - A System for Processing/Analyzing Hyperspectral Data." *Canadian Journal of Remote Sensing*, Vol. 24, No. 2, pp. 99-113.

Staenz, K. and Williams, D. J. (1997) "Retrieval of Surface Reflectance from Hyperspectral Data Using a Look-Up Table Approach." *Canadian Journal of Remote Sensing*, Vol. 23, No. 4, pp. 354-368.

Swayze, G. A., Clark, R.N., Smith, K. S., Hageman, P. L., Sutley, S. J., Pearson, R. M., Rust, G. S., Briggs, P. H., Meier, A. L., Singleton, M. J. and Shelly, R. (1998). "Usig imaging spectroscopy to cost-effectively locate acid-generating minerals at mine sites: an example from the California Gulch Superfund Site in Leadville, Colorado." *Jet Propulsion Laboratory Publicstion*, 97-21, 1, pp. 385-389.

Swayze, G.A., Smith, K.S., Clark, R.N., Sutley, S.J., Pearson, R.M., Vance, J.S., Hageman, P.L., Briggs, P.H., Meier, A.L., Singleton, M.J. and Roth, S. (2000). "Using imaging spectroscopy to

map acidic mine waste." *Environ Sci Technol.*, Vol. 34, 47-54.

Szeredi, T., Staenz, K. and Neville R. A. (2000). "Automatic endmember selection: part I theory." Submitted to *Remote Sensing of Environment.*

USGS (2000). Digital Spectral Library. Website address:http://speclab.cr.usgs.gov/spectral.lib04/spectral-lib04.html.

Walton-Day, K. (1999) "Geochemistry of the processes that attenuate acid mine drainage in wetlands." *The Environmental Geochemistry of Mineral Deposits, Part A: Processes, Techniques, and Health Issues.* Society of Economic Geologists, Inc., pp. 215-228.

Preprint/Prétirage

PRELIMINARY INVESTIGATION OF ACID MINE DRAINAGE DETECTION USING *casi* DATA, COPPER CLIFF, ONTARIO, CANADA*

Jiali Shang[1], Josée Lévesque[2], Philip Howarth[1], Bill Morris[3], Karl Staenz[4], Paul Yearwood[5]

[1]Waterloo Laboratory for Earth Observations, Department of Geography, University of Waterloo Waterloo, Ontario, Canada N2L 3G1 e-mail: j2shang@fes.uwaterloo.ca

[2]MIR Télédétection Inc., 2182 de la Province, Longueuil, Québec, Canada J4G 1R7

[3]School of Geography and Geology, McMaster University, Hamilton, Ontario, Canada L8S 4M1

[4]Canada Centre for Remote Sensing, 588 Booth Street, Ottawa, Ontario, Canada K1A 0Y7

[5]Decommissioning and Reclamation, Inco Limited, Copper Cliff, Ontario, Canada P0M 1N0

ABSTRACT

The environmental impact of mine tailings is a nation-wide problem in Canada. Mine tailings affect the environment primarily through acid mine drainage (AMD). AMD contains toxic concentrations of metals and dissolved salts which can contaminate ground and surface water. There is a clear need for monitoring mine-tailing sites in order to ensure that damage to the environment is kept to a minimum. The availability of high spatial resolution hyperspectral airborne imagery, acquired by sensors such as the Compact Airborne Spectrographic Imager (*casi*), has greatly improved the potential for automated mapping of mine tailings. In this paper, we investigate the potential of *casi* data for use in AMD detection. Both constrained and unconstrained linear spectral unmixing was performed on summer 1998 *casi* data acquired over the Copper Cliff tailings area in Ontario, Canada. Preliminary results show that spectral unmixing of *casi* data can provide valuable information on the occurrence of AMD.

1.0 INTRODUCTION

Tailings are the waste products of mineral processing from mining operations. The negative effects of mine tailings include the loss of land-surface values, soil erosion, and air and water pollution. The environmental impact of mine tailings is a nation-wide problem in Canada. Up to 1994, there were 41,000 hectares (410 km^2) of mine tailings in Canada (CANMET, 1994). The increasing demand for metals and the ability to develop lower-grade ores economically in the future could lead to further accumulation of acidic tailings. Tailings from copper (Cu), zinc (Zn), nickel (Ni), gold (Au), and uranium (U) mines contain sulphide minerals. When tailings are in contact with oxygen and water, these sulphide minerals will oxidize and generate acid (Lévesque *et al.*, 1997a; MEND, 1999). Acid-mine drainage (AMD) will dissolve the residue metals in the tailings thus causing ground- and surface-water contamination. These dissolved metals and low pH conditions can have detrimental effects on the health of plants and animals.

* Presented at the Fourth International Airborne Remote Sensing Conference and Exhibition / 21st Canadian Symposium on Remote Sensing, Ottawa, Ontario, Canada, 21-24 June 1999.

There is a clear need for monitoring mine-tailing sites in order to ensure that damage to the environment is kept to a minimum. Mapping the extent of mine tailings and their change over time is an essential component of mine-tailing monitoring and inventory. Various remote sensing data have been used for this purpose. However, because of the relatively coarse spatial and spectral resolutions of traditional satellite data, it is difficult to identify and map complex surfaces such as mine tailings. The availability of high spatial resolution hyperspectral airborne imagery, acquired by sensors such as the Compact Airborne Spectrographic Imager (*casi*), has greatly improved the potential for automated mapping of mine tailings. In this paper, the use of *casi* data for AMD detection is investigated through a case study at the Inco Copper Cliff mine, Ontario, Canada.

2.0 STUDY SITE

The study site is located at Inco Limited's Copper Cliff tailings area, Ontario, Canada (Figure 1). This site was selected because it has the largest acid-generating tailings in Canada, approximately 5,500 acres (22.3 km^2) (Puro *et al.*, 1995). It contains a range of mine-tailing lithologies with different levels of vegetation regrowth. The major surface-cover types are fresh tailings, oxidized tailings, tailings-retention ponds, lime, and vegetation. This area has been experiencing extensive revegetation activities. To date, 838 hectares of tailings have been limed, fertilized and seeded, and 340 hectares are permanently covered with water in the form of containment ponds (Yearwood, 1998). In addition, a considerable amount of research has been undertaken over this area which provides valuable information on the site (De Vos, 1995; Lévesque *et al.*, 1997a, 1997b, and 1999; McGregor, 1998). Results of these previous studies will assist in image interpretation.

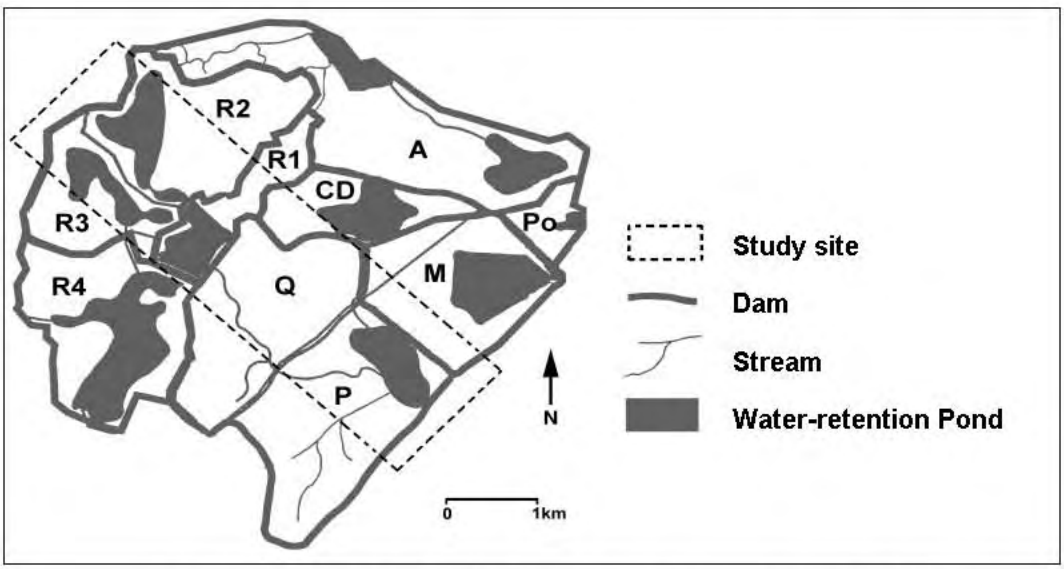

Figure 1. Map of the Study Area (Modified from Puro *et al.*, 1995)

3.0 DATA ACQUISITION AND PREPROCESSING

High spatial and spectral resolution *casi* data were acquired in spectral mode over the study area at 14:45 p.m. on August 19, 1998. The sky condition was clear, and the aircraft was flying at 2100 m above sea level (approximately 1800 m above the ground) heading 130 degrees from north. The data cover the visible and near-infrared regions of the electromagnetic spectrum, from 407 to 944 nm, in 72 contiguous bands. The bandwidth at FWHM (full width at half maximum) is 10 nm with a spectral sampling interval of 10 nm. The spatial resolution is 4 m by 4 m, resulting in a swath width of 1.6 km (406 pixels).

Image preprocessing was performed prior to image analysis to convert the *casi* radiance data to reflectance data. The preprocessing steps include roll correction, reflectance retrieval, and post-processing of the data in the spectral domain. In the first step, the *casi* data were corrected for aircraft roll effects by calculating lateral pixel shifts for each line using the navigation data. However, the *casi* data were not corrected for pitch and yaw due to the lack of navigation data. The *casi* radiance data were then converted to reflectance data using the Imaging Spectrometer Data Analysis System's (ISDAS) surface reflectance retrieval procedure (Staenz *et al.*, 1998). This procedure, developed by Staenz and Williams (1997), is based on a look-up table (LUT) approach to remove atmospheric effects from the *casi* data. It takes into account the wavelength, pixel position, atmospheric water vapour, aerosol optical depth, and terrain elevation for the generation of the LUT. MODTRAN3 radiative transfer (RT) code was used to create the LUT. The parameters used to run the MODTRAN3 RT code are listed in Table 1.

Table 1. Input Parameters for the MODTRAN3 Run

Parameters	**Input**
Standard atmospheric model	Mid-latitude summer
Aerosol model	Continental (rural)
Date of overflight	August 19, 1998
Solar zenith angle	50.6 °
Solar azimuth angle	116.9 °
Sensor zenith angle	Variable
Sensor azimuth angle	Variable
Sensor altitude above sea level	2000 m
Platform heading	130°
Terrain elevation	300 m
Water-vapour content	1.2 g/cm^2
Horizontal visibility	50 km

Post-processing was then performed on the retrieved reflectance data using spectrally flat targets to remove artifacts due to calibration and atmospheric modeling (Staenz *et al.*, 1998). Subscenes from two adjacent flightlines (6 and 7) of the *casi* surface reflectance images are shown in Figure 2. The areas labeled will be reviewed in detail in Section 5.0 Results and Discussion.

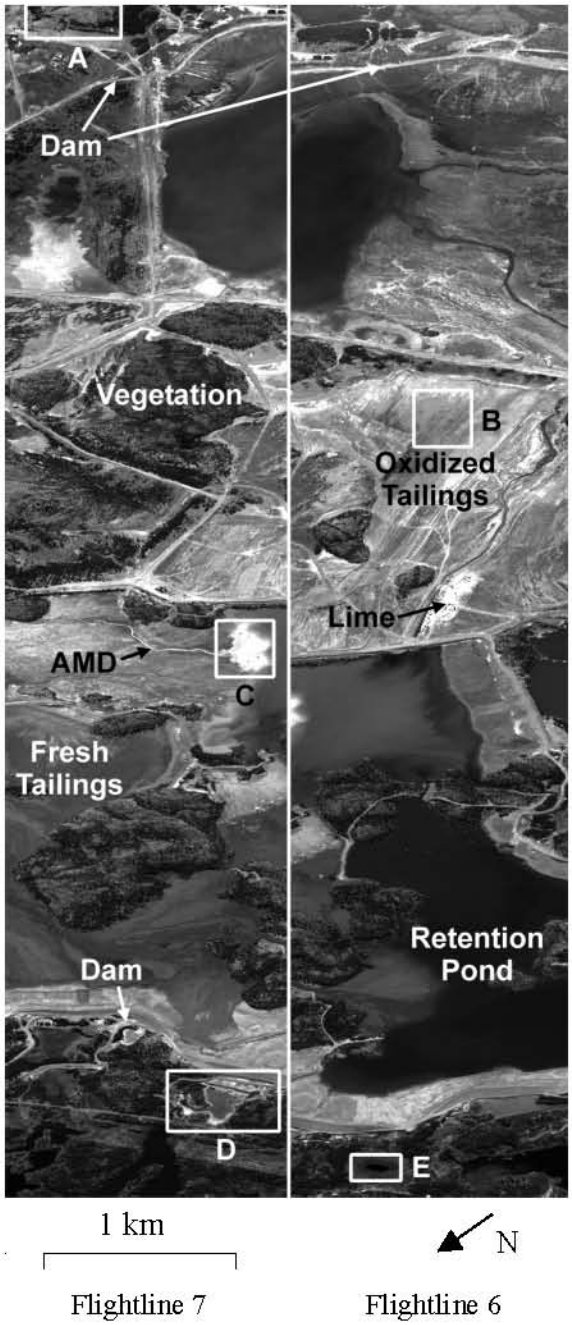

Figure 2. *casi* Reflectance Images of the Study Site (band 35 centered at wavelength 661 nm)

4.0 METHODS

The study is intended to investigate the potential of *casi* data for detecting AMD. This issue is addressed by comparing the fraction maps with the ground survey results.

Spectral unmixing was performed on the sub-scenes (flightlines 6 and 7) of the *casi* reflectance data in ISDAS. Both constrained and unconstrained linear-unmixing algorithms were applied. Linear unmixing is based on the assumption that the reflectance of a given target is the additive combination of the reflectance of each of the target components (endmembers) (Mustard and Pieters, 1987; Ben-Dor and Kruse 1995; Tompkins *et al.*, 1997). The unconstrained unmixing is abundance-free, and it can take on any value. Therefore, it represents the relative abundance of endmembers. The constrained unmixing provides the absolute abundance (Boardman, 1990).

Five endmembers were chosen for unmixing: water1, water2, oxidized tailings, lime, and vegetation. These endmember spectra were selected from the *casi* reflectance data. A principal component transformation was then conducted on all 72 bands of the *casi* reflectance data. The first three principal components (PCs) account for 98.8% of the total scene variance. These three PCs were used for selecting the endmembers. Endmembers are located at the extremities of the clouds of scatterplots using two of the PCs (Boardman, 1995; Lévesque *et al.*, 1999).

The locations of the five endmembers are shown in Figure 3. The spectra of the corresponding endmembers extracted from the *casi* data are shown in Figure 4.

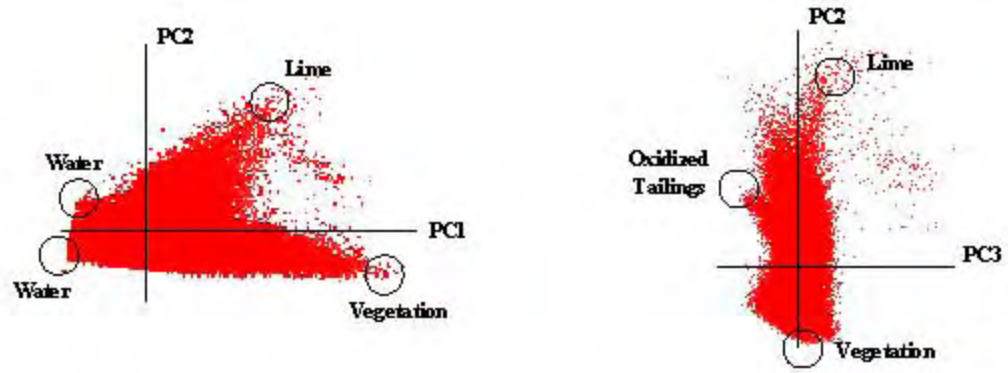

Figure 3. The Location of Endmembers on Scatter Plots of PC1 versus PC2 (left) and PC2 versus PC3 (right)

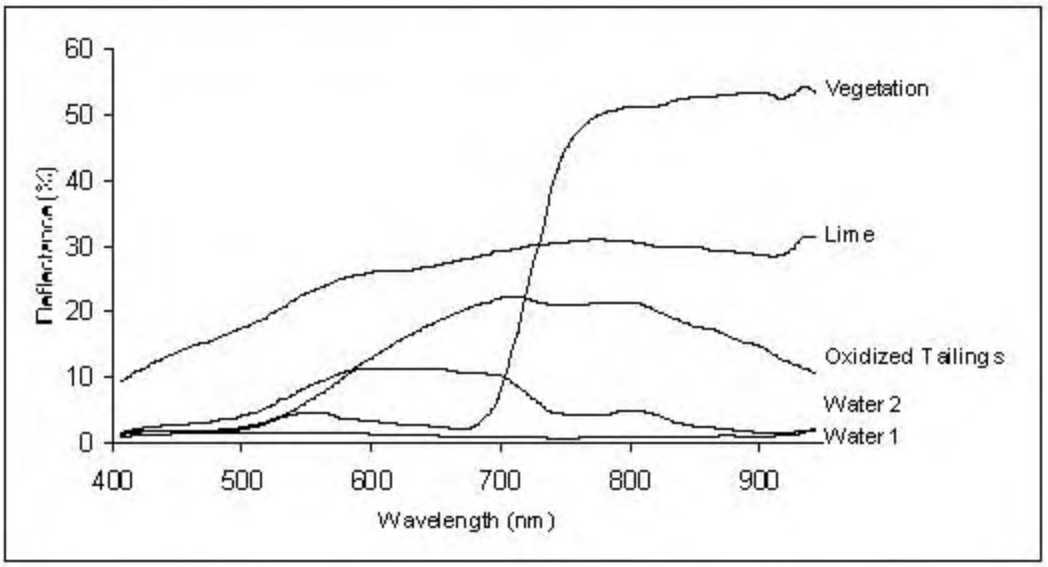

Figure 4. Endmember Spectra Derived from the *casi* Imagery

5.0 RESULTS AND DISCUSSION

A fraction map for each of the endmembers was generated. Results derived from the constrained and unconstrained linear unmixing were compared visually. Overall, the constrained model produced more realistic fraction maps based on a comparison with ground inspections. More detailed verification will be conducted in the future. Among these maps, the ones showing oxidized-tailing fractions are of most interest; they are displayed in Figure 5. The fraction maps have been enhanced using linear contrast stretch for better visualization. Bright tones represent high fractions, and dark tones represent low fractions. Five areas labeled A, B, C, D, and E in Figure 5 (see also Figure 2) will be discussed in detail. These areas represent typical portions of the tailings and their surroundings.

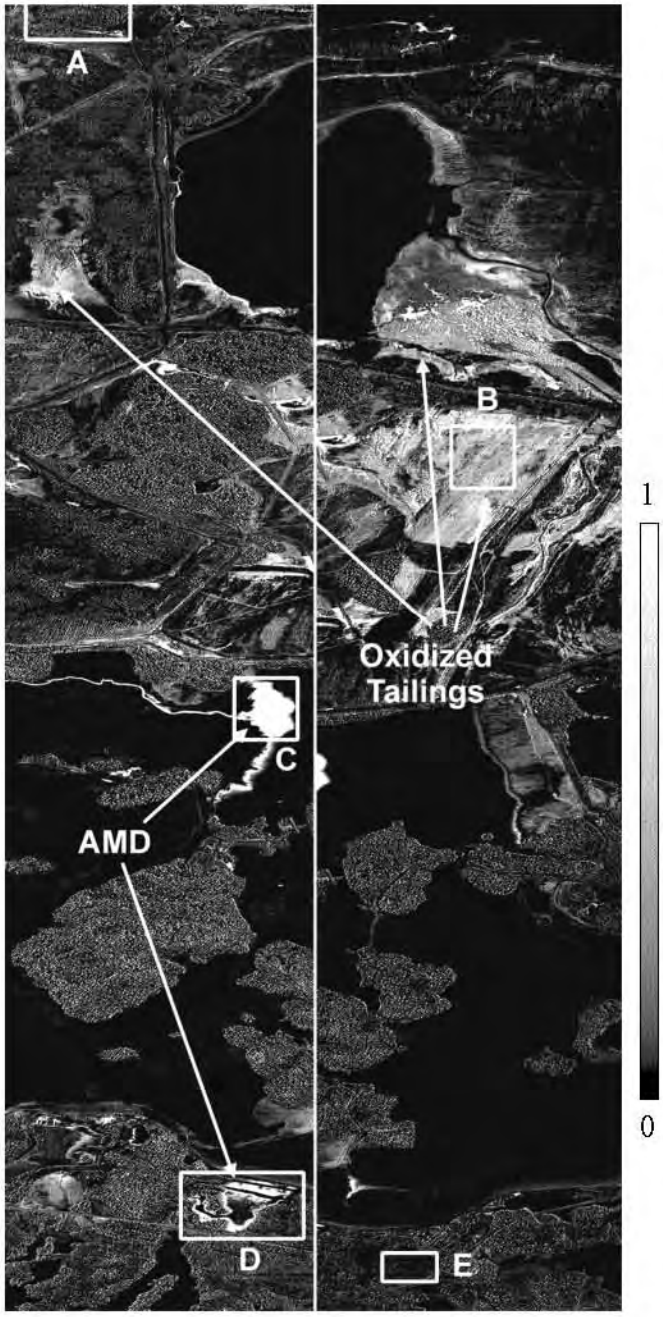

Flightline 7 Flightline 6

Figure 5. Oxidized Tailing (AMD) Fraction Map

Area A represents a rock outcrop with some vegetation cover. It is located beyond the tailings confinement area, southeast of the P tailings (Figure 1). On the map in Figure 5, the fractions are shown in mottled grey tones, with values between 0.0 and 0.2. They reveal the existence of oxidized tailings in this area. Since the prevailing wind in the area is from the northwest, the wind carries dust from the bare tailings and deposits it on the surface of the rock outcrop.

The bare oxidized tailings (Area B) are also well-defined. These areas have been limed, with no vegetation cover. In the fraction maps, they show as light tone with smooth texture.

Area C represents an extreme of AMD causing the tailings to appear in a rusty colour. It displays in solid bright tones in Figure 5 with fraction values of 0.7 to 1.0.

Area D is a tailings water-collection pond, located northwest to the dam that confines R2 and R3 tailings (Figure 1). It is also shown as bright tones due to its association with tailings water. However, its fractional values vary between 0.3 and 0.5, lower than area C.

Area E is a native water-body close to the R3 dam. There is no sign of AMD contamination or leaching from underneath the dam. Accordingly, the fractional values are close to zero. However, we do see some mottled grey tones in its neighborhood. This is very likely caused by airborne pollution.

6.0 CONCLUSIONS

This preliminary investigation has revealed that *casi* data can be used to detect acid mine drainage. It is a common belief that image data covering only the visible and near-infrared wavelengths are not capable of detecting mineral composition. This is because of the strong absorption features of minerals occurring in the shortwave-infrared region of the electromagnetic spectrum. However, due to the association of oxidized tailings with iron oxides, the occurrence of AMD can be inferred using iron oxide as an indicator. Iron oxides are featured as various shades of yellow, red, and brown colours in rocks, soils, and water (Schwertmann and Cornell, 1991). They can be identified using the visible and near-infrared portions of the spectrum as covered by the *casi* data used for this investigation (Kruse *et al.*, 1991). This study shows that *casi* can be used to recognize qualitatively the occurrence of AMD. For a future study, we will look at the relationship between oxidized tailings (AMD) and the *casi* response in a quantitative manner.

The results of this study will assist mining companies in monitoring the migration of AMD. By identifying possible affected sites, a more detailed survey can be conducted targeting these key areas in order to reduce time and cost. Accordingly, proper control can be applied to mitigate the negative impact of mine tailings on the surrounding environment.

7.0 ACKNOWLEDGEMENTS

Funding for this project was provided by the Centre for Research in Earth and Space Technology (CRESTech). The *casi* dataset was acquired by CRESTech. The Canada Centre for Remote Sensing (CCRS) provided both computer and image-processing software for data analysis. Special thanks to Dr. Alan King at Inco for his support in this project. Insights provided by Dr. David Blowes of the University of Waterloo are much appreciated.

8.0 REFERENCES

Ben-Dor, E. and Kruse, F. A., "Surface Mineral Mapping of Makhtesh Ramon Negev, Israel Using GER 63 Channel Scanner Data." *International Journal of Remote Sensing*, Vol. 16, No. 18, pp. 3529 – 3553, 1995.

Boardman, J. W., "Inversion of High Spectral Resolution Data." *Proceedings of the International SPIE Conference on Imaging Spectroscopy of the Terrestrial Environment,* Vol. 1298, pp. 223-233, 1990.

Boardman, J. W., "Analysis, Understanding and Visualization of Hyperspectral Data as Convex Sets in N-Space." *Proceedings of the International SPIE Conference on Imaging Spectroscopy of the Terrestrial Environment,* Vol.2480, pp.14-21, 1995.

CANMET, Report of Results of a Workshop on Mine Reclamation, 1994.

De Vos, K., *Geochemistry and Hydrogeology of a Plum of Tailings-Derived Water, Copper Cliff, Ontario,* University of Waterloo, unpublished M. Sc. Thesis, 1995.

Kruse, F. A., Dietz, J. B., and Kierein-Young, K. S., "Geological Mapping in Death Valley, California/Nevada Using NASA/JPL Airborne Systems (AVIRIS, TIMS, and AIRSAR)." *Proceedings of the Third AVIRIS Workshop*, U.S.A., *JPL* 91-28, pp. 258-259, 1991.

Lévesque, J., Singhroy, V., Staenz, K., and Bolton, D., "Site Characterization of Mine Tailings at the INCO Copper Cliff Tailings Impoundment Area Using *casi* Imagery." *Proceedings of GER '97, Geomatics Canada* (on CD-ROM), Canada, 1997a.

Lévesque, J., Staenz, K., Shighroy, V., and Bolton, D., "Spectral Unmixing for Monitoring Mine Tailings Site Rehabilitation, Copper Cliff Mine, Sudbury, Ontario." *Proceedings of the 12th International Conference and Workshops on Applied Geological Remote Sensing,* U.S.A., 1997b.

Lévesque, J., Staenz, K., Shang, J., Yearwood, P., Shighroy, V., "Temporal Monitoring of Mine Tailings Revegetation Using Hyperspectral Data, Sudbury, Ontario." *Proceedings of the Thirteenth International Conference on Applied Geologic Remote Sensing*, Canada, 1-3 March, Vol. II, pp. 21-28, 1999.

McGregor, R.G., Blowes, D.W., Jambor, J.L. and Robertson, W. D., "The Solid-Phase Controls on the Mobility of Heavy Metals at the Copper Cliff Tailings Area, Sudbury, Ontario Canada." *Journal of Contaminant Hydrology*, Vol. 33, pp. 247-271, 1998.

MEND, "Mine Environmental Neutral Drainage Program," website: http://www.nrcan.gc.ca/mets/mend, 1999.

Mustard, J. F. and Pieters, C. M., "Abundance and Distribution of Ultramafic Microbreccia in Moses Rock Dike: Quantitative Application of Mapping Spectroscopy." *Journal of Geophysical Research,* Vol. 92, pp. 10376-10390, 1987.

Puro, M. J., Kipkie, W. B., Knapp, R. A., McDonald, T. J., and Stuparyk, R. A., "Inco's Copper Cliff Tailings Area." *Proceedings of the Sudbury'95 Conference on Mining and the Environment*, Canada, Vol. 1, pp. 181-191, 1995.

Schwertmann, U. and Cornell, R. M., *Iron Oxides in the Laboratory: Preparation and Characterization.* VCH, Weinheim, Germany, 137p., 1991.

Staenz, K., Szeredi, T. and Schwarz, J., "ISDAS - A System for Processing/Analyzing Hyperspectral Data." *Canadian Journal of Remote Sensing*, Vol. 24, No. 2, pp. 99-113, 1998.

Staenz, K. and Williams, D. J., "Retrieval of Surface Reflectance from Hyperspectral Data Using a Look-Up Table Approach." *Canadian Journal of Remote Sensing*, Vol. 23, No. 4, pp. 354-368, 1997.

Tompkins, S., Mustard, J. F., Pieters, C. M. and Forsyth, D. W., "Optimization of Endmembers for Spectral Mixture Analysis." *Remote Sensing of Environment*, Vol. 59, pp. 472-489, 1997.

Yearwood, P., Unpublished Departmental Record of Decommissioning and Reclamation, Inco Limited, 1998.

Vegetation Stress Detection through Chlorophyll $a + b$ Estimation and Fluorescence Effects on Hyperspectral Imagery

P. J. Zarco-Tejada,* J. R. Miller, G. H. Mohammed, T. L. Noland, and P. H. Sampson

ABSTRACT

Physical principles applied to remote sensing data are key to successfully quantifying vegetation physiological condition from the study of the light interaction with the canopy under observation. We used the fluorescence–reflectance–transmittance (FRT) and PROSPECT leaf models to simulate reflectance as a function of leaf biochemical and fluorescence variables. A series of laboratory measurements of spectral reflectance at leaf and canopy levels and a modeling study were conducted, demonstrating that effects of chlorophyll fluorescence (CF) can be detected by remote sensing. The coupled FRT and PROSPECT model enabled CF and chlorophyll $a + b$ (C_{a+b}) content to be estimated by inversion. Laboratory measurements of leaf reflectance (r) and transmittance (t) from leaves with constant C_{a+b} allowed the study of CF effects on specific fluorescence-sensitive indices calculated in the Photosystem I (PS-I) and Photosystem II (PS-II) optical region, such as the curvature index [CUR; $(R_{675}\cdot R_{690})/R^2_{683}$]. Dark-adapted and steady-state fluorescence measurements, such as the ratio of variable to maximal fluorescence (F_v/F_m), steady state maximal fluorescence (F'_m), steady state fluorescence (F_s), and the effective quantum yield ($\Delta F/F'_m$) are accurately estimated by inverting the FRT–PROSPECT model. A double peak in the derivative reflectance (DR) was related to increased CF and C_{a+b} concentration. These results were consistent with imagery collected with a compact airborne spectrographic imager (CASI) sensor from sites of sugar maple (*Acer saccharum* Marshall) of high and low stress conditions, showing a double peak on canopy derivative reflectance in the red-edge spectral region. We developed a derivative chlorophyll index (DCI; calculated as D_{705}/D_{722}), a function of the combined effects of CF and C_{a+b} content, and used it to detect vegetation stress.

Most current assessments of forest condition are limited to ground-based visual evaluation (e.g., Canadian Forest Service, 1999). Although these conventional field assessments are valuable, they do not reveal physiological changes that characterize early stress responses (Sampson et al., 2000). Assessing physiological condition can indicate productivity and adaptability to environmental stress (Chapin, 1991; Colombo and Parker, 1999) and may provide early indication of decline in stand vigor and productive capacity. Early detection of stress with remote sensing methods could help to identify stress status at larger temporal and spatial scales and before damage is visible. However, to determine vegetation condition from the study of the interaction between the light and the canopy under observation, physical methods must be developed (Zarco-Tejada, 2000).

The C_{a+b} content is a potential indicator of vegetation stress because of its direct role in the photosynthetic processes of light harvesting and initiation of electron transport and its responsiveness to a range of stresses. In the chloroplast, light energy is harvested and processed by two functional units designated Photosystem I (containing chlorophyll with an absorption peak at 700 nm) and Photosystem II (chlorophyll absorption peak at 680 nm), which produce oxygen and energy through a series of reduction–oxidation reactions to transport electrons. Stressed vegetation can undergo various physiological perturbations in the light-dependent reactions of photosynthesis, including disruption of electron transfer, production of deleterious oxygen derivatives, photobleaching, pigment-bed reorganization, and structural damage to photosynthetic pigments. Differences in remote sensing reflectance between healthy and stressed vegetation due to changes in C_{a+b} levels have been detected previously in the green peak and along the red-edge spectral region (690 to 750 nm) (e.g., Rock et al., 1988; Vogelmann et al., 1993; Carter, 1994; Gitelson and Merzlyak, 1996).

Assessing CF is also a well-established physiological approach to detect previsual strain (Mohammed et al., 1995). Changes in chlorophyll function often precede changes in chlorophyll content, hence CF changes are often observed long before leaves become chlorotic. Chlorophyll fluorescence is red and far-red light produced in photosynthetic tissues upon excitation with natural or artificial light in the visible spectrum. Chlorophyll fluorescence production is one way plant chloroplasts harmlessly dissipate light energy that exceeds photosynthesis requirements, thereby protecting the chloroplasts from light-induced oxidative damage. According to several reviews of CF theory, measurement methods and interpretation (e.g., Papageorgiou, 1975; Krause and Weis, 1984; Schreiber and Bilger, 1987; Lichtenthaler and Rinderle, 1988; Lichtenthaler, 1992; Larcher, 1994; Schreiber et al., 1994), steady state CF and photosynthetic rate are inversely related (i.e., CF is low when photosynthesis is high). In addition, CF techniques

P.J. Zarco-Tejada, Centre for Research in Earth and Space Science (CRESS), and J.R. Miller, Dep. of Physics and Astronomy, York University, 4700 Keele Street, Toronto, ON, Canada M3J 1P3. G.H. Mohammed, P&M Technologies, 66 Millwood St., Sault Ste. Marie, ON, Canada P6A 6S7. T.L. Noland, Ontario Forest Research Institute (OFRI), Ontario Ministry of Natural Resources (OMNR), Sault Ste. Marie, ON, Canada P6A 2E5. P.H. Sampson, Provincial Geomatics Service Centre, Ontario Ministry of Natural Resources, 300 Water St, Peterborough, ON, Canada K9J 8M5. Received 24 Jan. 2001. *Corresponding author (zarco@terra.phys.yorku.ca).

Published in J. Environ. Qual. 31:1433–1441 (2002).

Abbreviations: CASI, compact airborne spectrographic imager; CF, chlorophyll fluorescence; C_{a+b}, chlorophyll $a + b$; CUR, reflectance curvature index [$(R_{675}\cdot R_{690})/R^2_{683}$]; DCI, derivative chlorophyll index; D_λ, value of the derivative reflectance at wavelength X in nanometers; FRT, fluorescence–reflectance–transmittance model; F'_m, steady state maximal fluorescence; F_s, steady state fluorescence; F_v/F_m, ratio of variable to maximal fluorescence; $\Delta F/F'_m$, effective quantum yield; PAM, pulse amplitude modulation; PS-I, Photosystem I; PS-II, Photosystem II; RMSE, root mean square error; RT, radiative transfer; R_λ, value of the reflectance at wavelength X in nanometers.

are rapid, nondestructive, and noninvasive (Mohammed et al., 1995).

Evidence of a solar-induced fluorescence signal superimposed on leaf reflectance signatures was first reported by Buschmann and Lichtenthaler (1988) as a result of laboratory studies with a reflection–absorption–fluorescence spectrometer. Other studies of the effect of fluorescence in apparent reflectance have been conducted (Peñuelas et al., 1995; Gamon et al., 1997; Peñuelas et al., 1997, 1998; Gamon and Surfus, 1999; Gitelson et al., 1999), although the effect of the fluorescence signal on the apparent reflectance spectra of leaves has not been quantified.

A study of whether chlorophyll fluorescence is measurable with a passive instrument such as an airborne hyperspectral imager (Zarco-Tejada, 2000) showed that radiative transfer (RT) theory, constrained by appropriate modeling assumptions, can be investigated at leaf, laboratory, and near-field scales to demonstrate that CF effects are detectable as part of leaf reflectance and transmittance, as well as near-canopy reflectance measurements collected over vegetation. Further studies of the theoretical basis for quantitatively estimating pigments by scaling up optical indices have focused on remote sensing methods based on RT and infinite reflectance models (Zarco-Tejada et al., 2000a,b, 2001a,b).

Extensive research performed at the leaf level have demonstrated the use of a large number of optical indices for C_{a+b} estimation, enabling the study of differences in reflectance between healthy and stressed vegetation due to changes in pigment levels (e.g., Rock et al., 1988; Vogelmann et al., 1993; Carter, 1994). Estimating pigment content with optical indices has been shown to produce the best results at leaf and canopy levels with red-edge, spectral, and derivative red-edge indices (Zarco-Tejada et al., 2001b).

Investigation of the effects of fluorescence contributions to the remotely observed signature identified optical indices calculated from leaf reflectance measurements related specifically to fluorescence emission in the 680- to 740-nm spectral region due to PS-II and PS-I (Zarco-Tejada et al., 2000a,b). Indices related to fluorescence maxima at 685 and 735 nm may be useful to study the relationship of leaf and canopy reflectance with chlorophyll fluorescence, such as R_{685}/R_{655}, $R_{683}^2/(R_{675} \cdot R_{691})$, and D_{730}/D_{706}.

These indices were assessed through RT modeling with the FRT simulation model (Zarco-Tejada et al., 2000a), which includes fluorescence flux in the RT differential equations. Here we discuss the results of an assessment of a coupled FRT with the PROSPECT leaf model (Jacquemoud and Baret, 1990) for fluorescence estimation by model inversion. Further, we look at the effects of chlorophyll fluorescence and pigment content on the derivative reflectance, focusing on the understanding of such effects on hyperspectral imagery collected with the airborne CASI instrument.

MATERIALS AND METHODS

Data Collection

In 1998 and 1999, leaf material was sampled from three-year-old potted trees of sugar maple for laboratory–greenhouse experiments and from twelve 30- × 30-m sugar maple study sites in the Algoma Region, Ontario, Canada.

The greenhouse experiments required one set of 30 leaves with similar chlorophyll content (49 to 53 units according to SPAD-502 [Minolta Camera Co., Osaka, Japan] chlorophyll meter readings and from subsequent pigment analysis, $\bar{x}$ = 58.08 μg/cm^2, s = 5.26, n = 30). Leaf samples with similar chlorophyll content were required to study how the apparent leaf reflectance and transmittance vary due to the effects of chlorophyll fluorescence. For the second greenhouse experiment, 60 leaves with variable chlorophyll content ($\bar{x}$ = 35.66 μg/cm^2, s = 15.87, n = 60) were sampled to study variations in the apparent leaf reflectance and transmittance due to changes in pigment content and chlorophyll fluorescence and were used to estimate pigment by model inversion.

In 1998 and 1999, 440 single leaf samples were collected from the 12 sugar maple study sites. Reflectance and transmittance were measured on these leaf samples with a LI-COR (Lincoln, NE) 1800-12 integrating sphere, coupled by a 200-μm-diameter single mode fiber to an Ocean Optics (Dunedin, FL) Model ST 1000 spectrometer, with a 1024-element detector array, 0.5-nm sampling interval, and approximately 7.3-nm spectral resolution in the 340- to 860-nm range.

Chlorophyll fluorescence variables F_v/F_m, F_t, $\Delta F/F'_m$, and F'_m were measured with a pulse amplitude modulation (PAM) fluorometer (PAM-2000; Heinz Walz GmbH, Effeltrich, Germany), which has been used widely in basic and applied fluorescence research (Mohammed et al., 1995). The term F_v/F_m quantifies the maximal efficiency of photon capture by open PS-II reaction centers and is one of the most widely used chlorophyll fluorescence variables. It is calculated from the equation $F_v/F_m = (F_m - F_o)/F_m$, where F_m is the maximal fluorescence yield of a dark-adapted sample, with all PS-II reaction centers fully closed, and F_o is the minimum fluorescence yield of a dark-adapted sample, with all PS-II reaction centers fully open. Effective quantum yield, which denotes the actual efficiency of PS-II photon capture of light by closed PS-II reaction centers, was determined as $\Delta F/F'_m = (F'_m - F_t)/F'_m$, where F'_m is the maximal fluorescence of a pre-illuminated sample with PS-II centers closed, and F_t is the fluorescence at steady state. Procedures used for measuring F_v/F_m and $\Delta F/F'_m$ were based on standard methods (Heinz-Walz-GmbH, 1993). To measure maximal fluorescence induction F_v/F_m, leaves were dark-adapted in bags at room temperature for at least 30 min.

In 1998 and 1999, airborne hyperspectral imagery was collected over the 12 sites of sugar maple where ground-truth samples were collected. The CASI sensor acquired hyperspectral reflectance data at 2-m spatial resolution and 72 spectral channels with 7.5-nm spectral bandwidth. The 12-bit radiometric resolution data collected by CASI were processed to at-sensor radiance with calibration coefficients derived in the laboratory. Simultaneously, a Micro-Tops II sunphotometer (Solar Light Co., Philadelphia, PA) was used to collect aerosol optical depth data at 550 nm so image data could be processed to ground reflectance with the CAM5S atmospheric correction model (O'Neill et al., 1997). Reflectance data were georeferenced with GPS data collected aboard the aircraft. Final registration of the hyperspectral mode imagery was achieved by registration to the CASI high spatial resolution imagery with visual identification of ground-referenced 1-m white targets, which served to accurately identify the location of the sites.

Modeling Chlorophyll Fluorescence and Chlorophyll $a + b$ Estimates at the Leaf Level with the Fluorescence–Reflectance–Transmittance and PROSPECT Models

Chlorophyll fluorescence effects on apparent reflectance were simulated at leaf level to validate the coupled FRT–

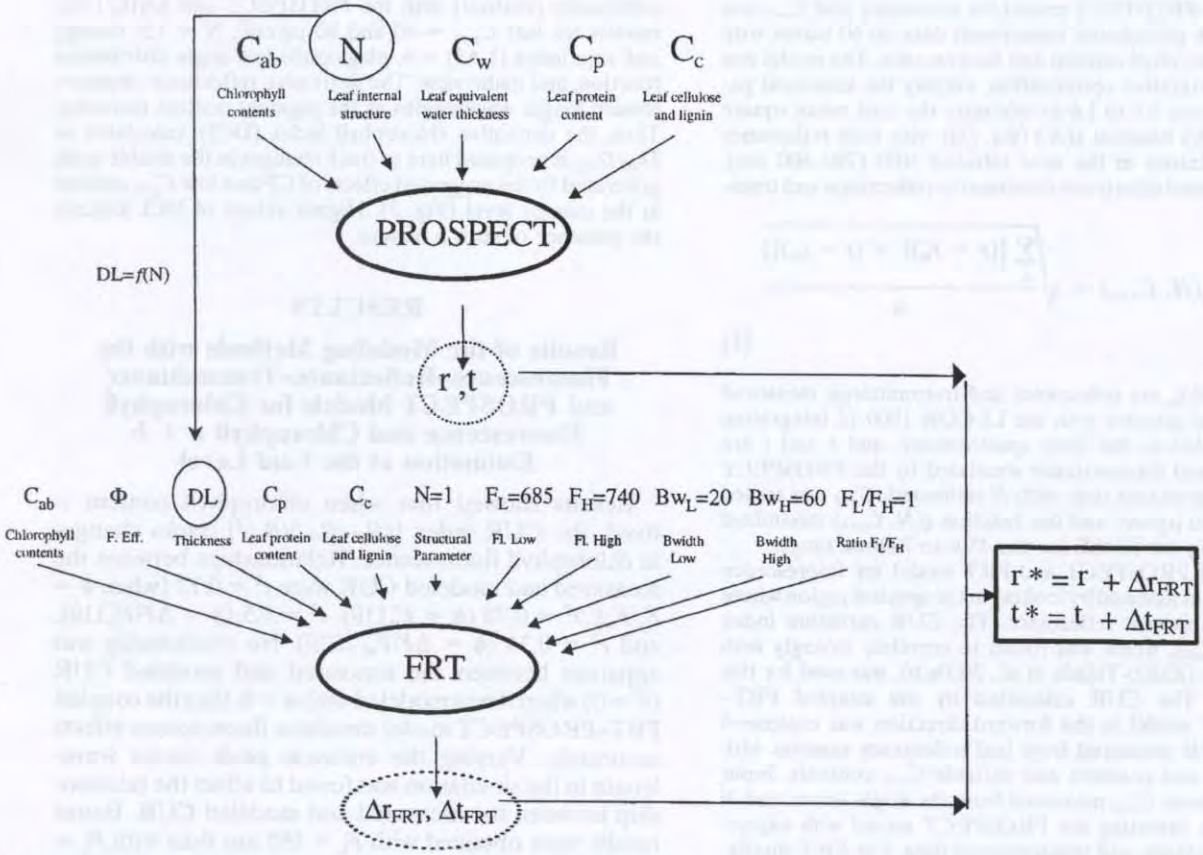

Fig. 1. Schematic diagram showing the coupling between the fluorescence–reflectance–transmittance (FRT) and PROSPECT models to calculate the change in reflectance (r^*) and transmittance (t^*) caused by accounting for chlorophyll fluorescence.

PROSPECT model (Fig. 1). The FRT model coupled to PROSPECT was used to simulate the effects of CF and variable C_{a+b} concentration on the derivative of reflectance to understand spectral features observed from airborne hyperspectral reflectance images collected at 2- × 2-m spatial resolution from healthy and stressed sugar maple study sites.

Experimental leaf reflectance, transmittance, pigment content, and chlorophyll fluorescence data were used for assessments through inversion of the coupled model by iterative optimization. The CF effects on leaf reflectance were simulated with the FRT model with input parameters leaf thickness (DL), C_{a+b} content (μg/cm^2), nominal values of protein content (C_p, in g/cm^2), cellulose and lignin content (C_c, in μg/cm^2), and equivalent water thickness (C_w, in cm). The fluorescence signal simulation inputs were the photon fluorescence efficiency (ϕ), ratio f (F_L/F_H) of the fluorescence peak at F_L (P-II center wavelength) relative to that at F_H (P-I center wavelength), and bandwidths B_L and B_H, the full width at half maximum of the fluorescence emissions centered at F_L and F_H wavelengths, respectively.

The coupling method consisted of adding the fluorescence signal modeled by FRT to the leaf reflectance and transmittance spectra simulated by PROSPECT, linking the variables DL (from FRT model) and the structural parameter (N) of the leaf mesophile (dimensionless, from PROSPECT model) through an empirical relationship. The rest of the input parameters needed in FRT for fluorescence modeling (F_L, B_L, F_H, B_H, f, and ϕ) allowed calculation of fluorescence spectra in the 400- to 800-nm range, Δr_{FRT} and Δt_{FRT}, obtaining the final apparent reflectance (r^*) and transmittance (t^*) as $r^* = r + \Delta r_{FRT}$; $t^* = t + \Delta t_{FRT}$ (Fig. 2).

Canopy reflectance without the effects of fluorescence was simulated with the SAILH canopy reflectance model (Verhoef, 1984) with simulated leaf reflectance and transmittance from PROSPECT.

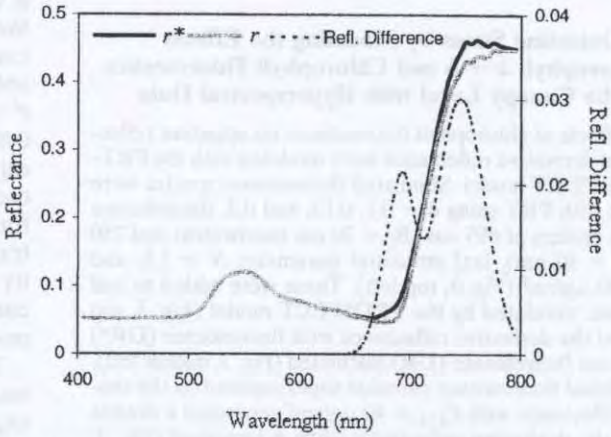

Fig. 2. Fluorescence–reflectance–transmittance (FRT) model simulation of leaf reflectance with the effects of fluorescence flux. Parameters used for the simulation: ϕ = 0.085, C_{a+b} content = 50 μg/cm^2, D_L = 0.075 mm, F_L = 688 nm, B_L = 30 nm, F_H = 746 nm, B_H = 52 nm, f ratio F_H/F_L = 0.94, labeled as r^* (with fluorescence), r (without fluorescence).

The FRT–PROSPECT model for estimating leaf C_{a+b} was assessed with greenhouse experiment data on 60 leaves with variable chlorophyll content and fluorescence. The model was inverted by iterative optimization, varying the structural parameter N from 0.9 to 1.6 to minimize the root mean square error (RMSE) function $\xi(N)$ (Eq. [1]) with both reflectance and transmittance in the near infrared NIR (780–800 nm), where structural effects are dominant in reflectance and transmittance:

$$\mathrm{RMSE} = \xi(N, C_{a+b}) = \sqrt{\frac{\sum_{\lambda} [(r - r_m)_\lambda^2 + (t - t_m)_\lambda^2]}{n}} \quad [1]$$

where r_m and t_m are reflectance and transmittance measured from the leaf samples with the LI-COR 1800-12 integrating sphere coupled to the fiber spectrometer, and r and t are reflectance and transmittance simulated by the PROSPECT model. In the second step, with N estimated, C_{a+b} was varied from 10 to 70 μg/cm² and the function $\xi(N, C_{a+b})$ minimized by calculating the RMSE for the 450- to 700-nm range.

The coupled PROSPECT and FRT model for fluorescence estimation was assessed by looking at the spectral region where CF affects apparent reflectance. The CUR curvature index $[(R_{675} \cdot R_{690})/R_{683}^2]$, which was found to correlate strongly with fluorescence (Zarco-Tejada et al., 2000a,b), was used for this assessment. The CUR calculated by the coupled FRT–PROSPECT model in the forward direction was compared with the CUR measured from leaf reflectance samples with variable CF and constant and variable C_{a+b} contents. Input parameters were C_{a+b} measured from the single leaves and N estimated by inverting the PROSPECT model with experimental reflectance and transmittance data. For FRT simulation, inputs were F_L, B_L, F_H, B_H, and fluorescence efficiency ϕ set to 0 (to simulate the CUR without fluorescence effects), and set to PAM-measured variables F_v/F_m, F'_m, and $\Delta F/F'_m$ (to simulate the CUR with fluorescence effects). Steady state fluorescence variables were measured with a halogen light attachment (excitation wavelength < 710 nm) at 110 and 2820 μmol quanta/(m² s) to correspond to photosynthetic photon flux densities used to measure reflectance and transmittance with the LI-COR sphere (indicated hereafter as $\Delta F/F'_m110$, F'_m110, $\Delta F/F'_m2820$).

Detecting Stress by Modeling the Effects of Chlorophyll $a + b$ and Chlorophyll Fluorescence at the Canopy Level with Hyperspectral Data

The effects of chlorophyll fluorescence on apparent reflectance and derivative reflectance were modeled with the FRT–PROSPECT RT model. Simulated fluorescence spectra were modeled with FRT using $\phi = 0.1$, 0.15, and 0.2, fluorescence emission centers at 695 nm (B_L = 30 nm bandwidth) and 750 nm (B_H = 40 nm), leaf structural parameter $N = 1.5$, and C_{a+b} = 40 μg/cm² (Fig. 3, top left). These were added to leaf reflectance simulated by the PROSPECT model (Fig. 3, top right) and the derivative reflectance with fluorescence (DR*) and without fluorescence (DR) calculated (Fig. 3, middle left). The modeled fluorescence emission superimposed on the simulated reflectance with C_{a+b} = 40 μg/cm² generated a double peak in the derivative reflectance when ϕ increased (Fig. 3, middle plot, left) due to the effect of the emission bands in the PS-I and PS-II regions. Canopy reflectance without the effects of fluorescence was simulated for different values of pigment content, and its derivative was calculated. Figure 4 shows the simulated canopy reflectance (top) and derivative reflectance (bottom) with the PROSPECT and SAILH RT models for leaf C_{a+b} = 40 and 80 μg/cm², $N = 1.5$, canopy leaf area index (LAI) = 6, plagiophile leaf angle distribution function, and nadir view. The derivative reflectance displaces toward longer wavelengths as the pigment content increases. Thus, the derivative chlorophyll index (DCI), calculated as D_{705}/D_{722}, is proposed here to track changes in the double peak generated by the suggested effects of CF and low C_{a+b} content at the canopy level (Fig. 5). Higher values of DCI indicate the presence of such a feature.

RESULTS

Results of the Modeling Methods with the Fluorescence–Reflectance–Transmittance and PROSPECT Models for Chlorophyll Fluorescence and Chlorophyll $a + b$ Estimation at the Leaf Level

Results showed that when chlorophyll content is fixed, the CUR index $[(R_{675} \cdot R_{690})/R_{683}^2]$ tracks changes in chlorophyll fluorescence. Relationships between the measured and modeled CUR were $r^2 = 0.72$ (when $\phi = F_v/F_m$), $r^2 = 0.78$ ($\phi = F'_m110$), $r^2 = 0.5$ ($\phi = \Delta F/F'_m110$), and $r^2 = 0.34$ ($\phi = \Delta F/F_m'2820$). No relationship was apparent between the measured and modeled CUR ($r^2 = 0$) when it was modeled with $\phi = 0$, thus the coupled FRT–PROSPECT model simulates fluorescence effects accurately. Varying the emission peak center wavelength in the simulation was found to affect the relationship between the measured and modeled CUR. Better results were obtained with F_L = 685 nm than with F_L = 690 nm (in both cases B_L = 20 nm) as indicated by $r^2 = 0.78$ ($\phi = F'_m110$; F_L = 685 nm) (Fig. 6) and $r^2 = 0.68$ ($\phi = F'_m110$; F_L = 690 nm). These results demonstrate that the modeled CUR performs well as a reflectance index function of fluorescence emission and that coupling PROSPECT and FRT results in an accurate simulation of the fluorescence effect in apparent reflectance. The best correlation results were obtained by selecting F'_m110 and F_v/F_m as measures of fluorescence efficiency ϕ, with the lack of correlation when $\phi = 0$ demonstrating that the CUR is determined by fluorescence when C_{a+b} content is constant. When both C_{a+b} and CF were variable, the CUR was also affected by changes in C_{a+b}: $r^2 = 0.73$ when the CUR was modeled with $\phi = 0$; $r^2 = 0.85$ ($\phi = F_v/F_m$), and $r^2 = 0.87$ ($\phi = F'_m110$). The C_{a+b} estimation from the set of leaves with variable pigment content achieved $r^2 = 0.96$ and RMSE = 0.02 (Fig. 7) for comparison of estimated and measured C_{a+b} concentration from each leaf. Therefore, the pigment variability within the set of leaf samples used in this study was correctly estimated with the linked FRT–PROSPECT model.

To estimate ϕ, the coupled FRT–PROSPECT model was inverted with reflectance spectra collected in the experiments with constant and variable C_{a+b} and CF. The function minimized was the RMSE between the measured and modeled CUR. Results obtained with constant C_{a+b} allowed modeled fluorescence ϕ estimated by inversion and fluorescence variables measured with PAM (Table 1; Fig. 8) to be compared. These results

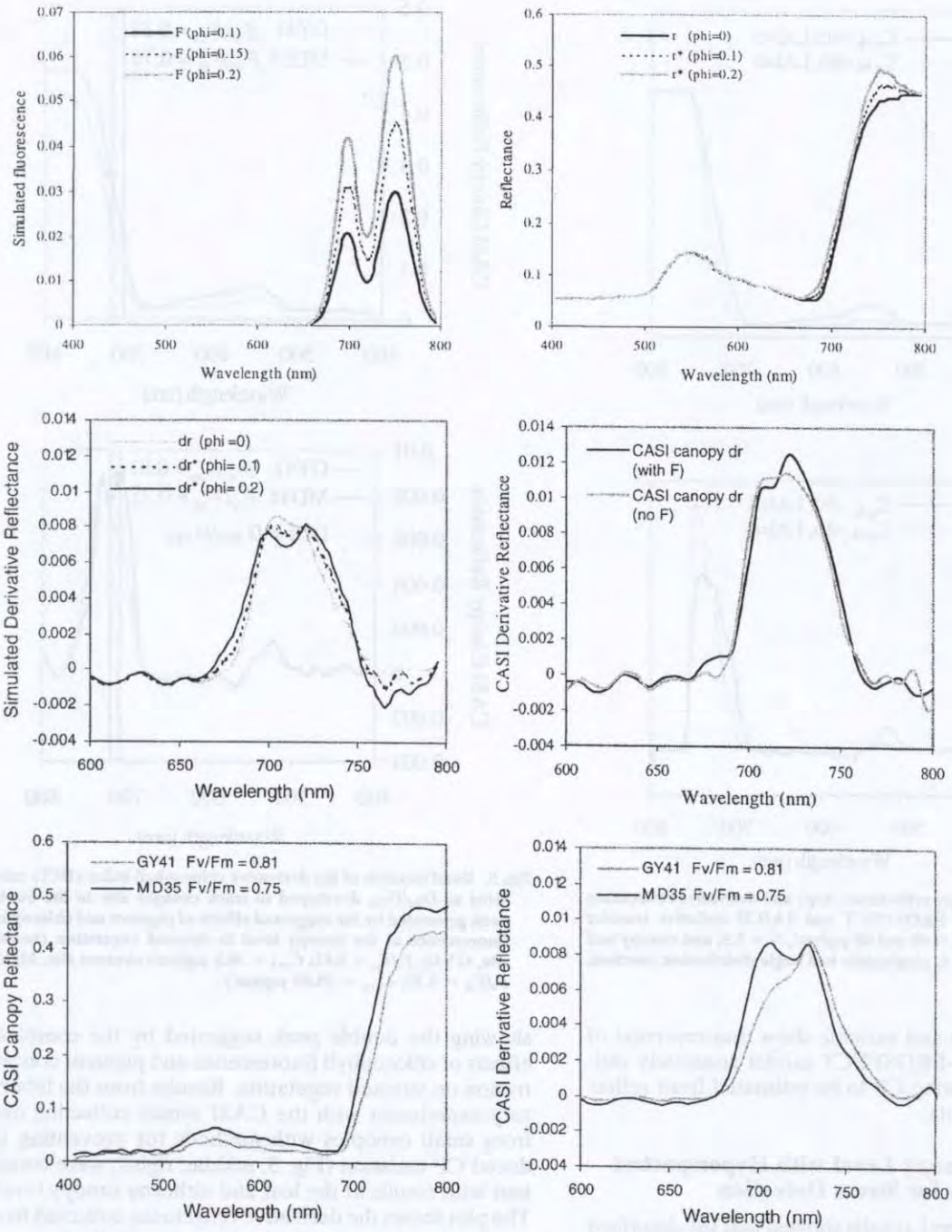

Fig. 3. Simulated leaf reflectance including the effects of fluorescence using the fluorescence–reflectance–transmittance (FRT) model (top and middle left plots) and compact airborne spectrographic imager (CASI) reflectance in the laboratory (middle right plot) and from an airborne campaign (bottom two plots). Top left plot shows simulated fluorescence emission for different values of ϕ (ranging from 0 to 0.2), and superimposed on leaf reflectance (top right plot) with peaks at 695 nm (B_L = 30 nm) and 750 nm (B_H = 40 nm), N = 1.5, and C_{a+b} = 40 μg/cm². Derivative reflectance (middle left plot) for different fluorescence simulations shows a double peak as function of fluorescence emission. Laboratory CASI reflectance from sugar maple seedlings with and without fluorescence emission shows that such effects are captured on the derivative reflectance (middle right plot). Airborne CASI data collected over 30- × 30-m sugar maple study sites (bottom plots) from the two sites with highest field-measured F_v/F_m and C_{a+b} (GY41, F_v/F_m = 0.81; C_{a+b} = 38.8 μg/cm²) and lowest (MD35, F_v/F_m = 0.75; C_{a+b} = 19.08 μg/cm²) show comparable double peak features.

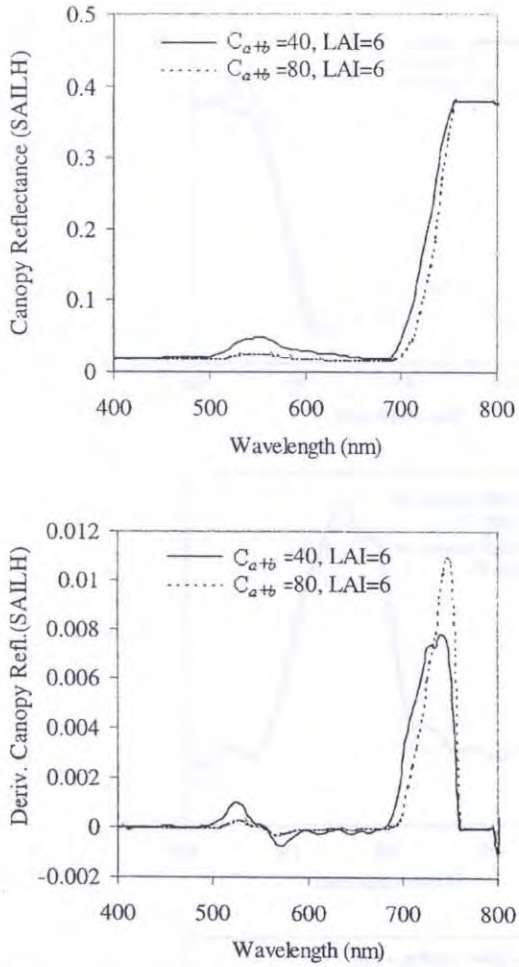

Fig. 4. Simulated canopy reflectance (top) and derivative reflectance (bottom) using the PROSPECT and SAILH radiative transfer models for leaf C_{a+b} = 40 and 80 μg/cm², N = 1.5, and canopy leaf area index (LAI) = 6, plagiophile leaf angle distribution function, and nadir view.

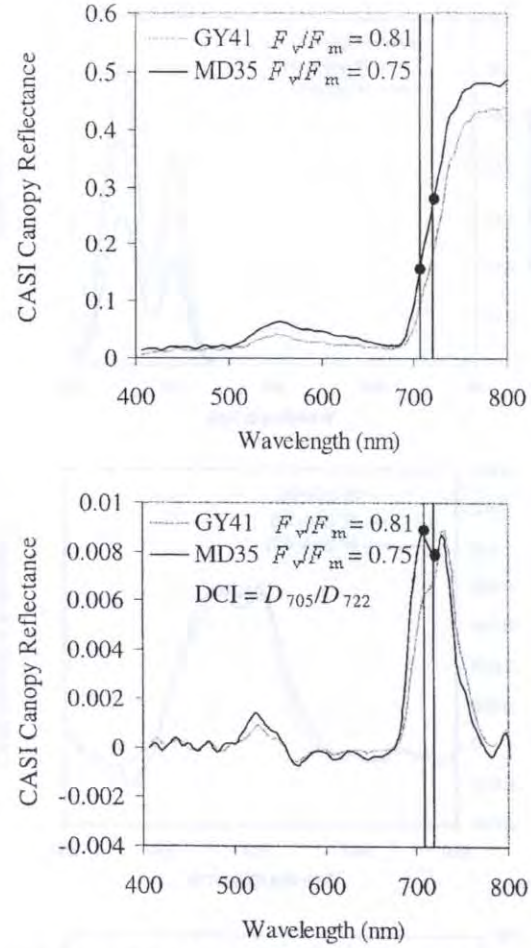

Fig. 5. Band location of the derivative chlorophyll index (DCI) calculated as D_{705}/D_{722}, developed to track changes due to the double peak generated by the suggested effects of pigment and chlorophyll fluorescence at the canopy level in stressed vegetation (healthy site, GY41: F_v/F_m = 0.81; C_{a+b} = 38.8 μg/cm²; stressed site, MD35: F_v/F_m = 0.75; C_{a+b} = 19.08 μg/cm²)

with C_{a+b} constant and variable show that inversion of the coupled FRT–PROSPECT model accurately estimates ϕ, thus allowing CF to be estimated from reflectance measurements.

Results at Canopy Level with Hyperspectral Data for Stress Detection

At the canopy level, results showed that the described double-peak effect was found on hyperspectral CASI reflectance images. Airborne imagery was analyzed from the two 20- × 20-m study areas with highest and lowest stress conditions characterized by C_{a+b} and CF measured in the field. Ground-truth data from the stressed study site reported C_{a+b} = 19.08 μg/cm² and F_v/F_m = 0.75, while data from the healthy site resulted in C_{a+b} = 38.8 μg/cm² and F_v/F_m = 0.83.

Hyperspectral reflectance spectra from the healthy and stressed sites (Fig. 3, bottom left, labeled as healthy = GY41 and stressed = MD35) were used to calculate the derivative reflectance (Fig. 3, bottom right) showing the double peak suggested by the combined effects of chlorophyll fluorescence and pigment concentration on stressed vegetation. Results from the laboratory experiment with the CASI sensor collecting data from small canopies with methods for preventing induced CF emission (Fig. 3, middle, right), were consistent with results at the leaf and airborne canopy levels. The plot shows the derivative reflectance collected from the maple canopy in the laboratory with fluorescence emission (after the light source is turned on, therefore exciting fluorescence emission) and after fluorescence emission decreased. Therefore, differences in the derivative reflectance found in this experiment are due to variations in chlorophyll fluorescence tracked at the canopy level with the hyperspectral sensor in the laboratory setting.

These results suggest that hyperspectral reflectance can be used to map stress condition through optical indices calculated on the double-peak red-edge region of the derivative reflectance. The appearance of the

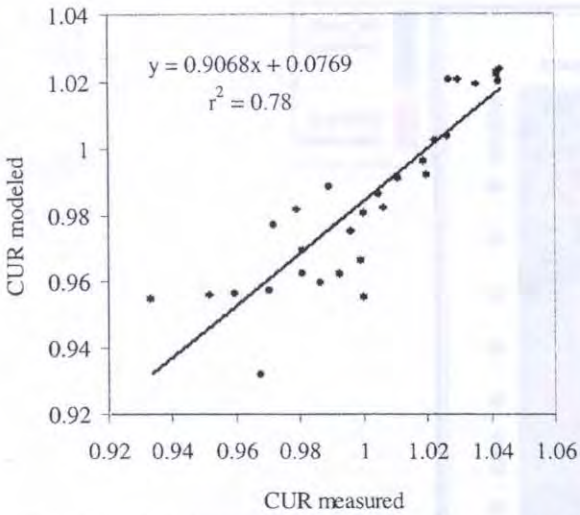

Fig. 6. Relationship between the reflectance curvature index [CUR; $(R_{675}\cdot R_{690})/R_{683}^2$] measured from leaf samples (experiment with C_{a+b} constant) and modeled by fluorescence–reflectance–transmittance (FRT)–PROSPECT. F'_m110 was used as input for ϕ in FRT–PROSPECT model.

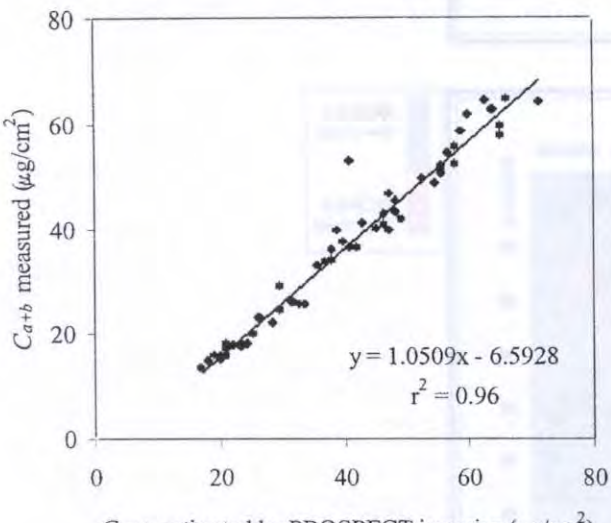

Fig. 7. Estimation of C_{a+b} by inversion of the PROSPECT leaf radiative transfer (RT) model from 60 reflectance and transmittance spectra and C_{a+b} measured from leaves samples with variable chlorophyll content ($\bar{x}$= 35.66 μg/cm², s = 15.87, n = 60).

double peak could indicate stress conditions due to low pigment content and the existence of CF emission. The severity of the stress would presumably need to be significant or prolonged to exhaust the normal physiological mechanisms that quench CF (thereby reducing its emission) during early stages of stress (Mohammed et al., 1995).

The proposed DCI derivative index was applied to hyperspectral derivative reflectance collected with the CASI sensor over the two study sites with highest and lowest stress conditions (Fig. 9). The 500- × 500-m sugar maple areas showing the 20- × 20-m study sites with lowest field-measured stress (GY41, Fig. 9, top) and

Table 1. Determination coefficients calculated between pulse amplitude modulation (PAM) chlorophyll fluorescence (CF) measurements F_v/F_m, F'_m110, F'_m2820, F_t110, F_t2820, $\Delta F/F'_m110$, and $\Delta F/F'_m2820$ and the estimated ϕ from leaf reflectance data using the fluorescence–reflectance–transmittance (FRT)–PROSPECT model.

	F_v/F_m	F'_m110	F'_m2820	F_t110	F_t2820	$\Delta F/F'_m110$	$\Delta F/F'_m2820$
C_{a+b} constant	0.75	0.75	0.79	0.62	0.77	0.55	0.39
C_{a+b} variable	0.5	0.74	0.66	0.64	0.62	0.62	0.33

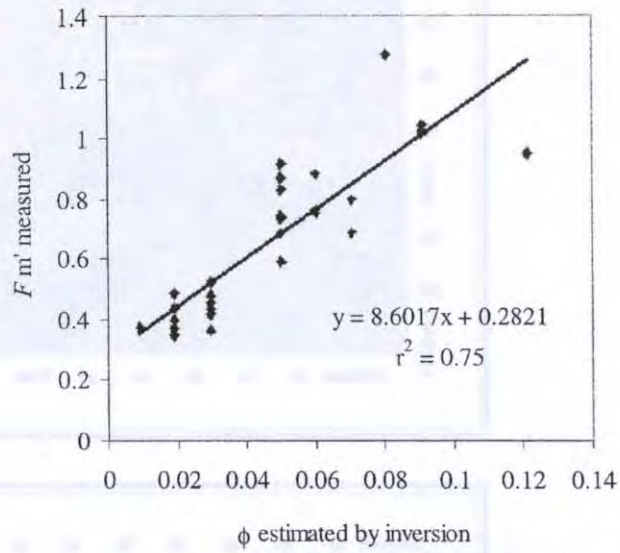

Fig. 8. Relationship between F'_m110 measured from leaf samples (experiment with C_{a+b} constant) and ϕ estimated by inversion of fluorescence–reflectance–transmittance (FRT)–PROSPECT.

highest stress (MD35, Fig. 9, bottom) were mapped with DCI reflectance index. Areas of vegetation stress are identified on the 2- × 2-m spatial resolution airborne images in red. Results from the DCI index are consistent with the ground-truth C_{a+b} and F_v/F_m data measured in the field. Coefficients of determination obtained between DCI and F_v/F_m (r^2 = 0.6) and between DCI and C_{a+b} (r^2 = 0.42) from the airborne hyperspectral imagery collected over the 12 study sites demonstrate the relationship between ground truth measures of stress and the double-peak red-edge DCI reflectance.

SUMMARY

Leaf-level PAM-measured fluorescence variables such as F_v/F_m, F_t, $\Delta F/F_m'$, and F_m' can be estimated from leaf reflectance and transmittance by inverting the coupled FRT and PROSPECT models. Through a set of laboratory experiments with sugar maple leaves, leaf reflectance and transmittance data were collected with a LI-COR integrating sphere attached to a fiber spectrometer, as were CF measurements with a PAM fluorometer. Using the FRT model and experiments with leaf samples with constant and variable C_{a+b} and CF, leaf-level optical indices that can track CF changes through measuring apparent reflectance were validated. Fluorescence-sensitive indices associated with reflectance changes at 690 and 750 nm, such as the curvature

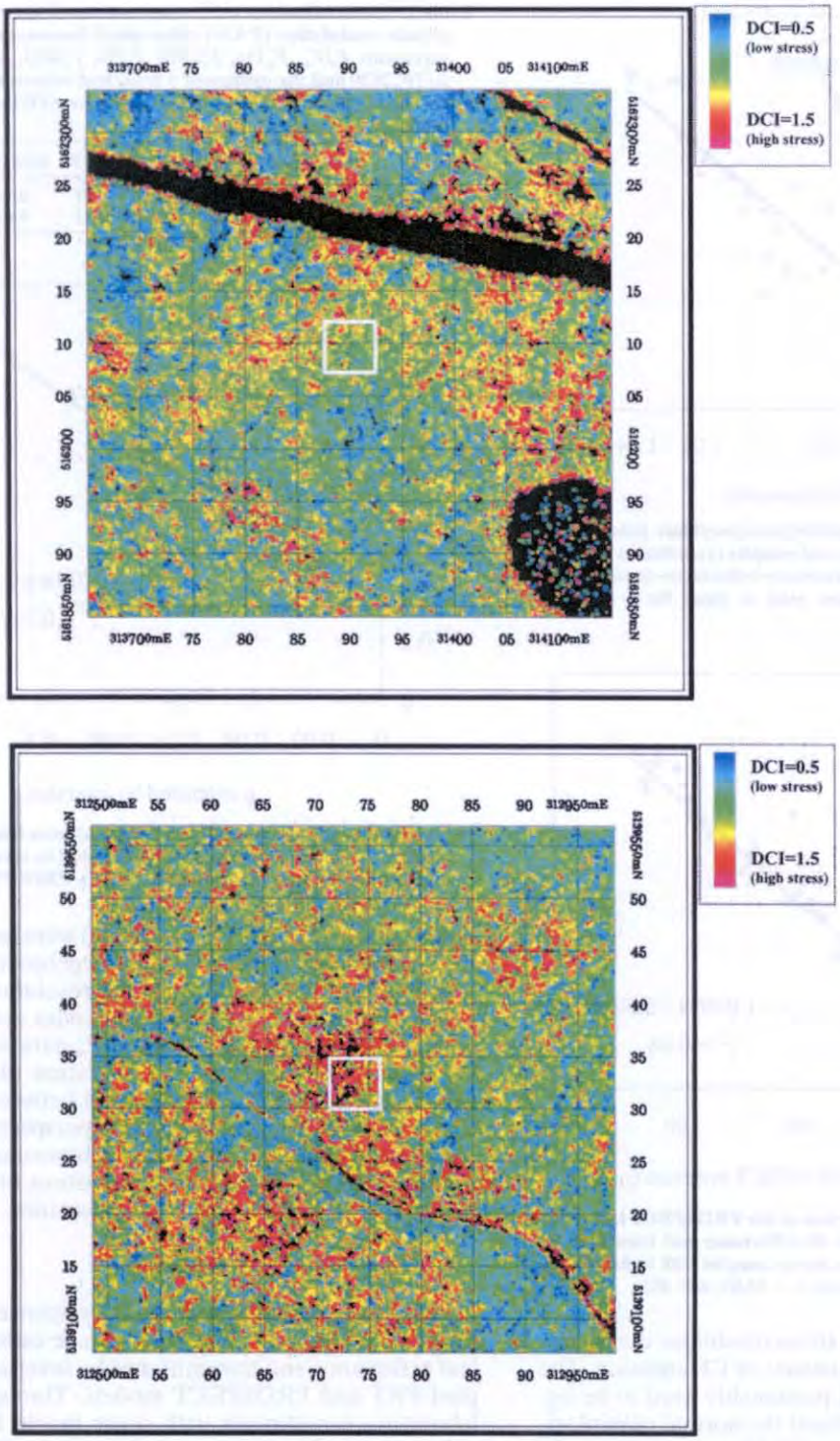

Fig. 9. The derivative chlorophyll index (DCI) applied to hyperspectral derivative reflectance collected with the compact airborne spectrographic imager (CASI) airborne sensor. Remote sensing images were collected over the two study sites with low (top image) and high (bottom image) stress conditions to map the double peak as an indicator of stress. Images show the 500- × 500-m sugar maple areas with the 20- × 20-m study sites with highest field-measured C_{a+b} and F_v/F_m (GY41, F_v/F_m = 0.81, C_{a+b} = 38.8 μg/cm², top image) and lowest F_v/F_m (MD35, F_v/F_m = 0.75, C_{a+b} = 19.08 μg/cm², bottom image). Areas of vegetation stress are identified on the 2- × 2-m spatial resolution airborne images in red.

index $(R_{675} \cdot R_{690})/R_{683}^2$, were tested in numerical model inversion through FRT coupled to the PROSPECT leaf model. Inverting FRT–PROSPECT from leaf reflectance and transmittance measurements resulted in accurate estimation ($r^2 = 0.7$) of dark-adapted and steady state fluorescence measures, such as F_v/F_m, F_m', and F_t. The CF and C_{a+b} effects on the derivative reflectance were modeled showing a double peak in the red-edge region, which is likely due to the combined effects of fluorescence emission and low pigment content on stressed vegetation and is demonstrated by RT modeling. Consistency was found between laboratory time-decay experiments and airborne hyperspectral CASI derivative reflectance collected from two sites of extreme health conditions. The DCI calculated as D_{705}/D_{722} based on the double peak of derivative reflectance is proposed for mapping vegetation stress. The coefficients of determination between the DCI calculated from 12 imaged sites of sugar maple and ground-truth F_v/F_m and C_{a+b} were 0.6 and 0.42, respectively. These results demonstrate the potential of derivative spectroscopy in the red-edge region with hyperspectral remote sensing to map vegetation stress effects.

ACKNOWLEDGMENTS

The authors gratefully acknowledge the financial support provided for this research through the Centre for Research in Earth and Space Technology (CRESTech), the Ontario Ministry of Natural Resources, and GEOIDE (Geomatics for Informed Decisions), part of the Canadian Networks of Centres of Excellence program. Special thanks are due to J. Harron (CRESTech) for developing the apparatus to perform single leaf measurements and S. Jacquemoud for making the PROSPECT code available.

REFERENCES

Buschmann, C., and H.K. Lichtenthaler. 1988. Reflectance and chlorophyll fluorescence signatures in leaves. p. 325–332. *In* H.K. Lichtenthaler (ed.) Applications of chlorophyll fluorescence. Kluwer Academic Publ., Dordrecht, the Netherlands.

Canadian Forest Service. 1999. Forest health in Canada: An overview. Nat. Resour. Canada, Ottawa, ON.

Carter, G.A. 1994. Ratios of leaf reflectances in narrow wavebands as indicators of plant stress. Int. J. Remote Sens. 15:697–704.

Chapin, F.S. 1991. Integrated responses of plants to stress. BioScience 41:29–36.

Colombo, S.J., and W.C. Parker. 1999. Does Canadian forestry need physiology research? For. Chronicle 75:667–673.

Gamon, J.A., L. Serrano, and J.S. Surfus. 1997. The photochemical reflectance index: An optical indicator of photosynthetic radiation-use efficiency across species, functional types, and nutrient levels. Oecologia 112:492–501.

Gamon, J.A., and J.S. Surfus. 1999. Assessing leaf pigment content and activity with a reflectometer. New Phytol. 143:105–117.

Gitelson, A.A., C. Buschman, and H.K. Lichtenthaler. 1999. The chlorophyll fluorescence ratio F735/F700 as an accurate measure of chlorophyll content in plants. Remote Sens. Environ. 69:296–302.

Gitelson, A.A., and M.N. Merzlyak. 1996. Signature analysis of leaf reflectance spectra: Algorithm development for remote sensing of chlorophyll. J. Plant Physiol. 148:494–500.

Heinz-Walz-GmbH. 1993. Portable Fluorometer PAM-2000 and data acquisition software DA-2000. Heinz-Walz-GmbH, Effeltrich, Germany.

Jacquemoud, S., and F. Baret. 1990. Prospect: A model of leaf optical properties spectra. Remote Sens. Environ. 34:75–91.

Krause, G.H., and E. Weis. 1984. Chlorophyll fluorescence as a tool in plant physiology. II. Interpretation of fluorescence signals. Photosynth. Res. 5:139–157.

Larcher, W. 1994. Photosynthesis as a tool for indicating temperature stress events. p. 261–277. *In* E.D. Schulze and M.M. Caldwell (ed.) Ecophysiology of photosynthesis. Springer–Verlag, Berlin.

Lichtenthaler, H.K. 1992. The Kautsky effect: 60 years of chlorophyll fluorescence induction kinetics. Photosynthetica 27:45–55.

Lichtenthaler, H.K., and U. Rinderle. 1988. The role of chlorophyll fluorescence in the detection of stress conditions in plants. CRC Crit. Rev. Anal. Chem. 19(Suppl. 1):529–585.

Mohammed, G.H., W.D. Binder, and S.L. Gillies. 1995. Chlorophyll fluorescence: A review of its practical forestry applications and instrumentation. Scand. J. For. Res. 10:383–410.

O'Neill, N.T., F. Zagolski, M. Bergeron, A. Royer, J.R. Miller, and J. Freemantle. 1997. Atmospheric correction validation of casi images acquired over the BOREAS southern study area. Can. J. Remote Sens. 23:143–162.

Papageorgiou, G. 1975. Chlorophyll fluorescence: An intrinsic probe of photosynthesis. p. 319–371. *In* Govindjee (ed.) Bioenergetics of photosynthesis. Academic Press, New York.

Peñuelas, J., I. Filella, P. Lloret, F. Muñoz, and M. Vilajeliu. 1995. Reflectance assessment of mite effects on apple trees. Int. J. Remote Sens. 16–14:2727–2733.

Peñuelas, J., I. Filella, J. Llusia, D. Siscart, and J. Pinol. 1998. Comparative field study of spring and summer leaf gas exchange and photobiology of the mediterranean trees *Quercus ilex* and *Phillyrea latifolia*. J. Exp. Bot. 49:229–238.

Peñuelas, J., J. Llusia, J. Piñol, and I. Filella. 1997. Photochemical reflectance index and leaf photosynthetic radiation-use-efficiency assessment in Mediterranean trees. Int. J. Remote Sens. 18:2863–2868.

Rock, B.N., T. Hoshizaki, and J.R. Miller. 1988. Comparison of in situ and airborne spectral measurements of the blue shift associated with forest decline. Remote Sens. Environ. 24:109–127.

Sampson, P.H., G.H. Mohammed, P.J. Zarco-Tejada, J.R. Miller, T.L. Noland, D. Irving, P.M. Treitz, S.J. Colombo, and J. Freementle. 2000. The bioindicators of forest condition project: A physiological, remote sensing approach. For. Chronicle 76(6):941–952.

Schreiber, U., and W. Bilger. 1987. Rapid assessment of stress effects on plant leaves by chlorophyll fluorescence measurements. p. 27–53. *In* J.D. Tenhunen and E.M. Catarino (ed.) Plant response to stress. Springer–Verlag, Berlin.

Schreiber, U., W. Bilger, and C. Neubauer. 1994. Chlorophyll fluorescence as a non-destructive indicator for rapid assessment of in vivo photosynthesis. Ecol. Stud. 100:49–70.

Verhoef, W. 1984. Light scattering by leaf layers with application to canopy reflectance modeling: The SAIL model. Remote Sens. Environ. 16:125–141.

Vogelmann, J.E., B.N. Rock, and D.M. Moss. 1993. Red edge spectral measurements from sugar maple leaves. Int. J. Remote Sens. 14: 1563–1575.

Zarco-Tejada, P.J. 2000. Hyperspectral remote sensing of closed forest canopies: Estimation of chlorophyll fluorescence and pigment content. Ph.D. thesis. Graduate Program in Earth and Space Sci., York Univ., Toronto.

Zarco-Tejada, P.J., J.R. Miller, G.H. Mohammed, and T.L. Noland. 2000a. Chlorophyll fluorescence effects on vegetation apparent reflectance: I. Leaf-level measurements and model simulation. Remote Sens. Environ. 74(3):582–595.

Zarco-Tejada, P.J., J.R. Miller, G.H. Mohammed, T.L. Noland, and P.H. Sampson. 2000b. Chlorophyll fluorescence effects on vegetation apparent reflectance: II. Laboratory and airborne canopy-level measurements with hyperspectral data. Remote Sens. Environ. 74(3): 596–608.

Zarco-Tejada, P.J., J.R. Miller, G.H. Mohammed, T.L. Noland, and P.H. Sampson. 2001a. Estimation of chlorophyll fluorescence under natural illumination from hyperspectral data. Int. J. Appl. Earth Observ. Geoinfo. 3:321–327.

Zarco-Tejada, P.J., J.R. Miller, T.L. Noland, G.H. Mohammed, and P.H. Sampson. 2001b. Scaling-up and model inversion methods with narrow-band optical indices for chlorophyll content estimation in closed forest canopies with hyperspectral data. IEEE Trans. Geosci. Remote Sens. 39(7):1491–1507.

Species Identification and Stress Detection of Heavy-Metal Contaminated Trees

I. Reusen, L. Bertels, W. Debruyn, B. Deronde, D. Fransaer, S. Sterckx

VITO - Flemish Institute for Technological Research, Mol, Belgium

INTRODUCTION

'Maatheide' in the north-eastern part of Belgium is contaminated with heavy metals like zinc, lead, cupper and cadmium due to several decades of zinc-melting activities. In August 2000 an airborne CASI campaign was organized in this region. CASI images were acquired with a spatial resolution of 1 m by 1 m in 18 'vegetation bands', mainly concentrated in the red edge curve (680 nm- 780 nm). The most dominant tree types in this region are pine, oak and birch. After the definition of pine, oak, birch, … regions of interest, SAM classification and subsequently multi-band segmentation and 'highest frequency smoothing', a pine mask, oak mask and birch mask were created. For the pine mask several vegetation stress indices (Peñuelas J., *et al.,*1994, Zarco P.J., 1999) were calculated. The 'EGFN' (Edge-Green First derivative Normalized difference) clearly indicates vegetation stress in pine trees in the region near the former zinc-melting factory and no vegetation stress in pine trees for the reference track where no heavy-metal contamination is expected.

OBJECTIVE OF THE STUDY AND LOCATION OF THE STUDY AREA

The aim of the study was to detect heavy-metal soil contamination by means of stress detection in vegetation which has its roots in the historical contamination. The study area is located in the north-eastern part of Belgium. At the end of the 70s the zinc factory was dismantled, crushed into small pieces and spread over the terrain. Therefore high concentrations of Zn (10000 mg/kg), Pb (1700 mg/kg), Cu (1000 mg/kg) and Cd (10-70 mg/kg) can be found at the site (J.Vangronsveld *et al*., 1995).

Data collection and processing

CASI images were collected in August 2000 over the contaminated region of 'Maatheide', and were accompanied with simultaneous dGPS, reflectance and irradiance measurements at the ground. The flights lines were oriented in SW-NE direction according the main wind direction and therefore the expected heavy-metal concentration gradient. The images were acquired with a spatial resolution of 1 m by 1 m in 18 'vegetation bands', mainly concentrated in the red edge curve (680 nm- 780 nm).

Location	Maatheide (north-eastern part of Belgium)
Sensor	CASI (Compact Airborne Spectrographic Imager)
Airplane	Piper Navajo Chieftain
Field of view	37.8°
Altitude	2600 ft
Ground speed	120 knots
Spatial resolution	1 m x 1 m
Swath width	511 m
Track length	30 km
Number of bands	18
Flight orientation	SW – NE

Table 1: Details of the CASI campaign 2000.

The geometrically corrected CASI images were atmospherically corrected with ATCOR4, developed by DLR. ATCOR4 allows to deduce radiometric calibration correction factors based on the ground reflectance measurements of natural and artificial targets.

DATA PROCESSING CHAIN

Figure 1 gives an overview of the used processing chain starting from 18 bands radiometric, geometric and atmospheric corrected CASI images. Due to a spectral calibration shift of the CASI sensor of a few nm, ATCOR4 was not able to correct properly at bands near the O_2 and H_2O absorption features. Therefore four spectral bands were removed. A vegetation mask is built using a NDVI threshold eliminating non-vegetation pixels in order to decrease the further processing time.

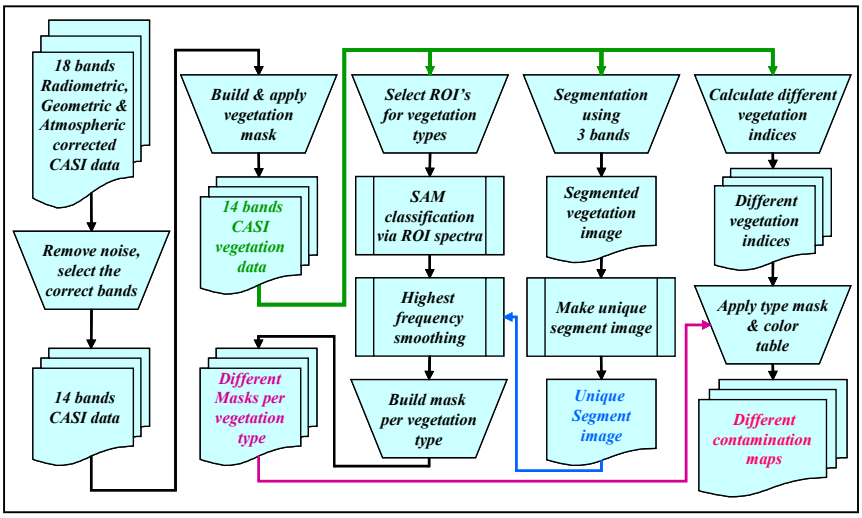

Figure 1. Processing chain: from 18 bands CAS Iimages to contamination maps.

ENVI's Spectral Angle Mapper (SAM) classification based on reference spectra determined from Regions Of Interest selected within the image (and verified in the field) results in a first rough classification, as shown in figure 2. The insert shows that a single tree is classified as consisting of different vegetation types. Multi-band segmentation with eCognition and 'highest frequency smoothing' is used to determine the final class for each tree (figure 3).

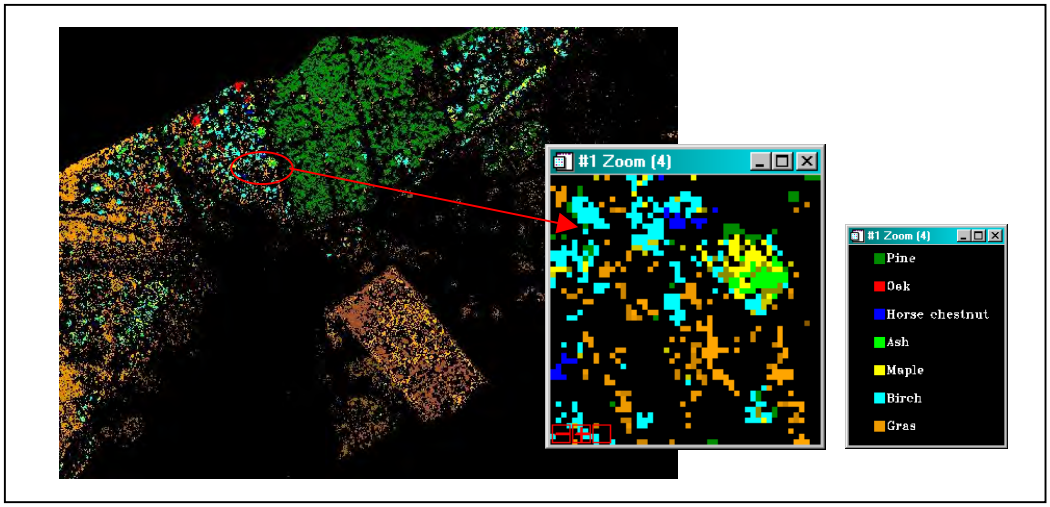

Figure 2: Result of SAM classification with image reference spectra. Insert: a single tree is classified as consisting of different vegetation types.

Three spectral bands were used to segment the image using color, shape and scale parameters with eCognition. The result is that corresponding pixels of a tree are clustered. Each segment is labeled with a unique number to allow identification of each segment (figure 3 middle). 'Highest Frequency Smoothing' finally determines the class attributed to each segment. To avoid misclassifications only segments consisting of at least 40% meaningful pixels are considered as shown in figure 3 (right).

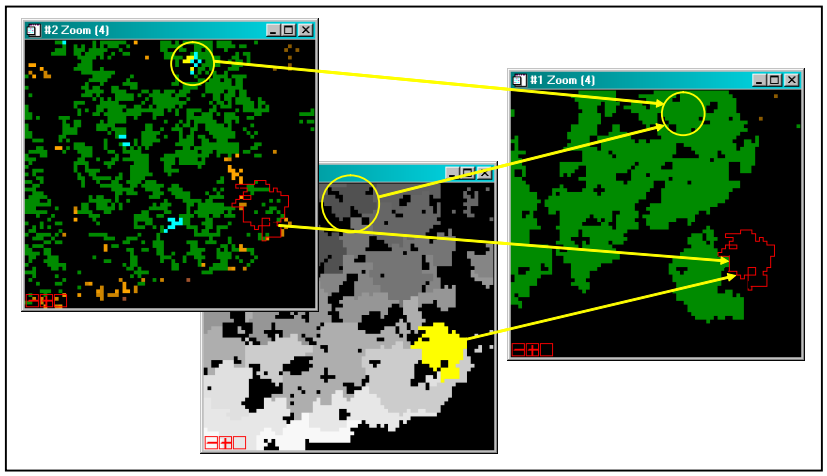

Figure 3: Left: Result of SAM classification with image reference spectra. A single tree is classified as consisting of different vegetation types. Middle: Result of multi-band segmentation with eCognition clustering pixels of a single tree (segment) together. Right: 'Highest Frequency Smoothing' determines the class attributed to each segment containing at least 40% meaningful pixels.

The final classification result after SAM classification, multi-band segmentation and 'Highest Frequency Smoothing' is shown in figure 4 (left). Subsequently a pine mask could be deduced from the Pine class of the final classification result (figure 4 right). Pine (*Pinus Sylvestris L.*) is the dominant tree type in this region.

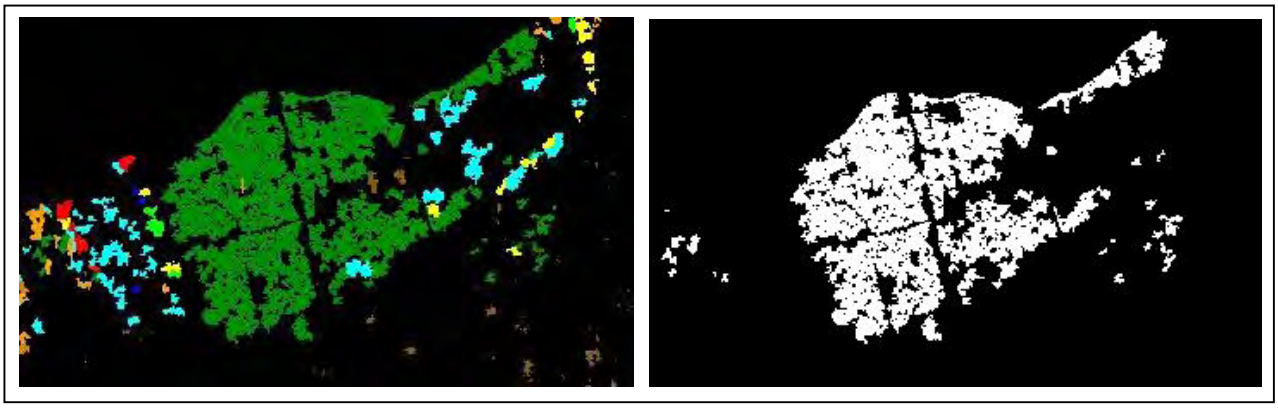

Figure 4: Left: Result of SAM classification, multi-band segmentation and 'Highest Frequency Smoothing'. Right: Pine mask deduced from the Pine class after SAM classification, multi-band segmentation and 'Highest Frequency Smoothing'.

For each pixel in the pine mask several vegetation stress indices (Peñuelas J., *et al.,*1994, Zarco P.J., 1999) were calculated and averaged per segment. The EGFN (Edge-Green First derivative Normalized difference) values are represented by a 10 percentile color code. The EGFN vegetation stress index clearly indicates high vegetation stress levels (low EGFN values) near the former zinc-melting factory (figure 5) and lower vegetation stress levels at more distant locations.

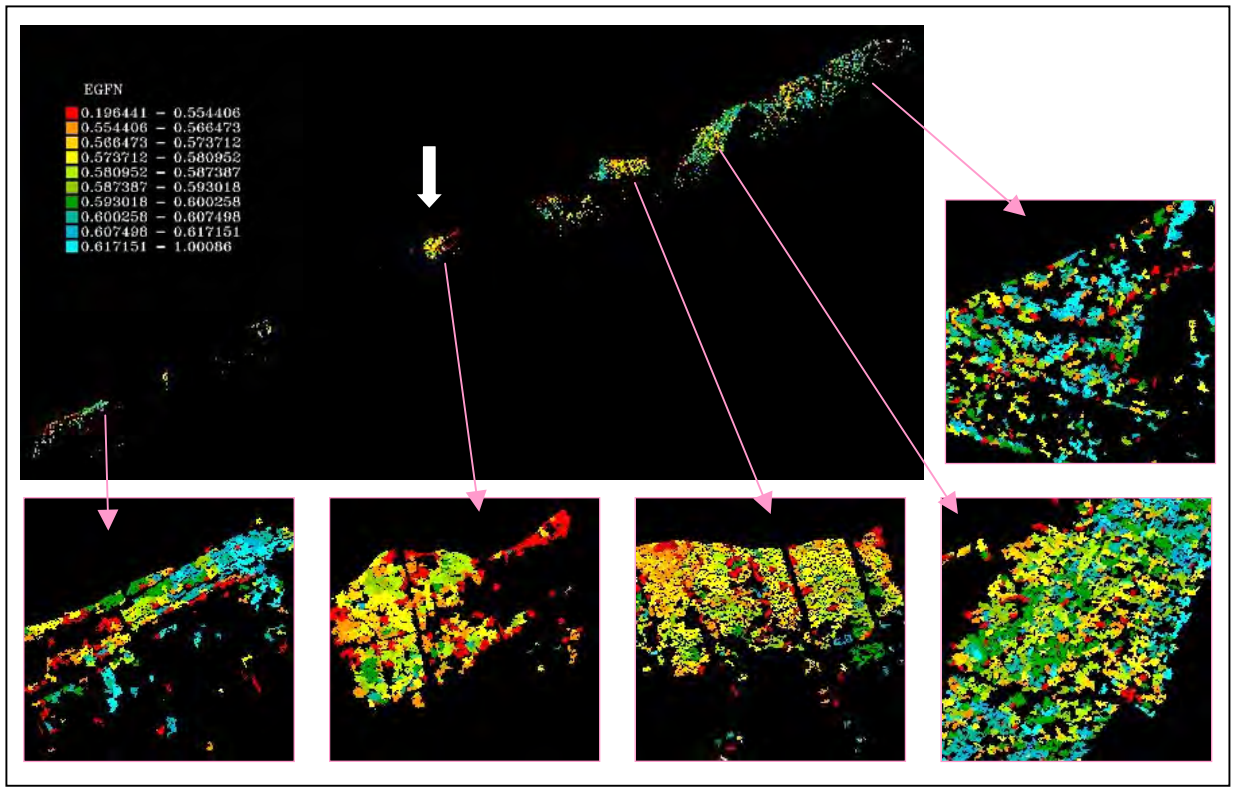

Figure 5: EGFN vegetation stress index map for pine in the 'Maatheide' track. The location of the former zinc melting factory is indicated by the white arrow.

The described vegetation stress detection technique was verified at a reference track where no heavy-metal contamination is expected. Figure 6 shows the location of the 'Maatheide' track with the former zinc melting factory indicated and the reference track.

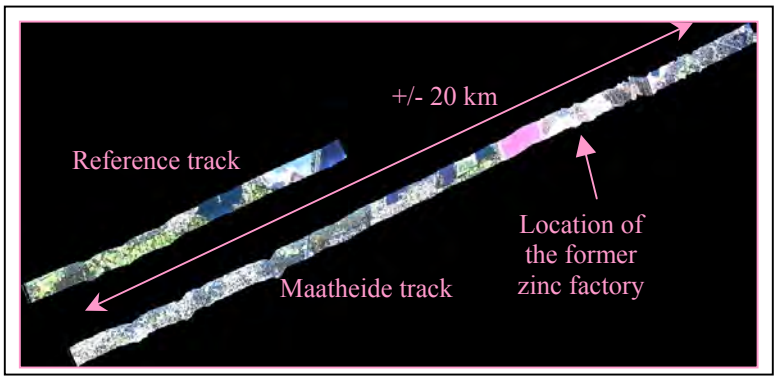

Figure 6: Location of the 'Maatheide' track with the former zinc melting factory indicated and reference track, where no heavy metal contamination is expected.

Subsequently both tracks are 25° rotated clockwise and divided into 100 m slices. If at least 2% meaningful pixels are present within the slice, the 20 percentile EGFN contribution bars are calculated. The location of the former zinc-melting factory is indicated. Figure 7 clearly shows low vegetation stress levels (high EGFN values) for the reference track as expected and high vegetation stress levels (low EGFN values) near the former zinc-melting factory. For comparison Cd concentrations, determined from soil and vegetable samples collected in gardens about 1000 m south of 'Maatheide' by LISEC, are displayed for the same 100 m slices. Clearly a correlation is present

between the vegetation stress index EGFN for pine and the Cd concentrations 1000 m south of 'Maatheide': high Cd concentrations (which are correlated with Zn concentrations) correspond to a low (red) EGFN value.

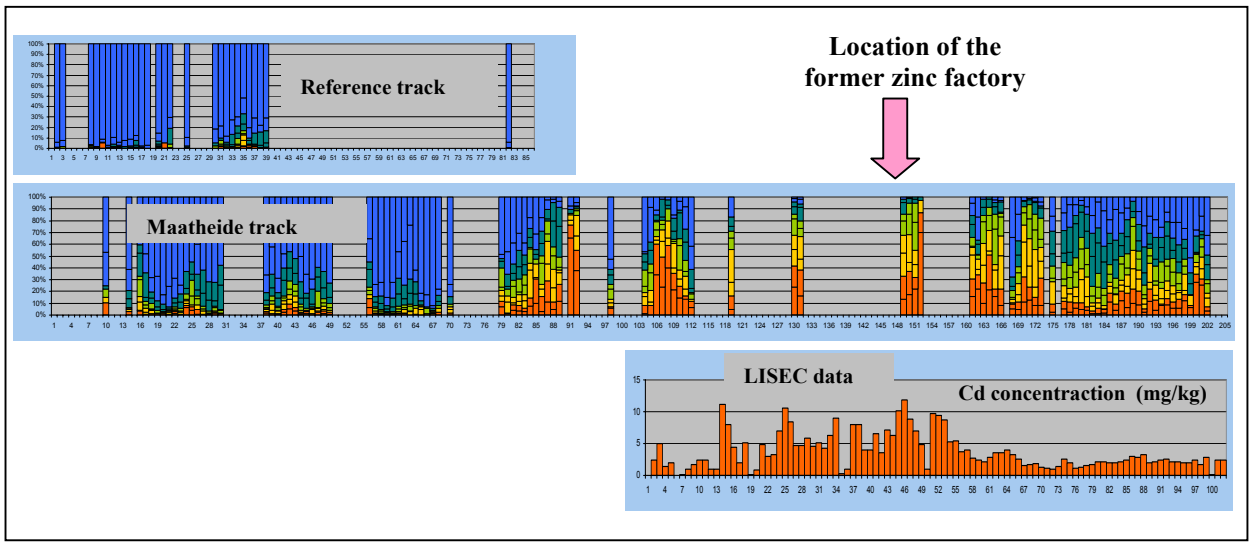

Figure 7: EGFN 20 percentile contribution bars for 100 m slices of the reference track and the 'Maatheide' track. For comparison the Cd concentration, determined from soil and vegetable samples collected 1000 m south of 'Maatheide', are displayed.

CONCLUSIONS

SAM classification of 14 bands CASI images with reference spectra from image ROI's, combined with multi-band segmentation and 'Highest Frequency Smoothing' gives good vegetation type classification results. A pine mask is deduced from the classification result and vegetation stress indices like EGFN are calculated for the pine mask. The vegetation stress index EGFN shows high stress levels (low EGFN values) in the vicinity of the former zinc-melting factory at 'Maatheide' and decreasing stress levels at more distant locations. The EGFN map was validated against Cd and Zn concentrations determined from soil and vegetable samples collected about 1000 m south of 'Maatheide'. High EGFN values for the reference track, where no heavy-metal contamination is present, indicate the absence of stress as expected. This technique to detect vegetation stress was applied successfully for pine, but can probably be used to map vegetation stress in other tree types, crops, …

ACKNOWLEDGEMENTS

This work was supported by the Flemish Waste Management Agency OVAM.

REFERENCES

1. *Peñuelas J., et al., Reflectance Indices Assocoiated with Physiological Changes in Nitrogen- and Water-limited Sunflower Leaves, Remote Sensing of Environment 48, p. 135-146 (1994)*

2. *Vangronsveld J. et al., Reclamation of a Bare Industrial Area Contaminated by Non-Ferrous Metals: In-Situ Metal Immobilization and Revegetation, Environmental Pollution Vol. 87, p. 51-59 (1995)*

3. *Zarco P.J., Optical Indices as Bioindicators of Forest Condition from Hyperspectral CASI data, Proceedings 19th Symposium of the European Association of Remote Sensing Laboratories (EARSeL), Valladolid, Spain, (1999)*